Study on the Anisotropy of Silver Nanowire-Polymer Composite Films by Optical Polarization Analysis

Takeo Tomiyama

February 2021

Study on the Anisotropy of Silver Nanowire-Polymer Composite Films by Optical Polarization Analysis

Takeo Tomiyama
Doctoral Program in Engineering Sciences
Subprogram in Materials Science and Engineering

Submitted to the
Degree Programs in Pure and Applied Sciences of the
Graduate School of Science and Technology
in Partial Fulfillment of the Requirements
for the Degree of Doctor of Philosophy in
Engineering

at the
University of Tsukuba

Abstract

Transparent conductive films (TCFs) are essential elements of many optoelectronic devices such as liquid crystal displays (LCDs), touch panels, organic light emitting diodes (OLEDs) and solar cells. Currently, indium tin oxide (ITO) films are the most widely used TCFs, but ITO film is so brittle that its applicability to next-generation flexible devices is limited. Among the potential substitutes, silver nanowires (AgNWs) are regarded as the most promising candidate because they can form a continuous network with high optical transparency, low electrical resistivity, and excellent mechanical flexibility. Furthermore, AgNW-based TCFs can be mass-produced by cost-effective wet coating methods, using a slot die coater.

However, such AgNW-based TCFs show undesirable dependence on the AgNW orientation, notably electrical anisotropy. The purpose of this study was to fully characterize the anisotropy of AgNW-polymer composite TCFs, as well as to evaluate and reduce issues encountered in their practical application to electronic devices.

I investigated the origin of the electrical anisotropy, by using dark-field microscopic image analysis and optical polarization spectroscopy to quantify the orientation distribution of the AgNWs. The results indicated that the distribution of AgNWs is not fully isotropic: their long axis is preferentially oriented along the lengthwise direction of the coated films. I also established the relationship between structural, electrical, and optical anisotropy. This allowed me to infer quantitative estimates of the structural and electrical anisotropy from by optical analysis.

I then focused on practical applications of AgNW-based TCFs, such as touch screen devices, for which three-dimensional anisotropy is also an important parameter. I characterized the three-dimensional structure of AgNWs networks by determining the orthogonal optical constants of the composite films with Mueller matrix spectroscopic ellipsometry.

Finally, I quantified and reduced adverse effects phenomena appearing when AgNW-polymer TCFs are used for touch screens: the “LCD light leakage” and the “electrode pattern visibility”. I also proposed methods to reduce such effects.

Contents

1. Introduction 1

1.1 Alternative materials 2

1.2 Silver nanowires 4

1.3 Motivation of the study 5

1.4 Outline of this thesis 6

1.5 References for Chapter 1 7

2. Materials and methods 11

2.1 Introduction 11

2.2 AgNW-polymer composite films 12

2.2.1 TCTF fabrication 12

2.2.2 Fabrication of transparent conductive electrodes using TCTF 13

2.3 Specifications of AgNW samples 16

2.4 Optical characterization 21

2.4.1 Polarized optical spectroscopy 21

2.4.2 Ellipsometry measurements 21

2.4.3 Mueller matrix measurements for diattenuation and retardation 22

2.4.4 Photometric measurements for depolarization 22

2.4.5 Absorption and scattering measurements 24

2.5 Electrical characterization 26

2.6 References for Chapter 2 26

3. Relationship between structural, electrical, and optical anisotropy 30

3.1 Introduction 30

3.2 Structural anisotropy of AgNWs 31

3.3 Optical anisotropy of AgNWs 36

3.4 Electrical anisotropy of AgNWs 41

3.5 Influence of the AgNW loading amount 44

3.6 Relationship between polarized transmittance and sheet resistance 46

3.7 Conclusion for this chapter 48

3.8 References for Chapter 3 48

4. Optical anisotropy studies with Mueller matrix ellipsometry 51

4.1 Introduction 51

4.2 Fundamentals of ellipsometry 52

4.2.1 Standard ellipsometry 52

4.2.2 Generalized ellipsometry 53

4.2.3 Mueller matrix ellipsometry 54

4.3 Optical model description 56

4.3.1 Quartz substrate 57

4.3.2 Polymer layer 57

4.3.3 Conductive layer 57

4.4 Determination of the optical constants 58

4.5 Conclusion for this chapter 68

4.6 References for Chapter 4 69

5. Polarization properties of AgNWs 71

5.1 Introduction 71

5.2 Diattenuation, retardation and depolarization 72

5.3 Polarization properties 75

5.3.1 Mueller matrix measurements 75

5.3.2 Diattenuation 76

5.3.3 Retardation 77

5.3.4 Depolarization 79

5.4 Light leakage of LCDs 83

5.5 Conclusion for this chapter 84

5.6 References for Chapter 5 85

6. Absorption and scattering by AgNWs 87

6.1 Introduction 87

6.2 Optical measurements 88

6.2.1 Absorption and scattering measurements 88

6.2.2 Color difference calculations 88

6.3 Transmission and reflection spectra 89

6.4 Absorption and scattering spectra 91

6.4.1 TCTF samples 91

6.4.2 Mie simulations – singular infinite AgNW 94

6.5 Color difference 95

6.6 Conclusion for this chapter 99

6.7 References for Chapter 6 99

7. Conclusion 101

7.1 Summary of the thesis 101

7.2 Future work 102

List of publications 104

Appendix 1 105

Orientation of AgNWs in the composite films 105

Appendix 2 107

CIEDE2000 color difference formula 107

Acknowledgements 110

Chapter 1

Introduction

In many optoelectronic devices such as liquid crystal displays (LCDs), touch screens, organic light emitting-diodes (OLEDs) and solar cells, transparent conductive materials (TCMs) are used as electrodes. The TCM market is likely to continue growing, because of the high industrial demand for personal devices. Screen flexibility will also allow for increased diversity of new products in many sectors, from consumer electronics and sensors to biomedical devices [1].

Currently, indium tin oxide (ITO) is the most widely used TCM, because of its transparency in the visible spectral region and its relatively low resistivity [2]. However, ITO film fabrication requires a high deposition vacuum and high annealing temperature, which is expensive and time-consuming. Furthermore, indium is a rare material, and its varying availability can cause fluctuations in ITO prices. More importantly, ITO film is so brittle that its application to the next generation of devices, which will be mainly flexible, is problematic [3]. For those reasons, there has been a strong push to investigate, materials that could constitute a suitable alternative to ITO, with better mechanical and optoelectronic performance [4, 5]. Finally, next-generation TCMs need to be inexpensive, therefore their fabrication should be possible with large-scale manufacturing methods.

1.1 Alternative materials

Various TCMs have been proposed as potential replacements for ITO, for example carbon nanotubes (CNTs) [6], graphene [7], conducting polymers [8], metal mesh [9] and metal nanowires [10]. Table 1.1 compares their main properties with those of ITO. Typical requirements for industrial production of optoelectronic devices are a transmittance of 90% or more, with a sheet resistance of less than 100 Ω/sq. However, depending on the intended application, the sheet resistance requirement varies. For example, touch screens require a sheet resistance of 50-100 Ω /sq. [11], while OLEDs require a sheet resistance of 20 Ω /sq. or less [12].

Table 1.1 Comparative properties of ITO and several alternative TCMs

	ITO	CNTs	Graphene	Conducting polymer	Metal mesh	Metal NWs
Sheet resistance (Ω/sq.)	5-100	25-300	30-5000	125-1500	0.8	30-100
Transmittance (%)	80-97	80-91	80-96	90	90	80-96
Stability	○	○	○	×	○	○
Flexibility	×	○	○	○	○	○
Cost	Medium	High	High	High	High	Medium

Random meshes of CNT-based electrodes are highly flexible, but their conductivity is low because of the high junction resistance between CNTs [13]. Although graphene shows high carrier mobility, it is very sensitive to defects and large-scale production remains difficult [14]. One of the most studied conductive polymers, poly(3,4-ethylenedioxithiophene): polystyrene sulfonate known as PEDOT:PSS has excellent mechanical flexibility and solution processability. However, conductive polymers in general show poor stability in ambient air, because they absorb oxygen and moisture [15]. The sheet resistance of a metal mesh can be close to that of bulk metal, even when the line width is close to a few microns [16]. Thus, the metal mesh TCMs have already been

used for high-grade devices. However, their manufacturing process, which includes high-resolution photolithography, is complicated and expensive.

Metal nanowires are one-dimensional nanomaterials with diameters of 10-200 nm and lengths of 5-100 um. So far, nanowires using copper [17] and silver [18-23] have been produced and characterized. Among the potential alternatives to ITO, metal nanowires are now regarded as the most promising candidate, because they can form a continuous two-dimensional (2D) network characterized by high transparency, low resistivity, and excellent mechanical flexibility. Furthermore, transparent conductive films (TCFs) based on such networks can be fabricated by cost-effective wet coating methods such as dip coating [24], spray coating [25], Meyer rod coating [26], and scalable, roll-to-roll compatible slot die coating [27-30].

Figure 1.1 shows the relationship between the transmittance and sheet resistance for some ITO alternatives [31]. Because silver is the most conductive metal, AgNW electrodes show superior electrical and optical performance compared with other materials. AgNWs are already commercialized by multiple companies, and AgNW-based transparent conductive electrodes are increasingly used for touch screen manufacturing.

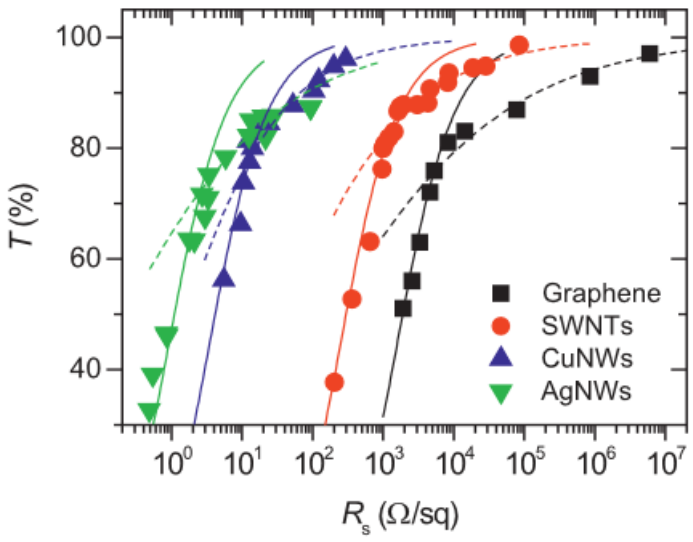

Figure 1.1 Typical transmittance (generally measured at ~ 550 nm) as a function of sheet resistance for thin films of nanostructured materials [31].

1.2 Silver nanowires

The optical and electrical properties of AgNW networks have been extensively investigated in the past decade, both theoretically and experimentally. Network transmittance and sheet resistance depend on various parameters, including the diameter (D), length (L), aspect ratio (L/D) of the AgNWs, as well as their loading amount and junction resistance between the wires.

Loading amount is an important parameter that plays the primary role in defining both the sheet resistance and transparency of AgNW network [32]. Sparse networks are very transparent but have high sheet resistance, whereas dense networks are highly conductive but appear opaque. The length of the nanowires is also important in determining the network properties: longer nanowires require fewer wire junctions, resulting in a lower sheet resistance [33]. X. Xu *et al*. reported that longer nanowires induced not only low sheet resistance – by forming more conductive routes through the network – but also better transparency [34]. M. Marus *et al*. showed that, theoretically, 200-µm-long nanowires induce a 13.5 times lower sheet resistance than 10-µm-long nanowires with similar transmittance [35]. The diameter of the nanowire influences mainly network conductivity. S. M. Bergin *et al*. reported that, for a given transmittance, using nanowires with a smaller diameter led to an increase in nanowire density, which improved network conductivity [33]. G.Khanarian *et al*. presented an analysis of the optical and electrical properties of AgNW based on Mie light scattering and electrical percolation theory [36]. They showed that transmission depends only on the AgNW diameter, whereas the network electrical properties depend on both the diameter and, very sensitively, on the critical percolation concentration. They concluded that it is possible to make transparent conductors with high transmission (T > 90%) and sheet resistance Rs of about 100 Ω/sq, as long as the nanowire diameter is 50 nm or less and their aspect ratio 250 or more. The sheet resistance of the network is also determined by the junction resistance between the nanowires. In fact, R. M. Mutiso *et al*. showed that the main parameters that determine the relationship between the transmittance and the sheet resistance are the length, diameter, loading amount, and average effective junction

resistance between the nanowires [37]. Furthermore, computational methods have recently been developed to predict the sheet resistance and transparency of isotropic nanowire networks [38, 39]. In summary, the impact of nanowire parameters on the macroscopic properties of isotropic nanowire networks has been extensively investigated and is now well-characterized.

1.3 Motivation of the study

Various methods can be used to synthesize AgNWs. Among these, the polyol method presents several advantages in terms of cost and mass-production capabilities. It is currently the most common preparation method for AgNWs [40]. However, AgNW-based TCFs can also be mass-manufactured by a slot die-coating method that can help to further reduce fabrication costs. Unfortunately, composite films fabricated by slot die-coating exhibit electrical anisotropy, characterized by a lower sheet resistance value in the lengthwise direction of the film and a higher value in the crosswise direction. This undesirable effect must be minimized in practical applications, such as designing an electric circuit. For example, a typical requirement for TCF electrodes is that the electrical anisotropy should not exceed 1.2. This problem motivated me to study the relationship between electrical anisotropy and AgNW orientation in the polymer matrix.

Additionally, AgNWs are not uniformly oriented in the TCF. This causes angular variations of the sheet resistance, as well as optical anisotropy. An important implication of this effect is that it is easier to analyze the AgNW orientation distribution using optical, rather than electrical, measurements. Indeed, measuring sheet resistance is time-consuming because the patterned electrodes must be photolithographically manufactured. On the contrary, optical measurements are contactless, non-destructive, and do not require any processing of the film sample. Furthermore, spectral characterization of AgNW-based TCFs over a wide wavelength range shows the transverse and longitudinal modes of AgNW localized surface plasmon resonance (LSPR), which constitute valuable information to estimate the AgNW orientation.

Lastly, it was necessary to evaluate the practical aspects of implementing AgNW-

based TCFs into touch screens for electronic devices. For this purpose, I quantified adverse effects such as “LCD light leakage [41]” and “electrode pattern visibility [42]” and investigated how they could be reduced.

1.4 Outline of this thesis

In the following chapter, the AgNW-polymer composite films are described in detail and their properties, especially the different aspects of network anisotropy, are thoroughly investigated. Undesirable resulting effects are quantified and mitigating solutions are proposed.

Chapter 2 describes the fabrication methods and specifications of AgNW-polymer composite films used throughout this thesis. In Chapter 3, the AgNW orientation distribution is quantified using dark field microscopy and optical polarization spectroscopy. A relationship between structural, electrical, and optical anisotropy is established and used to quantify the structural and electrical anisotropy by optical analysis. In Chapter 4, I investigate the three-dimensional (3D) structure of the AgNW network and develop a model for spectroscopic ellipsometry analysis of biaxial AgNW networks, notably using Mueller matrix ellipsometry to determine the orthogonal optical constants of the composite films. Chapter 5 discusses the “LCD light leakage” phenomenon. Retardation and depolarization within the composite films, which depend on the AgNW characteristics, are quantified using, respectively, polarimetry measurements and a newly developed photometric method. In Chapter 6, “pattern visibility” is described and evaluated quantitatively, by applying the color difference (ΔE_{00}) formalism to diffuse reflection spectra of the composite films.

Finally, Chapter 7 contains the summary of my findings and achievements, as well as the potential future steps of my research and the implication of my work for the next generation of flexible electronic devices.

1.5 References for Chapter 1

[1] Lili Wang, Zheng Lou, Kai Jiang, Guozhen Shen, "Bio-Multifunctional Smart Wearable Sensors for Medical Devices," Adv. Intell. Syst. 1(5), 1900040 (2019).

[2] Akshay Kumar, Chongwu Zhou, "The Race to Replace Tin-Doped Indium Oxide: Which Material Will Win," ACS Nano 4(1), 11-14 (2010).

[3] Thomas Sannicolo, Mélanie Lagrange, Anthony Cabos, Caroline Celle, Jean-Pierre Simonato, Daniel Bellet, "Metallic Nanowire-Based Transparent Electrodes for Next Generation Flexible Devices: A Review," Small 12(44), 6052-6075 (2016).

[4] Liangbing Hu, Hui Wu, Yi Cui, "Metal Nanogrids, Nanowires, and Nanofibers for Transparent Electrodes," MRS Bull. 36(10), 760-765 (2011).

[5] Martin Weis, "Transparent Electrodes for Flexible Organic Light-Emitting Diodes and Displays," Display and Imaging 2, 49-68 (2015).

[6] J. Chen, A. I. Minett, Y. Liu, C. Lynam, P. Sherrell, C. Wang, G. G. Wallace, "Direct Growth of Flexible Carbon Nanotube Electrodes," Adv. Mater. 20(3), 566-570 (2008).

[7] Gunho Jo, Minhyeok Choe, Sangchul Lee, Woojin Park, Yung Ho Kahng, Takhee Lee, "The Application of Graphene as Electrodes in Electrical and Optical Devices," Nanotechnology 23(11), 112001(2912).

[8] Hui Shi, Congcong Liu, Qinglin Jiang, Jingkun Xu, "Effective Approaches to Improve the Electrical Conductivity of PEDOT:PSS: A Review," Adv. Electron. Mater. 1(4), 1500017 (2015).

[9] Hock Beng Lee, Won-Yong Jin, Manoj Mayaji Ovhal, Neetesh Kumar; Jae-Wook Kang, "Flexible Transparent Conducting Electrodes Based on Metal Meshes for Organic Optoelectronic Device Applications: A Review," J. Mater. Chem. C 7(5), 1087-1110 (2019).

[10] Shengrong Ye, Aaron R. Rathmell, Zuofeng Chen, Ian E. Stewart, Benjamin J. Wiley, "Metal Nanowire Networks: The Next Generation of Transparent Conductors," Adv. Mater. 26(39), 6670-6687 (2014).

[11] Chang Seok Oh, Sang Mun Lee, Eun Hye Kim, Eun-Woo Lee, Lee Soon Park, "Electro-Optical Properties of Index Matched ITO-PET Film for Touch Panel Application," Mol. Cryst. Liq. Cryst. 568, 32-37 (2012).

[12] Dongxiang Luo, Qizan Chen, Baiquan Liu, Ying Qiu, "Emergence of Flexible White Organic Light-Emitting Diodes," Polymers 11(2), 384 (2019).

[13] M.S. Fuhrer, J. Nygård, L. Shih, M. Forero, Young-Gui Yoon, M. S. C. Mazzoni, Hyoung Joon Choi, Jisoon Ihm, Steven G Louie, A. Zettl, Paul L. McEuen, "Crossed Nanotube Junctions," Science 288 (5465), 494-497 (2000).

[14] Yuyan Shao, Jun Wang, Mark Engelhard, Chongmin Wanga, Yuehe Lin, "Facile and Controllable Electrochemical Reduction of Graphene Oxide and its Applications," J.

Mater. Chem. 20, 743-748 (2010).

[15] A. M. Nardes, M. Kemerink, M. M. de Kok, E. Vinken, K. Maturova, R.A.J. Janssen, “Conductivity, Work Function, and Environmental Stability of PEDOT:PSS Thin Films Treated with Sorbitol,” Org. Electron. 9(5), 727-734 (2008).

[16] Peter B. Catrysse, Shanhui Fan, “Nanopatterned Metallic Films for Use as Transparent Conductive Electrodes in Optoelectronic Devices,” Nano Lett. 10(8), 2944-2949 (2010).

[17] Vu Binh Nam, Daeho Lee, “Copper Nanowires and Their Applications for Flexible, Transparent Conducting Films: A Review,” Nanomaterials 6(3), 47 (2016).

[18] Daniel Langley, Gaël Giusti, Céline Mayousse, Caroline Celle, Daniel Bellet, Jean-Pierre Simonato, “Flexible Transparent Conductive Materials Based on Silver Nanowire Networks: A Review,” Nanotechnology 24(45), 452001 (2013).

[19] Duc Anh Dinh, Kwun Nam Hui, Kwan San Hui, Pushpendra Kumar, Jai Singh, “Silver Nanowires: A Promising Transparent Conducting Electrode Material for Optoelectronic and Electronic Applications,” Rev. Adv. Eng. 2(4), 324-345 (2013).

[20] Weiwei He, Changhui Ye, “Flexible Transparent Conductive Films on the Basis of Ag Nanowires: Design and Applications: A Review,” J Mater Sci Technol. 31(6), 581-588 (2015).

[21] Daniel Bellet, Mélanie Lagrange, Thomas Sannicolo, Sara Aghazadehchors, Viet Huong Nguyen, Daniel P. Langley, David Muñoz-Rojas, Carmen Jiménez, Yves Bréchet, Ngoc Duy Nguyen, “Transparent Electrodes Based on Silver Nanowire Networks: From Physical Considerations towards Device Integration,” Materials 10(6), 570 (2017).

[22] Renyun Zhang, Magnus Engholm, “Recent Progress on the Fabrication and Properties of Silver Nanowire-Based Transparent Electrodes,” Nanomaterials 8(8), 628 (2018).

[23] Jinhyeong Kwon, Young D. Suh, Jinhwan Lee, Phillip Lee, Seungyong Han, Sukjoon Hong, Junyeob Yeo, Habeom Lee, Seung Hwan Ko, “Recent Progress in Silver Nanowire Based Flexible/Wearable Optoelectronics,” J. Mater. Chem. C. 6(28), 7445-7461 (2018).

[24] Kwangguk Ahn, Dongjae Kim, Onyu Kim, Jaewook Nam, “Analysis of Transparent Conductive Silver Nanowire Films from Dip Coating Flow,” J. Coat. Technol. Res. 12(5), 855-862 (2015).

[25] Jin-Young Lee, Dongkyun Shin, Jongwoon Park, “Fabrication of Silver Nanowire-Based Stretchable Electrodes Using Spray Coating,” Thin Solid Films 608, 34-43 (2016).

[26] Eun Jung, Chanho Kim, Minha Kim, Heeyeop Chaea, Jeong HoCho, Sung Min Cho, “Roll-to-Roll Preparation of Silver-nanowire Transparent Electrode and its Application to Large-area Organic Light-emitting Diodes,” Organic Electronics 41, 190-197 (2017).

[27] Michael Spaid, “Wet-Processable Transparent Conductive Materials,” Information

Display 28(1), 10-15 (2012).

[28] Keehyun Shin, Janghoon Park, Changwoo Lee, "A 250-mm-Width, Flexible, and Continuous Roll-to-Roll Slot-Die Coated Carbon Nanotube/Silver Nanowire Film Fabrication and a Study on the Effect of Anti-reflective Overcoat," Thin Solid Films 598, 95-102 (2016).

[29] Dong-Ju Kim, Hae-In Shin, Eun-Hye Ko, Ki-Hyun Kim, Tae-Woong Kim, Han-Ki Kim, "Roll-to-roll Slot-die Coating of 400 mm Wide, Flexible, Transparent Ag Nanowire Films for Flexible Touch Screen Panels," Sci. Rep. 6, 34322 (2016).

[30] S. M. Raupp, L. Merklein, M. Pathak, P. Scharfer, W. Schabel, "An Experimental Study on the Reproducibility of Different Multilayer OLED Materials Processed by Slot Die Coating," Chem Eng Sci. 160, 113-120 (2017).

[31] Sukanta De, Jonathan N. Coleman, "The Effects of Percolation in Nanostructured Transparent Conductors," MRS Bull. 36(10), 774-781 (2011).

[32] Y. H. Wang, X. Yang, D. X. Du, X. F. Zhang, "A Comprehensive Study of High-performance of Flexible Transparent Conductive Silver Nanowire Films," J. Mater. Sci.: Mater. Electron. 30, 13238-13246 (2019).

[33] Stephen M. Bergin, Yu-Hui Chen, Aaron R. Rathmell, Patrick Charbonneau, Zhi-Yuan Lib, Benjamin J. Wiley, "The Effect of Nanowire Length and Diameter on the Properties of Transparent, Conducting Nanowire Films," Nanoscale 4(6), 1996 (2012).

[34] Xiaomei Xu, Song He, Conghua Zhou, Xingda Xia, Liao Xu, Hui Chen, Bingchu Yanga, Junliang Yang, "Largely-increased Length of Silver Nanowires by Controlled Oxidative Etching Processes in Solvothermal Reaction and the Application in Highly Transparent and Conductive Networks," RCS Adv. 6(107), 105895-105902 (2016).

[35] Mikita Marus, Aliaksandr Hubarevich, Reuben Jeremy Weixiong Lim, Hui Huang, Aliaksandr Smirnov, Hong Wang, Weijun Fan, Xiao Wei Sun, "Effect of Silver Nanowire Length in a Broad Range on Optical and Electrical Properties as a Transparent Conductive Film," Opt. Mater. Express 7(3), 1105-1112 (2017).

[36] Garo Khanarian, Jaebum Joo, X.-Q. Liu, Peter Eastman, Daniel Werner, Kathleen M. O'connell, Peter Trefonas, "The Optical and Electrical Properties of Silver Nanowire Mesh Films," J. Appl. Phys 114, 024302 (2013).

[37] Rose M. Mutiso, Michelle C. Sherrott, Aaron R. Rathmell, Benjamin J. Wiley, Karen I. Winey, "Integrating Simulations and Experiments to Predict Sheet Resistance and Optical Transmittance in Nanowire Films for Transparent Conductors," ACS Nano, 7(9), 7654-7663 (2013).

[38] Fei Han, Thirupathi Maloth, Gilles Lubineau, Recep Yaldiz, Amit Tevtia, "Computational Investigation of the Morphology, Efficiency, and Properties of Silver Nano Wires Networks in Transparent Conductive Film," Sci. Rep. 8, 17494 (2018).

[39] Hugh G. Manning, Claudia Gomes da Rocha, Colin O' Callaghan, Mauro S. Ferreira, John J. Boland, "The Electro-Optical Performance of Silver Nanowire Networks,"

Sci. Rep. 9, 11550 (2019).

[40] Yue Shi, Liang He, Qian Deng, Quanxiao Liu, Luhai Li, Wei Wang, Zhiqing Xin, Ruping Liu, “Synthesis and Applications of Silver Nanowires for Transparent Conductive Films,” Micromachines 10(5), 330 (2019).

[41] Takeo Tomiyama, Kensuke Yoshihara, Hiroshi Yamazaki, “Polarization Properties of Silver Nanowire/Polymer Composite Films: Diattenuation, Retardance and Depolarization,” Opt. Mater. Express 9(6), 2582-2594 (2019).

[42] Takeo Tomiyama, Ikuo Mukai, Hiroshi Yamazaki, Yoshihiko Takeda, “Optical Properties of Silver Nanowire/Polymer Composite Films: Absorption, Scattering and Color Difference,” Opt. Mater. Express 10(12), 3202-3214 (2020).

Chapter 2

Materials and methods

2.1 Introduction

Many applications require TCFs to be formed into a suitable electrical circuit on the substrate. For this purpose, conventional photolithography and laser ablation are commonly used to create the desired metal nanowire pattern. However, photolithography requires numerous chemicals−photoresists, photoresist developers, photoresist stripping solution, chemical reagents for metal etching−and complex fabrication processes [1-4]. Alternately, AgNWs can be selectively ablated by focused pulsed laser scanning [5, 6], but this method is inefficient and can cause thermal damage to the substrate [7]. Furthermore, an encapsulation layer is needed to protect AgNWs from undesirable chemical reaction, notably oxidation, and to remedy the low adhesion between AgNWs and substrate. Examples of encapsulant polymers are acrylate polymer [8-11], urethane polymer [12-14], poly(dimethylsiloxane) [15-18], colorless polyimide [19-22], epoxy polymer [23].

To avoid such problems, a silver nanowire-photosensitive polymer composite film called transparent conductive transfer film (TCTF) was developed in our laboratory at Showa Denko Materials Co. Ltd. (formerly Hitachi Chemical Co. Ltd.), together with a dedicated electrode fabrication process. This process is simpler and more cost-effective

than conventional patterning because it uses neither photoresist nor toxic etching reagents. The TCTF can then be transferred to various substrates and electrodes can be easily patterned through a simple photolithographic process.

This chapter describes fabrication methods and specifications of the TCTFs used throughout this thesis. Methods to measure optical and electrical properties in the TCTF are also described.

2.2 AgNW-polymer composite films

2.2.1 TCTF fabrication

An ultraviolet (UV)-curable acrylate-based polymer resin was chosen as the AgNW matrix polymer to achieve both electrode patterning and excellent encapsulation, thus enhancing the stability of the film under harsh environments. This matrix polymer is a negative-type photosensitive resin capable of alkali development. It contains a binder polymer, a photopolymerizable compound, a photopolymerization initiator, and additives. The photo-cured polymer is highly transparent over a wide spectral range and has good adhesion to both AgNWs and substrates such as polyethylene terephthalate (PET), cyclo olefin polymer (COP), and glass.

The TCTF fabrication steps are shown in Figure 2.1. First, an aqueous dispersion of AgNWs is coated onto a carrier film using a slot-die coater, then dried with roll-to-roll manufacturing techniques. Next, an additional coating of photosensitive resin is applied on top of the AgNWs and dried with the same procedure. TCTF thickness is about 5 μm. Among the solution-processing coating methods, slot-die coating is one of the most suitable for mass production [24-27]. Finally, the cover film is stacked on the resin layer and wound on the roll.

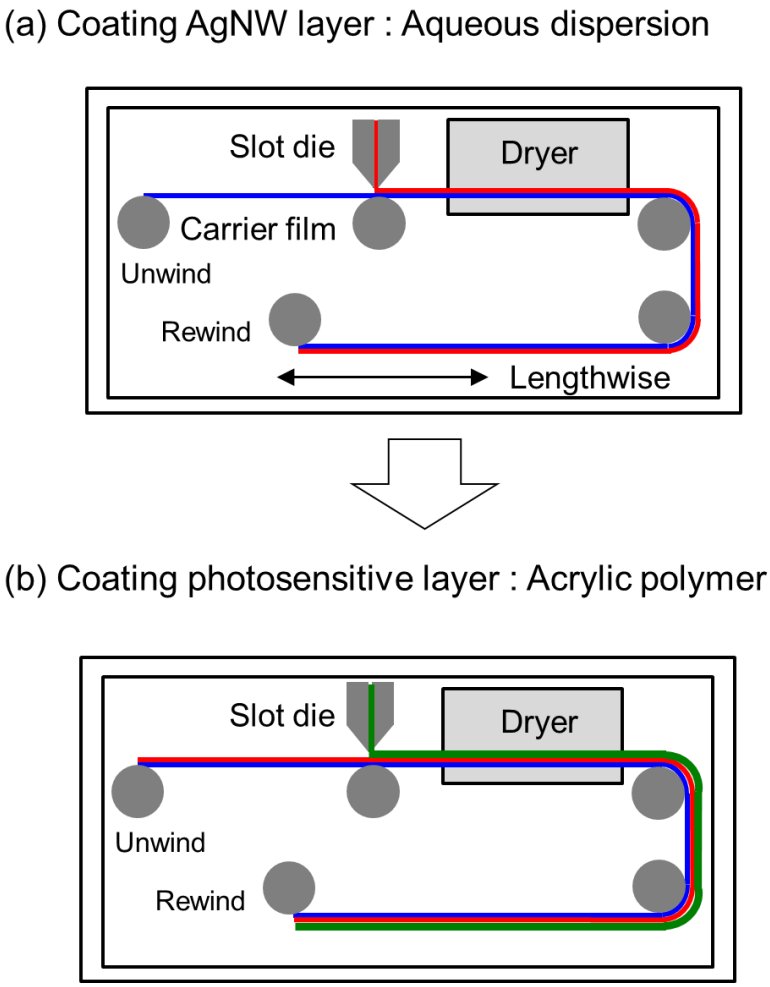

Figure 2.1 Roll-to-roll slot-die coating process for TCTF fabrication. (a) Coating and drying of the AgNW layer. (b) Coating and drying of the photosensitive resin layer.

2.2.2 Fabrication of transparent conductive electrodes using TCTF

The conventional fabrication procedure for patterned electrodes [1-4] is shown schematically in Fig. 2.2 (a). An aqueous dispersion of AgNW is first coated onto a substrate and dried to form a network. The photoresist is then coated on top of the AgNW network, covered by a photomask and exposed to UV light. Once the photoresist is developed, AgNWs are etched with an acidic etchant. Finally, the photoresist is removed with a photoresist stripping solution and a thin overcoat polymer layer is applied on the pattered AgNW electrodes.

The fabrication process for TCTF patterned electrodes is different from the standard

process (Figure 2.2 (b)). First, the TCTF is laminated upside-down at high temperature (> 100℃) onto the substrate, with AgNWs on top. A photomask is placed over the TCTF and the cover film is attached to prevent oxidation during the curing process. The electrodes, represented in dark yellow in the figure, are cured by exposure to UV light through the photomask (first exposure). The cover film is then removed, and the full surface is exposed to UV light (second exposure). At this stage, the TCTF surface is not cured (except for the first exposure) because of oxygen inhibition, and the inside of the TCTF is cured. Next, I use a water-based developing liquid, here a 1% sodium carbonate solution, to selectively dissolve the surface of the laminate to a depth of 0.8 μm, creating the land and space areas in the electrode. Finally, a high dose of UV light is used to fully cure the entire TCTF. In summary, TCTF can simplify the electrode fabrication process because photoresist or overcoat are not required for AgNWs patterning and encapsulation.

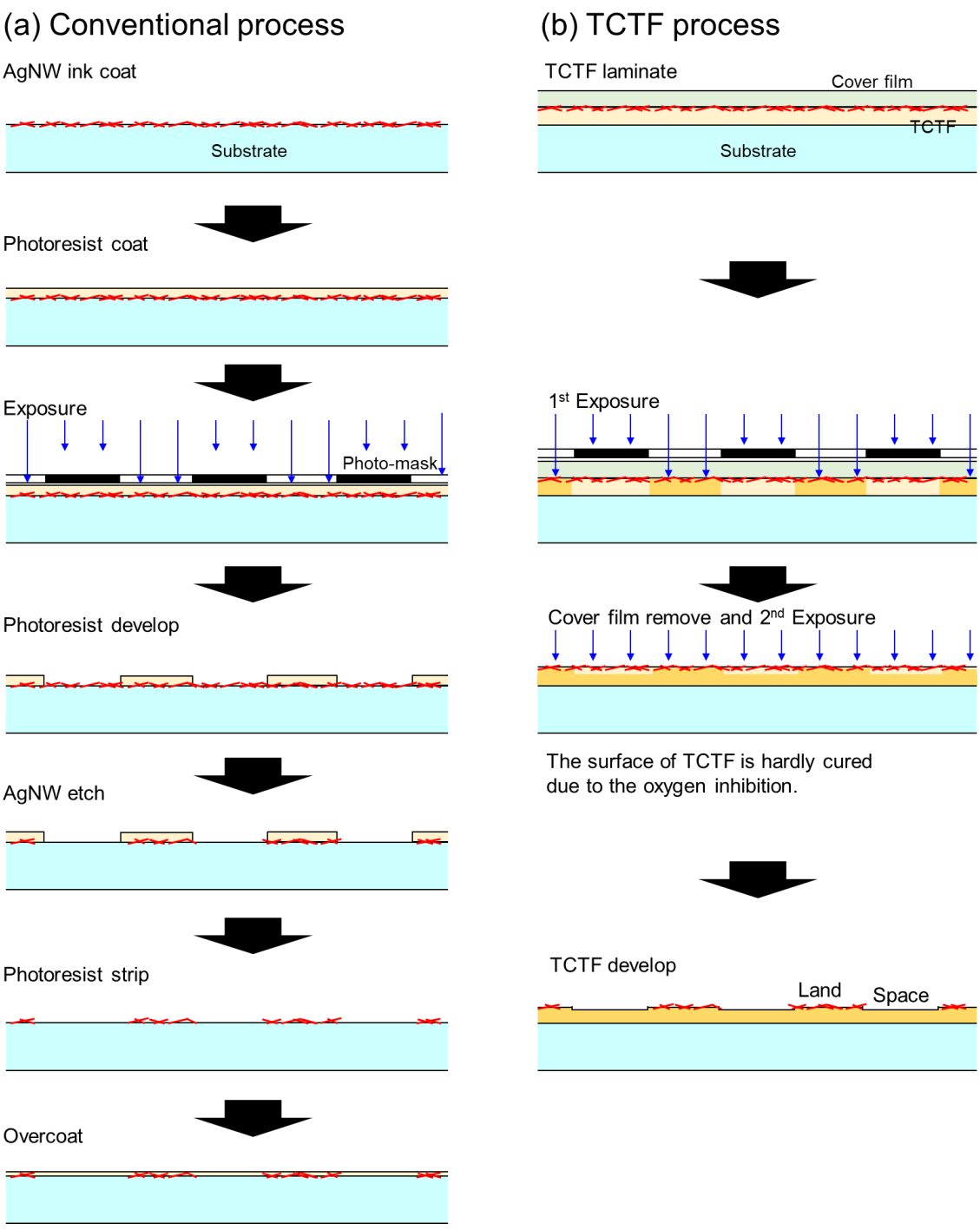

Figure 2.2 Photolithographic processes used for fabrication of AgNW-based electrodes: (a) conventional process, (b) TCTF process.

2.3 Specifications of AgNW samples

The AgNWs used for this research were obtained from Cambrios Advanced Materials Corporation [28]. Eight samples were comprehensively investigated. They can be divided into three groups according to the physical characteristics of the AgNWs. Sample properties are shown in Table 2.1.

Table 2.1 Properties of the AgNW-polymer composite film samples

Sample designation	AgNW loading (mg/m^2)	Average diameter (nm)	Average length (μm)	Transmittance[a] (%)	Sheet resistance[b] (Ω/sq.)	Electrical anisotropy[c]
A1	17	33	32.4	96.5	56.2	1.17
A2				96.2	46.8	1.47
B	18			96.7	47.6	1.36
C	22			96.3	34.1	1.30
D	37	23	27.2	95.2	25.1	1.36
E	53			92.9	19.5	1.37
F	130			84.8	9.1	1.91
G	22	19	21.0	97.0	54.5	1.51

[a] Transmittance (T) for unpolarized incident light at 550 nm. Background corrections are performed using a quartz substrate as the reference.
[b] Average sheet resistance (Rs) of the films.
[c] Crosswise-to-lengthwise sheet resistance ratio.

AgNW loading amounts in the TCTFs were measured by inductive coupled plasma mass spectrometry (ICP-MS). Before the measurements, the samples were dissolved in an acid solution and diluted with ultrapure water. AgNW diameters and lengths were estimated visually from high-magnification transmission electron microscopy (TEM) and from dark field microscopic images, respectively. Figure 2.3 shows typical TEM images for Samples A2, B and G. Typical dark field microscope images are shown in Figure 2.4 for Samples A2, B and G and Figure 2.5 for Samples B, C, D, E and F, respectively.

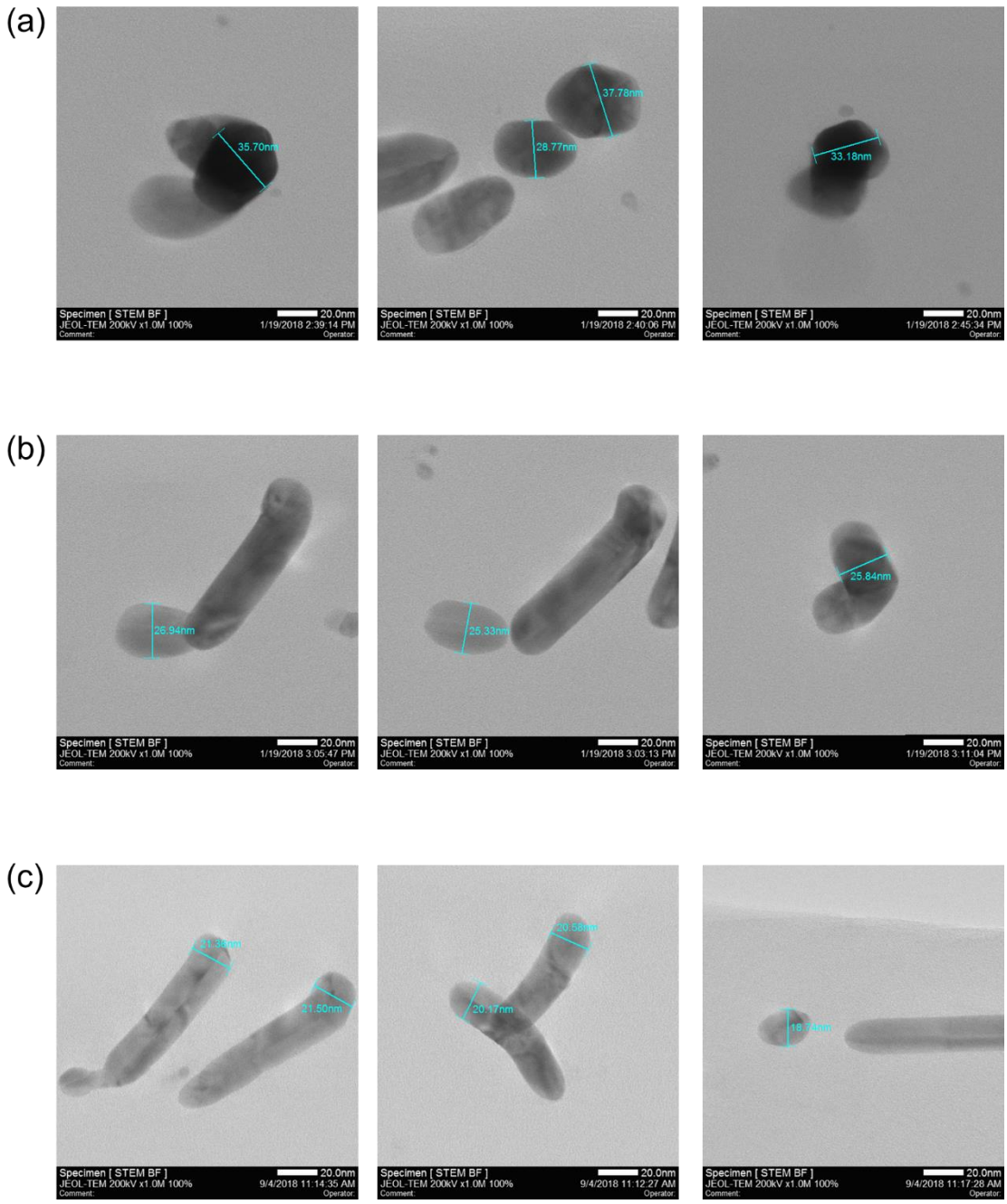

Figure 2.3 TEM images of AgNWs in Samples (a) A2, (b) B and (c) G.

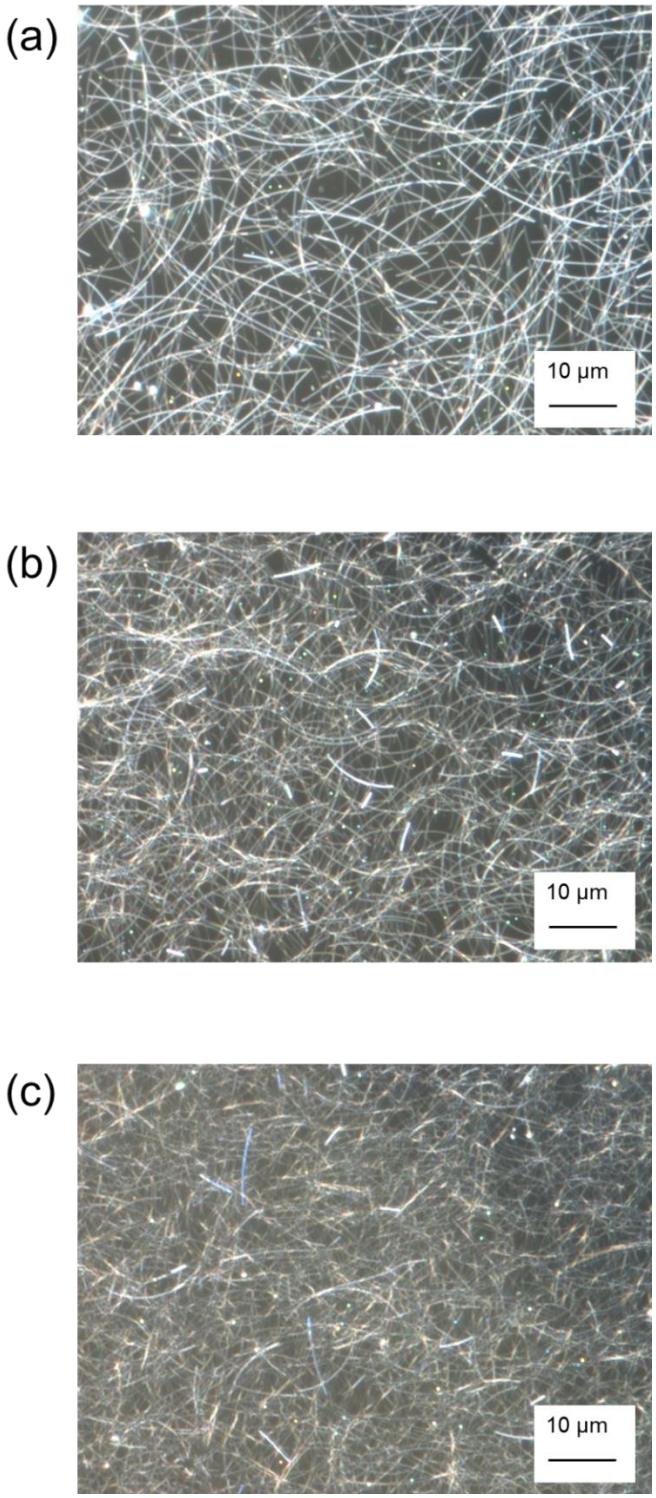

Figure 2.4 Dark field microscope images of Samples (a) A2, (b) B and (c) G.

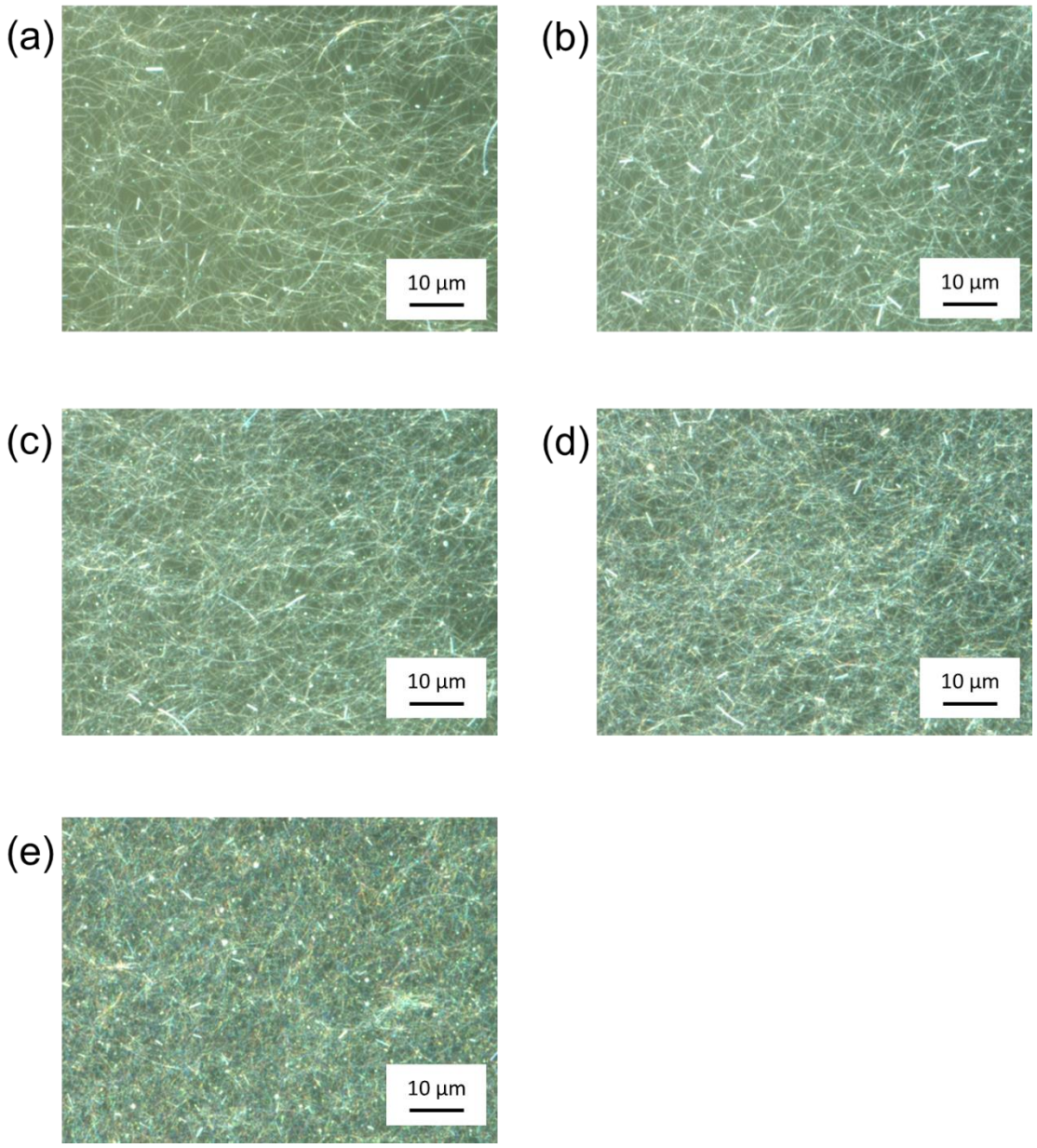

Figure 2.5 Dark field microscope images of Samples (a) B, (b) C, (c) D, (d) E and (e) F.

Samples A1 and A2 contain the same AgNWs and show similarly large average sheet resistance, but their electrical anisotropy is different. Samples A2, B and G show comparable sheet resistance for different AgNW diameters. Samples B through F contain the same AgNWs but loading amounts are different. As the loading amount increases (from Sample B to Sample F), TCTF transmittance and sheet resistance both decrease. A

sheet resistance of 50 Ω/sq. or higher is required for touch screens of 12 inches or less [29]. Therefore, even the largest sheet resistance values (56.2, 46.8, 47.6, and 54.5 Ω/sq. for Samples A1, A2, B and G, respectively) are low enough for touch screen applications. All samples show electrical anisotropy.

Samples with significantly lower sheet resistance (Samples C through F) were used to illustrate more clearly the optical (Section 2.4) and electrical (Section 2.5) properties of AgNWs. I used a 0.1 mm-thick PET film substrate for electrical measurements and a 1.0 mm-thick quartz glass substrate for optical measurements. Figure 2.6 shows a TEM image of the TCTF cross-section. Although AgNWs are embedded just below the polymer surface, embedding did not prevent electrical contact between the AgNW network and the external connection pads on the surface.

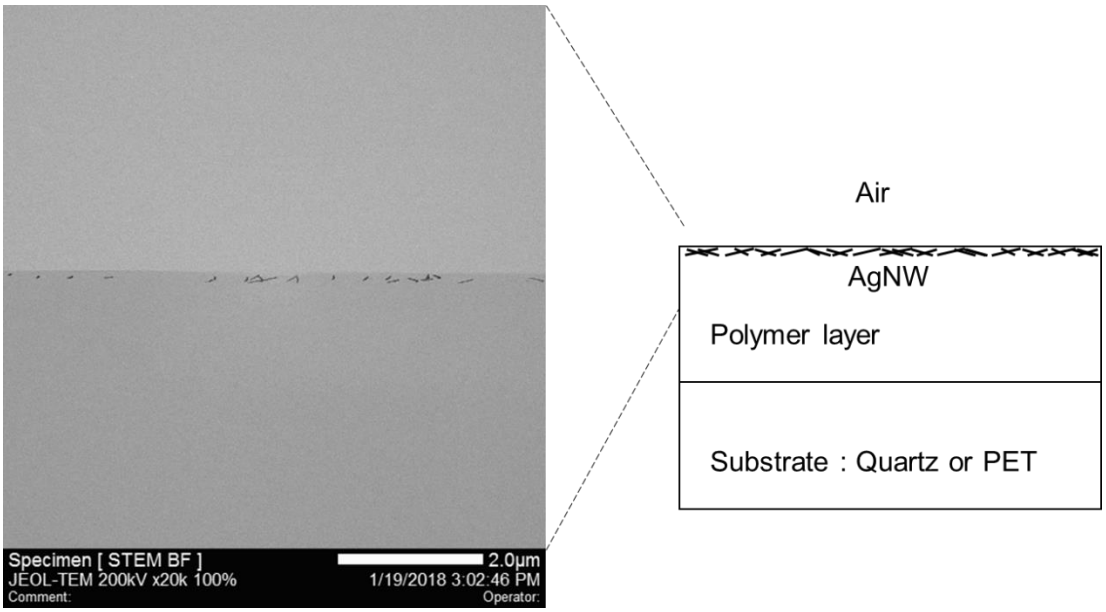

Figure 2.6 TEM cross section image of the TCTF.

2.4 Optical characterization

2.4.1 Polarized optical spectroscopy

Optical anisotropy of the TCTF was analyzed using polarized optical spectroscopy (Section 3.3). Extinction spectra, as a function of the in-plane rotation of the incoming polarized light, were measured using an Agilent Cary 7000 Universal Measurement Spectrophotometer [30] equipped with a Glan-Taylor calcite prism polarizer. In polarization-dependent measurements, the direction of polarization of the incident light is fixed, and the sample itself is rotated. The polarization angle φ is defined as the angle between the electric field vector and the lengthwise direction of the sample. Extinction was measured through a 20-mm diameter circular aperture. All samples were mounted with the coated side facing the light source. Background corrections were performed using a quartz substrate as the reference. Measurements were acquired over a spectral range of 300−2100 nm. The changeover point from the PMT detector used in the near-UV/visible region to the PbS detector used in the near-infrared (NIR) region is located at 900 nm. Data points between 900−940nm were not included in my analyses because the data in this range were too noisy to be usable.

2.4.2 Ellipsometry measurements

The TCTF thickness and optical constants were determined (Section 4.5) using a spectroscopic ellipsometer with dual rotating achromatic compensators, the “RC2” of the J. A. Woollam Co. [31]. The compensators are located before and after the sample, which allows for all 16 elements of the Mueller matrix (M_{11} to M_{44}) to be collected with high accuracy. I set up a layer stack model in the CompleteEASE analysis software [32]. Regression analysis was used to optimize the fit between calculated model parameters and experimental data.

2.4.3 Mueller matrix measurements for diattenuation and retardation

I used a spectropolarimeter (“Poxi-Spectra”, Tokyo Instruments Co., Ltd. [33]) to measure the Mueller matrix elements (defined in Section 4.2.3) of each TCTF sample (Section 5.3.1). Here, the measurement system is composed of a light source, a polarization state generator (PSG), a TCTF sample, a polarization state analyzer (PSA) and a spectrometer. The PSG is used to generate elliptical polarization states subsequently analyzed with the PSA. Diattenuation and retardation were then determined with the polar decomposition method [34] (Sections 5.3.2–5.3.3).

2.4.4 Photometric measurements for depolarization

I used a polarization measurement optical system (“RETS 100”, manufactured by Otsuka Electronics Co., Ltd. [35]) to measure depolarization of the TCTF samples (Section 5.3.4). For this analysis, each sample was placed between two high-extinction ratio Glan-Thompson linear polarizers (assumed ideal). Two measurement configurations were used: parallel, where both polarizers are oriented along the x axis of the reference frame (Figure 2.7 (a)), and crossed, where the first polarizer (on the incident side) is aligned with the x-axis and the second (transmission side) is perpendicular, along the y axis (Figure 2.7 (b)). Transmittance was measured in the parallel and crossed configurations and depolarization was derived from the results. The detailed calculation method is described in Section 5.2.

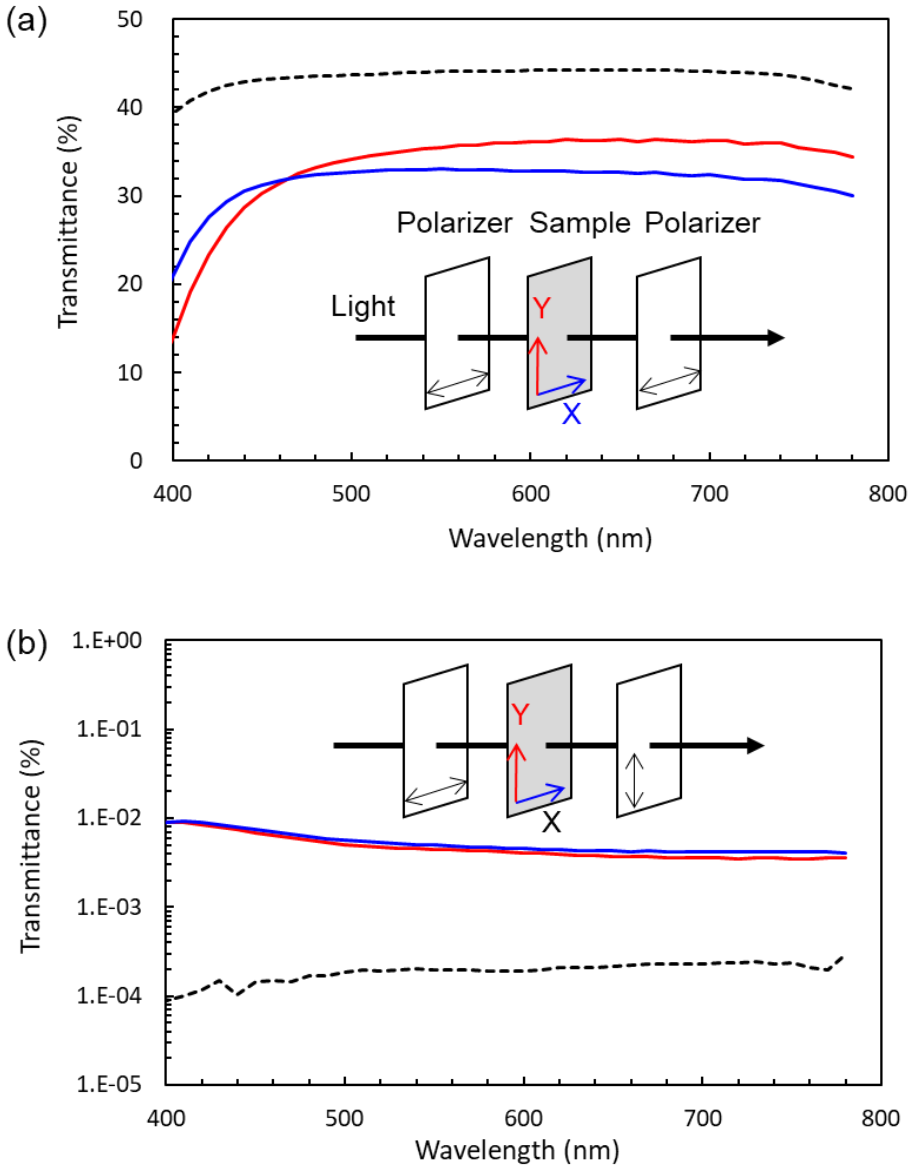

Figure 2.7 Optical transmission spectra of Sample F set between (a) parallel and (b) crossed linear polarizers. Inset diagram shows the measurement configuration, the transmission axis of each polarizer, and the principal axes (x, y) of the sample, aligned with the lengthwise (inset, x, blue arrow) and crosswise (inset, y, red arrow) TCTF directions. Blue and red transmission curves were measured along the x and y axes, respectively. The dashed black line shows the transmission spectrum of the polarizers (without sample).

2.4.5 Absorption and scattering measurements

To evaluate absorption and scattering within the TCTF samples, I measured the total and diffuse transmission and reflection spectra with a double-beam spectrophotometer (Agilent Cary 7000 Universal Measurement Spectrophotometer [30]) equipped with a 6-inch diameter integrating sphere. The integrating sphere has a 1.5-inch diameter circular port (#1), a 0.625×1.5-inch port (#2) and a 1.5×1.75-inch port (#3). SPECTRALON [36] is used for the standard reflector plates. The experimental setup is shown in Figure 2.8.

For transmittance measurements (Fig. 2.8 (a)–(d)), port #1 acts as a specular exclusion port and port #2 as a transmittance port, while port #3 is unused. Samples are placed at the transmittance port (#2), so that the integrating sphere collects all light transmitted through the samples. The specular component can be excluded or included in the measurements by opening or closing the specular exclusion port (#1). Total (T_t), diffuse (T_d) and specular (T_{sp}) transmittance can be expressed as:

$$T_t = T_2 / T_1, \tag{2.1}$$

$$T_d = (T_4 - T_3 \times (T_2 / T_1)) / T_1, \tag{2.2}$$

$$T_{sp} = T_t - T_d, \tag{2.3}$$

where T_1 and T_2 represent the total transmitted light intensity in the absence or presence of a sample, respectively, and T_3 and T_4 the light intensity scattered within the integrating sphere with and without sample, respectively.

For reflectance measurements (Fig. 2.8 (e)–(h)), the three ports act as a reflectance port (#1), an entrance port (#2) and a specular exclusion port (#3), respectively. In this configuration, samples are mounted at the reflectance port (#1). The incidence angle is set to 8°. Like for transmittance measurements, the specular component can be excluded or included. Total (R_t), diffuse (R_d) and specular (R_{sp}) reflectance can be expressed as:

$$R_t = R_2 / R_1, \tag{2.4}$$

$$R_d = (R_4 - R_3 \times (R_2 / R_1)) / R_1, \tag{2.5}$$

$$R_{sp} = R_t - R_d, \tag{2.6}$$

where R_1 and R_2 represent the total reflected light intensity in the absence or presence of a sample, respectively, and R_3 and R_4 the light intensity scattered within the integrating

sphere with and without sample, respectively.

Finally, absorption, scattering and extinction were derived from the transmission and reflection measurements as expressed in Equations (2.7–2.9):

$$\text{Absorption} = 1 - (T_t + R_t), \tag{2.7}$$

$$\text{Scattering} = T_d + R_d, \tag{2.8}$$

$$\text{Extinction} = \text{absorption} + \text{scattering}. \tag{2.9}$$

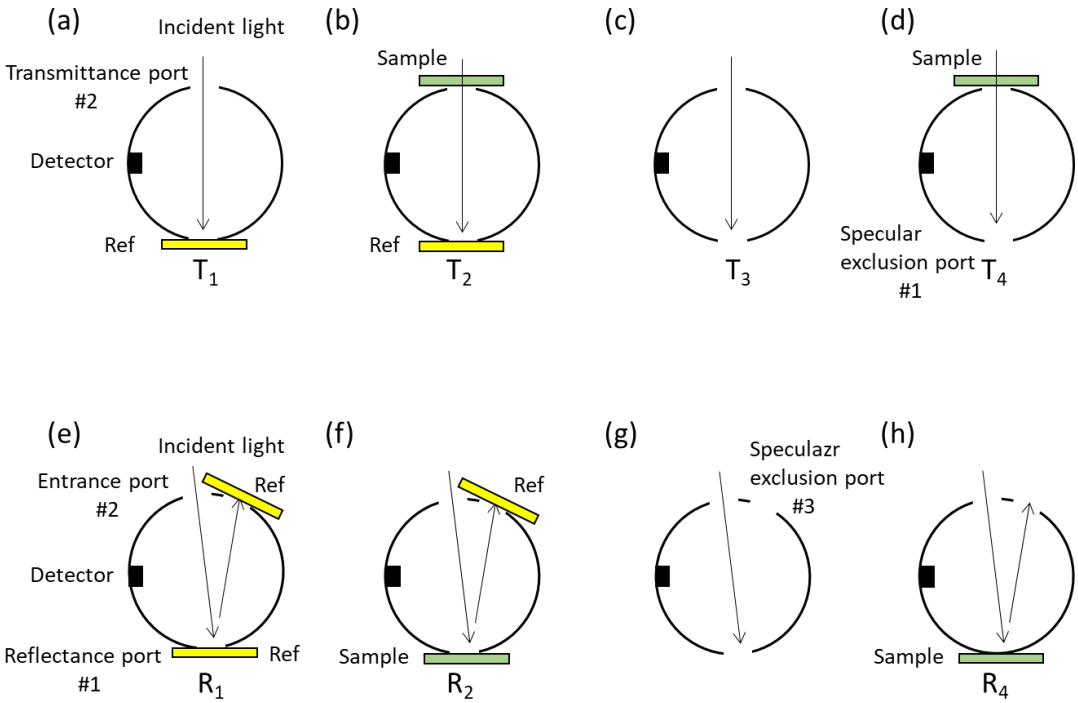

Figure 2.8 Integrating sphere configuration for transmittance (a–d) and reflectance (e–h) measurements. Transmission configurations: (a) total transmitted light, (b) total light transmitted through the sample, (c) light scattered by the sphere, (d) light scattered by the sample into the sphere. Reflection configurations: (e) total light reflected by the sphere, (f) total light reflected by the sample into the sphere, (g) light scattered by the sphere, h) light scattered by the sample and the sphere. “Ref” represents the standard reflector plate.

2.5 Electrical characterization

For electrical measurements, patterned circuit channels were fabricated by photolithography (Figure 2.9). Channel ends were marked with silver paste to improve the connection resistivity to the AgNW network. TCTF sheet resistance values depending on the measurement angle ($R_s(\theta)$, where θ is the measurement angle) were derived from the resistances of narrow channels ($R_{measured}(\theta)$) measured using 4-point probes. For each sample, resistances were measured at 12 different angles (azimuth 0 to 180° in 15° steps). For a circuit channel oriented at angle θ, the sheet resistance $R_s(\theta)$ is given by $R_s(\theta) = R_{measured}(\theta) \times W / L$, where W and L are the width (1.0 mm) and length (30 mm) of the sample, respectively. The radial angle reference, $\theta = 0°$, is set in the lengthwise direction of the TCTF. Each reported value was an average of six measurements.

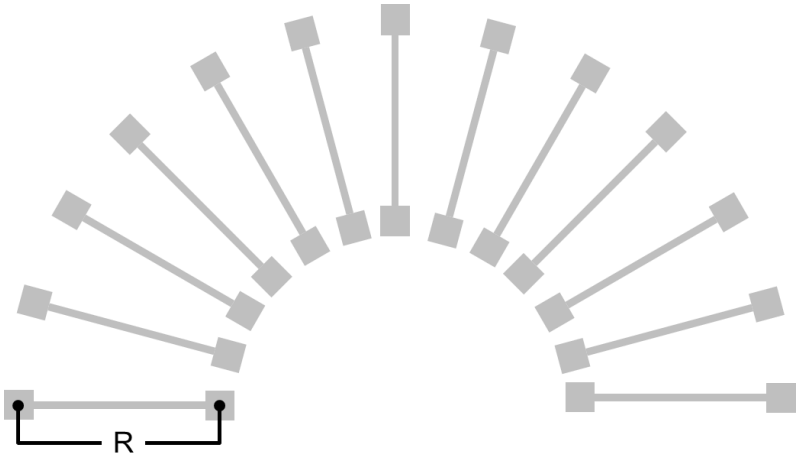

Figure 2.9 Patterned circuit lines for resistance measurements.

2.6 References for Chapter 2

[1] Yumi Ahn, Hyungjin Lee, Donghwa Lee, Youngu Lee, "Highly Conductive and Flexible Silver Nanowire-Based Microelectrodes on Biocompatible Hydrogel," ACS Appl. Mater. Interfaces 6(21), 18401-18407 (2014).

[2] Seyul Kim, So Yeon Kim, Jeonghun Kim, Jung Hyun Kim, "Highly Reliable

AgNW/PEDOT: PSS Hybrid Films: Efficient Methods for Enhancing Transparency and Lowering Resistance and Haziness," J. Mater. Chem. C. 2(28), 5636-5643 (2014).

[3] Vincent Martinez, Flurin Stauffer, Mohammed O. Adagunodo, Csaba Forro, Janos Vörös, Alexandre Larmagnac, "Stretchable Silver Nanowire-Elastomer Composite Microelectrodes with Tailored Electrical Properties," ACS Appl. Mater. Interfaces 7(24), 13467-13475 (2015).

[4] Kwonwoo Shin, Ji Sun Park, Jong Hun Han, Yunsu Choi, Dae Sung Chung, Se Hyun Kim, "Patterned Transparent Electrode with a Continuous Distribution of Silver Nanowires Produced by an Etching-free Patterning Method," Sci. Rep. 7, 40087 (2017).

[5] Harim Oh, Jeeyoung Lee, Jin-Hoon Kim, Jin-Woo Park, Myeongkyu Lee, "Fabrication of Invisible Ag Nanowire Electrode Patterns Based on Laser-Induced Rayleigh Instability," J. Phys. Chem. C 120(36), 20471-20477 (2016).

[6] Harim Oh, Myeongkyu Lee, "Laser-Direct Fabrication of Invisible Ag Nanowire Electrode Pattern on Flexible Plastic Substrate," Thin Solid Films 636, 375-383 (2017).

[7] Chang-Hyun Song, Chul Jong Han, Byeong-Kwon Ju, Jong-Woong Kim, "Photoenhanced Patterning of Metal Nanowire Networks for Fabrication of Ultraflexible Transparent Devices," ACS Appl. Mater. Interfaces 8(1), 480-489 (2016).

[8] Pengfei Kou, Liu Yang, Kequn Chi, Sailing He, "Large-area and Uniform Transparent Electrodes Fabricated by Polymethylmethacrylate-assisted Spin-Coating of Silver Nanowires on Rigid and Flexible Substrates," Opt. Mater. Express 5(10), 2347-2358 (2015).

[9] Youngmin Kim, Jong-Woong Kim, "Silver Nanowire Networks Embedded in Urethane Acrylate for Flexible Capacitive Touch Sensor," Appl. Surf. Sci. 363, 1-6 (2016).

[10] Tomke E. Glier, Lewis Akinsinde, Malwin Paufler, Ferdinand Otto, Maryam Hashemi, Lukas Grote, Lukas Daams, Gerd Neuber, Benjamin Grimm-Lebsanft, Florian Biebl, Dieter Rukser, Milena Lippmann, Wiebke Ohm, Matthias Schwartzkopf, Calvin J. Brett, Toru Matsuyama, Stephan V. Roth, Michael Rübhausen, "Functional Printing of Conductive Silver-Nanowire Photopolymer Composites," Sci. Rep. 9, 6465 (2019).

[11] Byungil Hwanga, Tae Gwang Yunb, "Stretchable and Patchable Composite Electrode with Trimethylolpropane Formal Acrylate-Based Polymer," Compos. B. Eng. 163, 185-192 (2019).

[12] Weili Hu, Xiaofan Niu, Ran Zhao, Qibing Pei, "Elastomeric Transparent Capacitive Sensors Based on an Interpenetrating Composite of Silver Nanowires and Polyurethane," Appl. Phys. Lett. 102, 083303 (2013).

[13] Yang Yang, Su Ding, Teppei Araki, Jinting Jiu, Tohru Sugahara, Jun Wang, Jan Vanfleteren, Tsuyoshi Sekitani, Katsuaki Suganuma, "Facile Fabrication of

Stretchable Ag Nanowire/Polyurethane Electrodes Using High Intensity Pulsed Light," Nano Res. 9(2), 401–414 (2016).

[14] Byungil Hwang, Chee-Hong An, Stefan Becker, "Highly Robust Ag Nanowire Flexible Transparent Electrode with UV-Curable Polyurethane-based Overcoating Layer," Mater. Des.129(5), 180-185 (2017).

[15] Feng Xu, Yong Zhu, "Highly Conductive and Stretchable Silver Nanowire Conductors," Adv. Mater. 24(37), 5117-5122 (2012).

[16] Gaeun Heo, Kyoung-hee Pyo, Da Hee Lee, Youngmin Kim, Jong-Woong Kim, "Critical Role of Diels–Adler Adducts to Realise Stretchable Transparent Electrodes Based on Silver Nanowires and Silicone Elastomer," Sci. Rep. 6, 25358 (2016).

[17] Lihua Liu, Qiang Zhang, Dong Zhao, Aoqun Jian, Jianlong Ji, Qianqian Duan, Wendong Zhang, Shengbo Sang, "Preparation and Property Research of Strain Sensor Based on PDMS and Silver Nanomaterials," J. Sens. 1-8 (2017).

[18] Yiting Chen, R. Stephen Carmichael, Tricia Breen Carmichael, "Patterned, Flexible, and Stretchable Silver Nanowire/Polymer Composite Films as Transparent Conductive Electrodes," ACS Appl. Mater. Interfaces 11(34), 31210-31219 (2019).

[19] Joshua A. Spechler, Tae-Wook Koh, Jake T. Herb, Barry P. Rand, Craig B. Arnold, "A Transparent, Smooth, Thermally Robust, Conductive Polyimide for Flexible Electronics," Adv. Funct. Mater. 25(48), 7547 (2015).

[20] Dasom Lee, Doo-Young Youn, Zhenhao Luoa, Il-Doo Kim, "Highly Flexible Transparent Electrodes Using a Silver Nanowires-Embedded Colorless Polyimide Film via Chemical Modification," RSC Adv. 6(36), 30331-30336 (2016).

[21] Dae-Gon Kim, Jiwan Kim, Seung-Boo Jung, Young-Sung Kim, Jong-Woong Kim, "Electrically and Mechanically Enhanced Ag Nanowires-Colorless Polyimide Composite Electrode for Flexible Capacitive Sensor," Appl. Surf. Sci. 380, 223-228 (2016).

[22] Chan-Jae Lee, Sungwoo Jun, Byeong-Kwon Ju, Jong-Woong Kim, "Pressure-Sensitive Strain Sensor Based on a Single Percolated Ag Nanowire Layer Embedded in Colorless Polyimide," Physica B Condens. Matter. 514, 8-12 (2017).

[23] Lei Miao, Guojun Liu, Kevin McEleney, Jiandong Wang, "Epoxy-Embedded Silver Nanowire Meshes for Transparent Flexible Electrodes," J. Mater. Sci. 54, 10355-10370 (2019).

[24] Michael Spaid, "Wet-Processable Transparent Conductive Materials," Information Display 28(1), 10-15 (2012).

[25] Keehyun Shin, Janghoon Park, Changwoo Lee, "A 250-mm-Width, Flexible, and Continuous Roll-to-Roll Slot-Die Coated Carbon Nanotube/Silver Nanowire Film Fabrication and a Study on the Effect of Anti-reflective Overcoat," Thin Solid Films 598, 95-102(2016).

[26] Dong-Ju Kim, Hae-In Shin, Eun-Hye Ko, Ki-Hyun Kim, Tae-Woong Kim, Han-Ki Kim, "Roll-to-roll Slot-die coating of 400 mm Wide, Flexible, Transparent Ag Nanowire Films for Flexible Touch Screen Panels," Sci. Rep. 6, 34322 (2016).

[27] S. M. Raupp, L. Merklein, M. Pathak, P. Scharfer, W. Schabel, “An Experimental Study on the Reproducibility of Different Multilayer OLED Materials Processed by Slot Die Coating,” Chem Eng Sci. 160, 113-120 (2017).

[28] https://www.cambrios.com/technology-detail/technology/

[29] Goki Toshima, Takeo Tomiyama, “A New Touch-Panel Structure Using Metal Mesh and Ag Nanowire,” SID Symposium Digest of Technical Papers 47(1), 308-310 (2016).

[30] Manual available online at https://www.agilent.com/en/product/molecular-spectroscopy/uv-vis-uv-vis-nir-spectroscopy/uv-vis-uv-vis-nir-systems/cary-7000-universal-measurement-spectrophotometer-ums (Last accessed on 2021-02-27)

[31] Manual available online at https://www.jawoollam.com/products/rc2-ellipsometer (Last accessed on 2021-02-27)

[32] Description available online at https://www.jawoollam.com/ellipsometry-software/completeease (Last accessed on 2021-02-27)

[33] Manual available online at https://www.tokyoinst.co.jp/en/products/detail/evaluation_of_polarization/PX03/index.html (Last accessed on 2021-02-27)

[34] Shih-Yau Lu, Russell A. Chipman, “Interpretation of Mueller Matrices Based on Polar Decomposition,” J. Opt. Soc. Am. A. 13(5), 1106-1113 (1996).

[35] Manual available online at https://www.otsukael.com/product/detail/productid/19 (Last accessed on 2021-02-27)

[36] Description available online at https://www.labsphere.com/labsphere-products-solutions/materials-coatings-2/coatings-materials/spectralon/ (Last accessed on 2021-02-27)

Chapter 3

Relationship between structural, electrical, and optical anisotropy

3.1 Introduction

Recently, networks with highly aligned AgNW have been intensively studied, both theoretically and experimentally [1,2], because of an important property: in the direction of preferential alignment, low sheet resistance can be achieved without loss of transmittance. Fabrication methods for such networks include horizontal dip coating [3,4], grazing incident spraying [5,6], rod coating [7,8], roll coating [9], capillary printing [10,11], agitation-assisted assembly [12] or stretching [13-15]. However, these fabrication processes are often complex and unsuitable for large-scale production. For industrial and marketing purposes, TCFs with uniform sheet resistance, such as ITO films, are overwhelmingly desired, because the anisotropy of the sheet resistance can be ignored during electrode design. The TCTF that we developed (Chapter 2) exhibits a slight electrical anisotropy depending on the coating condition during the fabrication process. This motivated me to study the relationship between the AgNW orientation in the polymer matrix and optical and electrical anisotropy effects in the TCTF.

In this chapter, I characterize the AgNW angular distribution by dark-field optical

microscopic image analysis. Then, I analyze polarized optical spectra to define optical anisotropy and to examine the relationship between the structural, optical and electrical anisotropy. I base these analyses on Sample A1 and A2 (Table 2.1). The impact of the AgNW loading amount and the relationship between transmittance and sheet resistance are also discussed, using measurements of Samples B−F. This allows me to quantify structural and electrical anisotropy by optical analysis.

3.2 Structural anisotropy of AgNWs

In this section, I explore the structure of the AgNW network in TCTF samples. I analyzed microscope images and polarization spectra to determine the AgNW orientation and to define the structural anisotropy of the TCTF samples. I used Sample A1 and A2 for this analysis, because they contain the same AgNWs but exhibit slightly different properties (Table 2.1): the average sheet resistance is similar (56.2 and 46.8 Ω/sq.) but not the electrical anisotropy (1.17 and 1.47). Dark field optical microscope images of Samples A1 and A2 are shown in Figure 3.1.

First, to evaluate the angular distribution of the AgNWs, I derived the AgNW power spectrum by applying 2D fast Fourier transform (2D-FFT) algorithms to the dark-field images. The power spectrum of Sample A1 (Figure 3.2 (a)) is nearly featureless, due to the near-isotropic distribution of the AgNWs. In Sample A2, there is a noticeably brighter area along the vertical direction (Figure 3.2 (b)), indicating preferential AgNW orientation. Since the angular dependence of a power spectrum is perpendicular to the original image [16], I deduced that AgNWs in Sample A2 are preferentially oriented along the lengthwise direction of the TCTF.

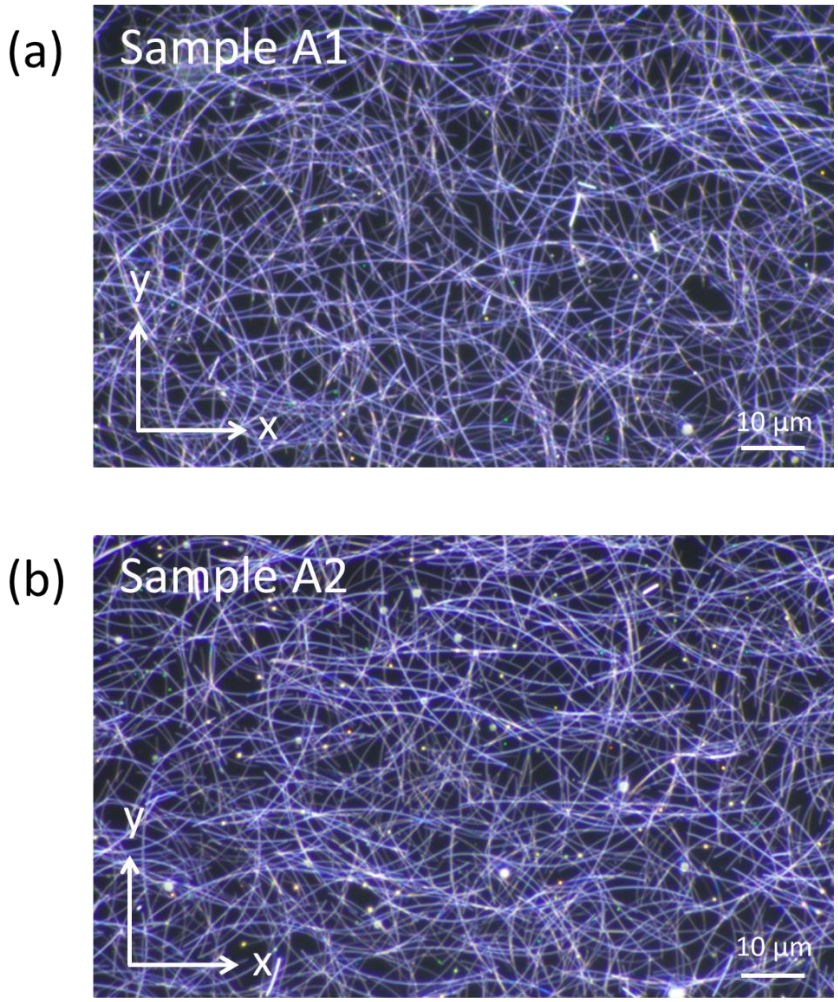

Figure 3.1 Dark field optical microscopy images of Samples (a) A1 and (b) A2. The x and y axes correspond to the lengthwise and crosswise directions of TCTF, respectively.

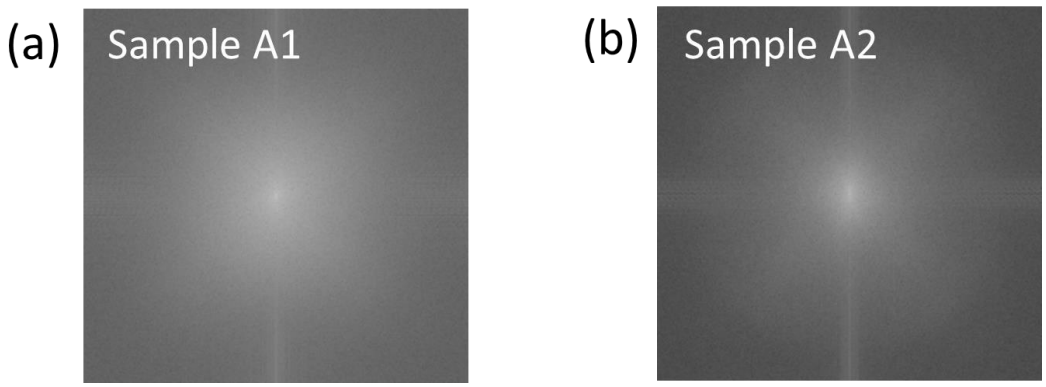

Figure 3.2 Power spectrum obtained by two-dimensional fast Fourier transform (2D-FFT) of Figure 3.1 for Samples (a) A1 and (b) A2.

For the next step, I quantified the AgNW angular distribution using the “OrientationJ” plug-in of the image analysis software “ImageJ” [17]. Forty dark field images of Sample A2 (Figure 3.3) were accumulated and processed by OrientationJ to obtain the radial sum of accumulated pixel intensities. The methodology used to validate quantification by “OrientationJ” is described in Appendix 1. Radial intensity was then normalized and plotted as a function of the radial angle θ. The reference ($\theta = 0°$) was set to the lengthwise TCTF direction. This radial intensity defines the AgNW angular distribution. Figure 3.4 shows the calculated AgNW angular distribution for Samples A1 and A2 in polar and Cartesian coordinates. As expected, the polar plot for Sample A1 shows a slightly flattened ellipse only (Figure 3.4 (a)), whereas the polar curve for Sample A2 is significantly stretched in the lengthwise direction (Figure 3.4 (b)). Similarly, the probability density function (PDF) of Sample A1 (Figure 3.4 (c)) is rather flat but that of Sample A2 shows a marked peak centered on zero (Figure 3.4 (d)).

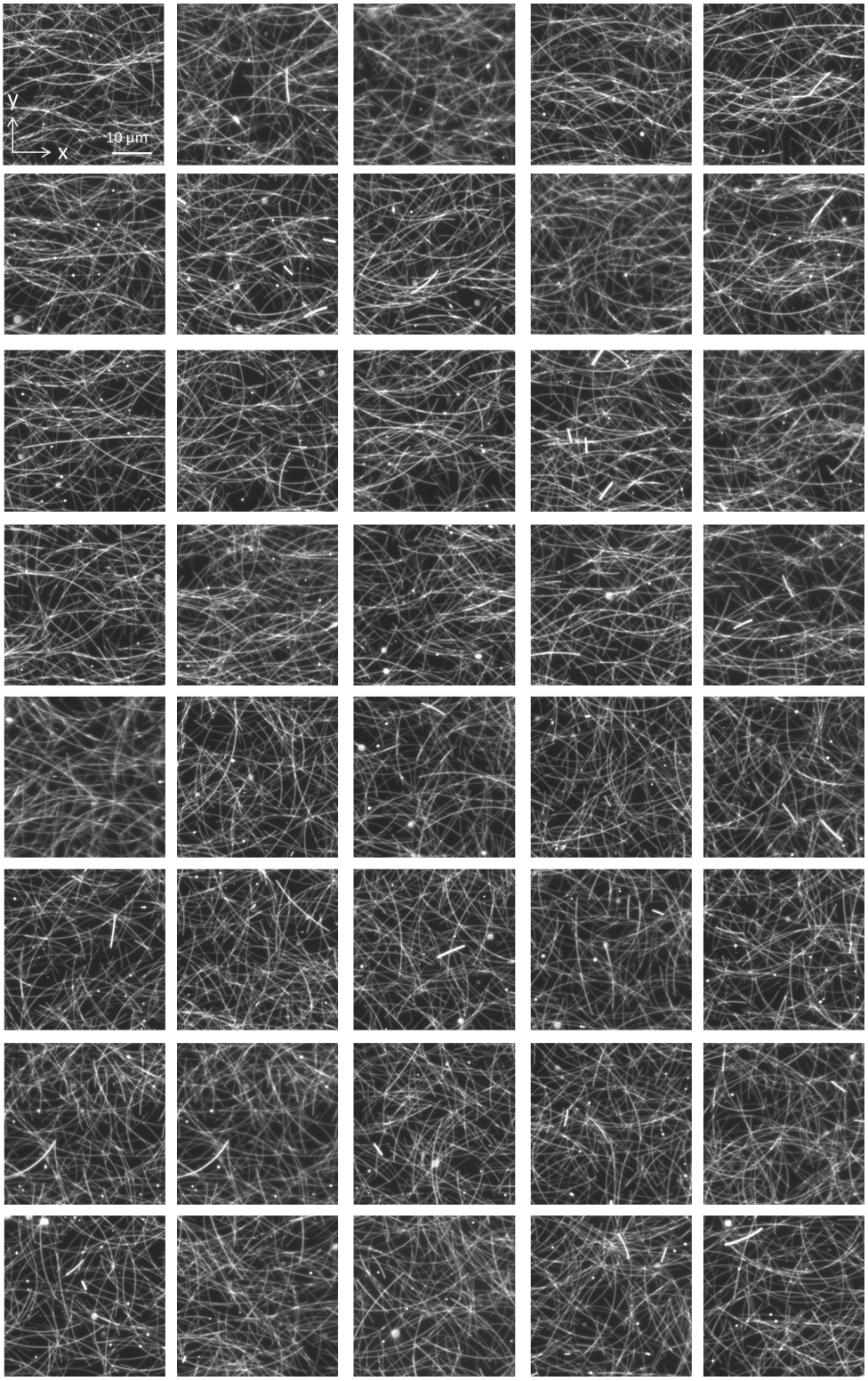

Figure 3.3 Dark field optical microscopy images of a set of A2-type samples used by the image analysis software.

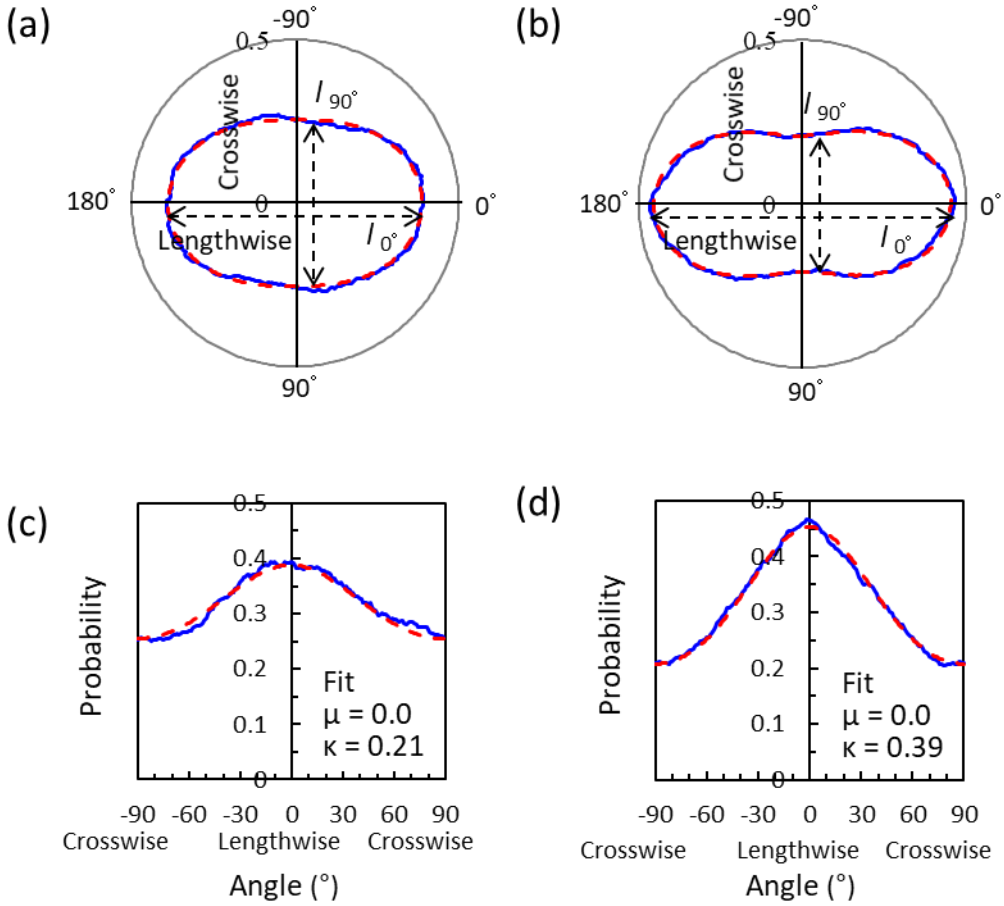

Figure 3.4 Angular distribution of the AgNW in (a)–(b) polar and (c)–(d) Cartesian coordinates for Samples A1 ((a), (c)) and A2 ((b), (d)), respectively. Blue lines represent the calculated AgNW angular distributions; red dashed lines show the fitting von Mises probability density functions (PDFs). The mean direction μ and concentration parameter κ of the PDFs are given in the plot.

To characterize the AgNW angular distribution in both samples, I fitted the results with two von Mises PDFs. The von Mises distribution is a circular analog of the Gaussian distribution defined by its mean direction μ and concentration parameter κ. In polar coordinates, the von Mises PDF for a polarization angle θ is given by:

$$f(\theta, \mu, \kappa) = \frac{\exp[\kappa \cos(2\theta - 2\mu)]}{\pi I_0(\kappa)}, \qquad 0 \le \theta \le \pi,\ 0 \le \mu \le \pi,\ \kappa \ge 0, \tag{3.1}$$

where $I_0(\kappa)$ is the modified Bessel function of the first kind of order 0,

$$I_0(\kappa) = \frac{1}{2\pi}\int_0^{\theta} \exp[\kappa \cos\theta]\, d\theta. \quad (3.2)$$

The quality of the fit was sufficient to extract the AgNW angular distribution parameters. For both samples, the estimated mean direction was close to 0°, confirming that AgNW are preferentially oriented along the lengthwise direction of the TCTF. The estimated concentration parameter values for Sample A1 and A2 were 0.21 and 0.39, respectively.

Lastly, I defined structural anisotropy as the ratio of the major axis to the minor axis ($l_{0°}/l_{90°}$) of the von Mises polar fitting curve. I calculated values of 1.52 and 2.20 for Samples A1 and A2, respectively. Since both samples contain the similar loading amount of AgNWs (Table 2.1), this confirmed the near-isotropy of Sample A1 and some degree of preferential orientation in Sample A2.

3.3 Optical anisotropy of AgNWs

Preferential AgNW orientation not only explains the structural anisotropy of the TCTF, but also influences its optical properties. In this section, I describe optical measurements, also of Samples A1 and A2, used to characterize optical anisotropy in the TCTF and to relate structural and optical anisotropies. For this analysis, I acquired polarized optical extinction spectra of Sample A1 and A2 for different in-plane polarization orientation. The measurement methodology was described in Section 2.4.1.

Spectra acquired at normal incidence show stronger polarization-dependent effects for Sample A2 (Figure 3.5 (b)) than for Sample A1 (Figure 3.5 (a)), like for structural anisotropy. Interference fringes, visible in all spectra, are caused by the thick (5 μm) polymer layer. Two distinctive spectral features, caused by LSPR of the AgNWs [18-20], are visible in Figure 3.5 for both samples. Firstly, an intense peak (dipole resonance) can be seen at 383 nm, with a shoulder (quadrupole resonance) at 360 nm. It is generated by the LSPR associated with AgNW polarization when the electric field vector of the incident light is perpendicular to the long axis of a nanowire (transverse mode). Secondly, a slight upward slope can be observed on all spectra in the NIR region. This occurs when

the incident light polarization is parallel to the long axis of an AgNW (longitudinal mode).

In the general case, extinction caused by polarized incident light can be expressed as:

$$\mathrm{Ext}(\varphi) = \mathrm{Ext}(0°)\cos^2\varphi + \mathrm{Ext}(90°)\sin^2\varphi, \quad (3.3)$$

where the polarization angle φ is the angle between the polarization vector and the lengthwise TCTF direction, and Ext(0°) and Ext(90°) are the orthogonal extinction components along the lengthwise and crosswise directions, respectively.

Figure 3.6 shows the extinction variations in the transverse (383 nm, near-UV) and longitudinal (average over 1400–2100 nm, NIR) modes with respect to the polarization angle. In the near-UV region, extinction increases from a minimum value for φ = 0° (lengthwise TCTF direction) to a maximum value for φ = 90° (crosswise direction). In the NIR region, the maximum is found at φ = 0° and the minimum at φ = 90°. This indicates that the longitudinal mode is strong in the lengthwise TCTF direction, whereas the transverse mode is stronger in the crosswise direction. Optical anisotropy is then defined as the maximum-to-minimum ratio of orthogonal extinction components, expressed as Ext(90°)/Ext(0°) for the transverse mode and Ext(0°)/Ext(90°) for the longitudinal mode. Taking the background polymer extinction into consideration, I calculated optical anisotropy values of 1.20 and 1.37 for Samples A1 and A2 in the transverse mode, respectively. In the longitudinal mode, I found values of 1.12 and 1.40 for Samples A1 and A2, respectively. In summary, the optical anisotropy of Sample A2 was consistently larger than that of Sample A1.

The next logical step for me was to relate the physical properties of the AgNW network (structural anisotropy) with the optical anisotropy in the TCTF. For simplicity, AgNWs are assumed here to be straight wires, with perpendicular long and short axes. Since their aspect ratio (length-to-diameter ratio) is sufficiently large (~10^3, see Table 2.1), I assumed that the extinction effects associated with the long and short axes of the AgNWs could be decoupled and that each nanowire is dichroic. The angular dependence of single-AgNW extinction in the longitudinal and transverse modes, respectively, is given by:

$$\mathrm{Ext}(\varphi) = \mathrm{Ext}(0°)\cos^2\varphi \quad \text{with } \mathrm{Ext}(90°) = 0 \quad \text{(longitudinal mode, NIR)} \quad (3.4a)$$

$$\mathrm{Ext}(\varphi) = \mathrm{Ext}(90°)\sin^2\varphi \quad \text{with } \mathrm{Ext}(0°) = 0 \quad \text{(transverse mode, near-UV)} \quad (3.4b)$$

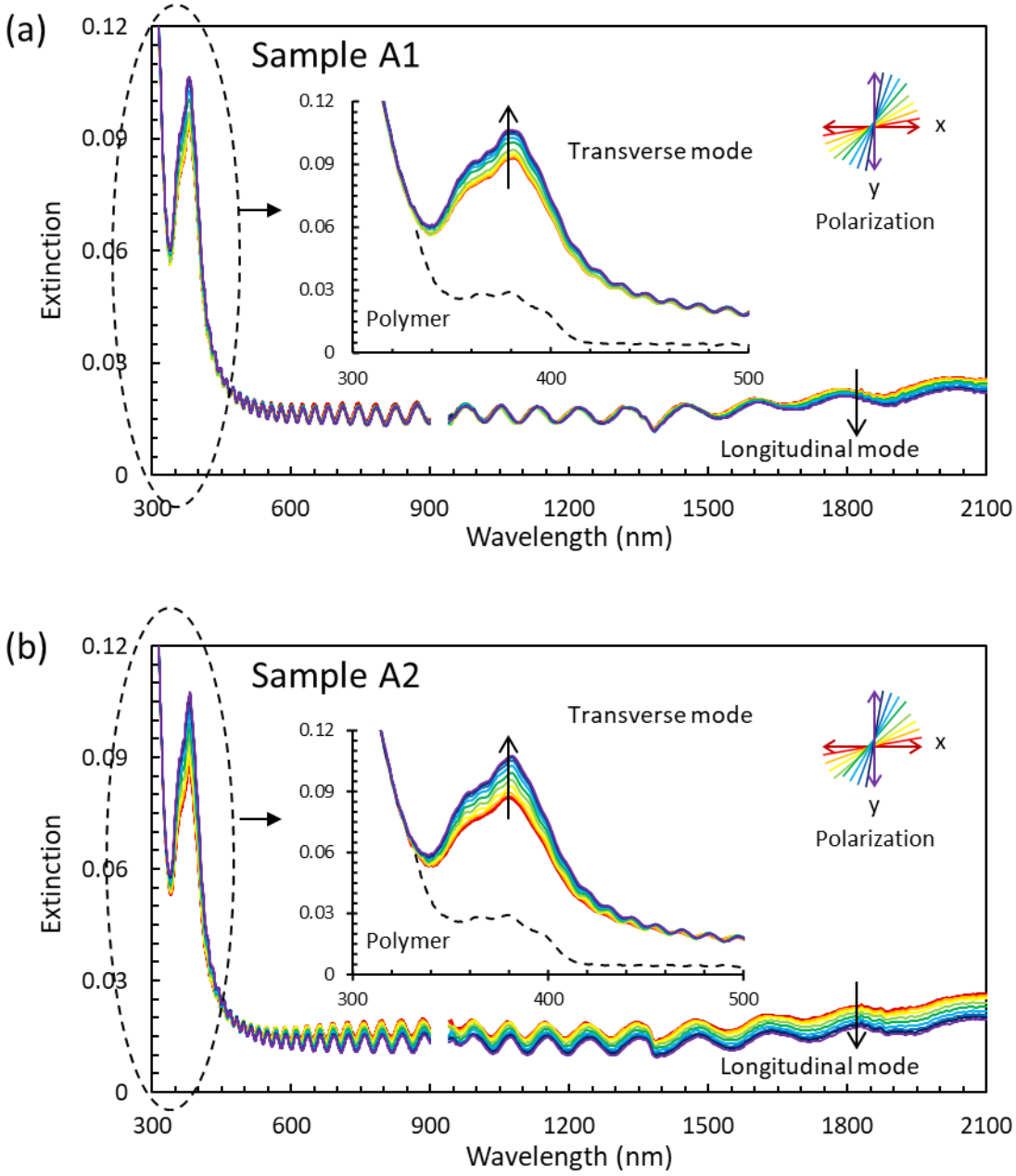

Figure 3.5 Normal-incidence polarized extinction spectra of Samples (a) A1 and (b) A2, respectively, as a function of the polarization angle. The inset spectra (center, top) show the transverse mode (300–500 nm) and the extinction spectrum of the polymer matrix (dashed line). Polarization directions are shown in the top right corner. The polarization angle varies by 15° between consecutive spectra, from the lengthwise (x, 0°, red line) to the crosswise (x, 90°, purple line) direction of the TCTF.

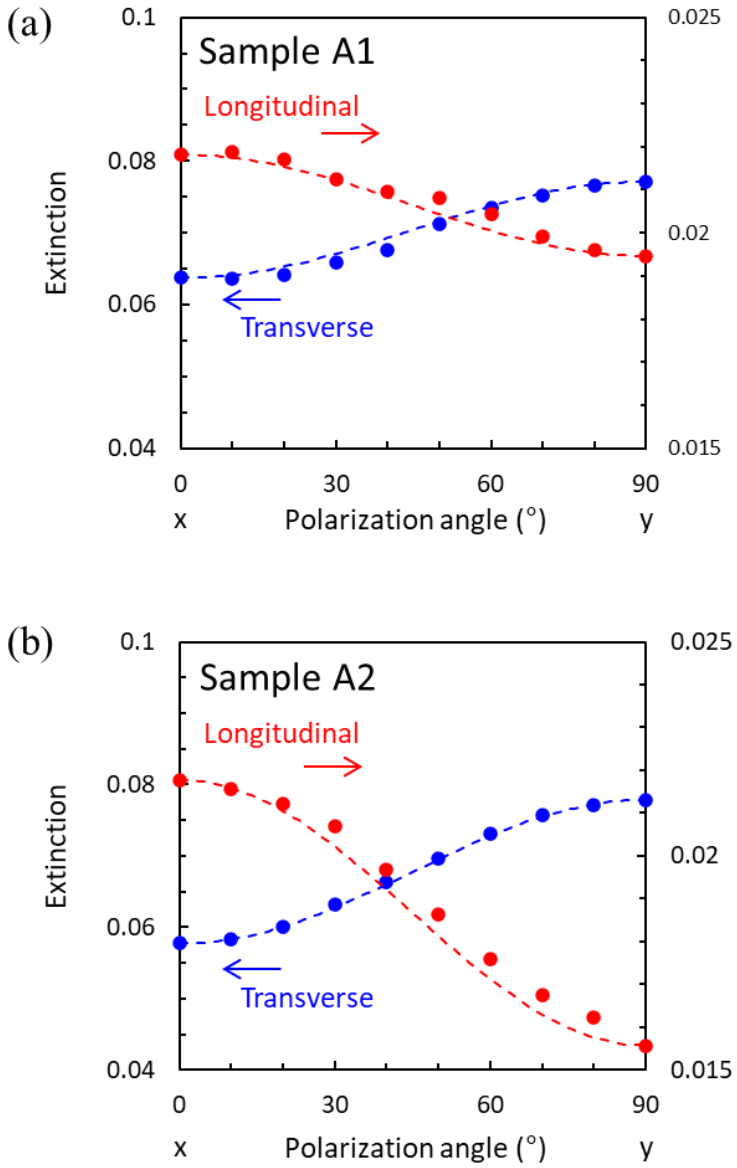

Figure 3.6 Average extinction of Samples (a) A1 and (b) A2, respectively, in the transverse (383 nm, near-UV) and longitudinal (average over 1400–2100 nm, near-IR) modes, as a function of the polarization angle. Transverse mode extinction calculations take the background polymer into consideration. The left axis corresponds to the transverse mode (blue) and the right axis to the longitudinal mode (red), respectively. The fitting function is defined by Equation (3.5). The lengthwise and crosswise TCTF directions are indicated by the "x" and "y" at $\varphi = 0°$ and $\varphi = 90°$, respectively.

Extinction of the AgNW ensemble consists of the interaction between the polarized incident light and the AgNWs with their individual orientation. If multiple scattering is not taken into account, angular dependence of the AgNW ensemble extinction can be expressed as follows:

$$F(\theta, \kappa) = \int_{-\frac{\pi}{2}}^{\frac{\pi}{2}} f(\theta, \mu, \kappa) \cos^2 \mu \, d\mu, \quad (3.5)$$

where f (θ, μ, κ) is the AgNW angular distribution (von Mises PDF with parameters μ and κ, Equation (3.1)) and $\cos^2\mu$ represents the angular dependence of single-AgNW extinction (Equation (3.4a)). I calculated the dependence of the ensemble extinction F(θ, κ) on the AgNW angular distribution f(θ,μ,κ) and plotted them for different values of the concentrate parameter κ (Figure 3.7 (a) and (b) for f(θ,μ,κ) and F(θ,κ), respectively). Their variations are similar: when κ increases, both increase in the lengthwise direction of the TCTF and decrease in the crosswise direction, respectively. The effect is smaller for the ensemble optical extinction than for the AgNW angular distribution. The structural (l(θ)/l(θ+90º)) and optical (Ext(θ)/Ext(θ+90º)) normalized orthogonal component ratios are shown in Figure 3.7 (c) and (d), respectively. Structural ($l_{0°}/l_{90°}$) and optical (Ext(0°)/Ext(90°)) anisotropy values for Samples A1 and A2 are also shown. Polarized optical spectroscopy measurements showed that optical anisotropy in the TCTF is smaller than structural anisotropy. This was confirmed by calculations with an image analysis tool based on Equation (3.5), which yielded values—1.23 and 1.47 for Samples A1 and A2, respectively—comparable to those obtained by spectroscopic measurements (1.12 and 1.40 for Samples A1 and A2, respectively, in the longitudinal mode). I was able to link the ensemble extinction to AgNW angular distribution, thereby establishing a connection between optical and structural anisotropy (Equation (3.5)) and confirming that multiple scattering did not need to be considered in samples A1 and A2.

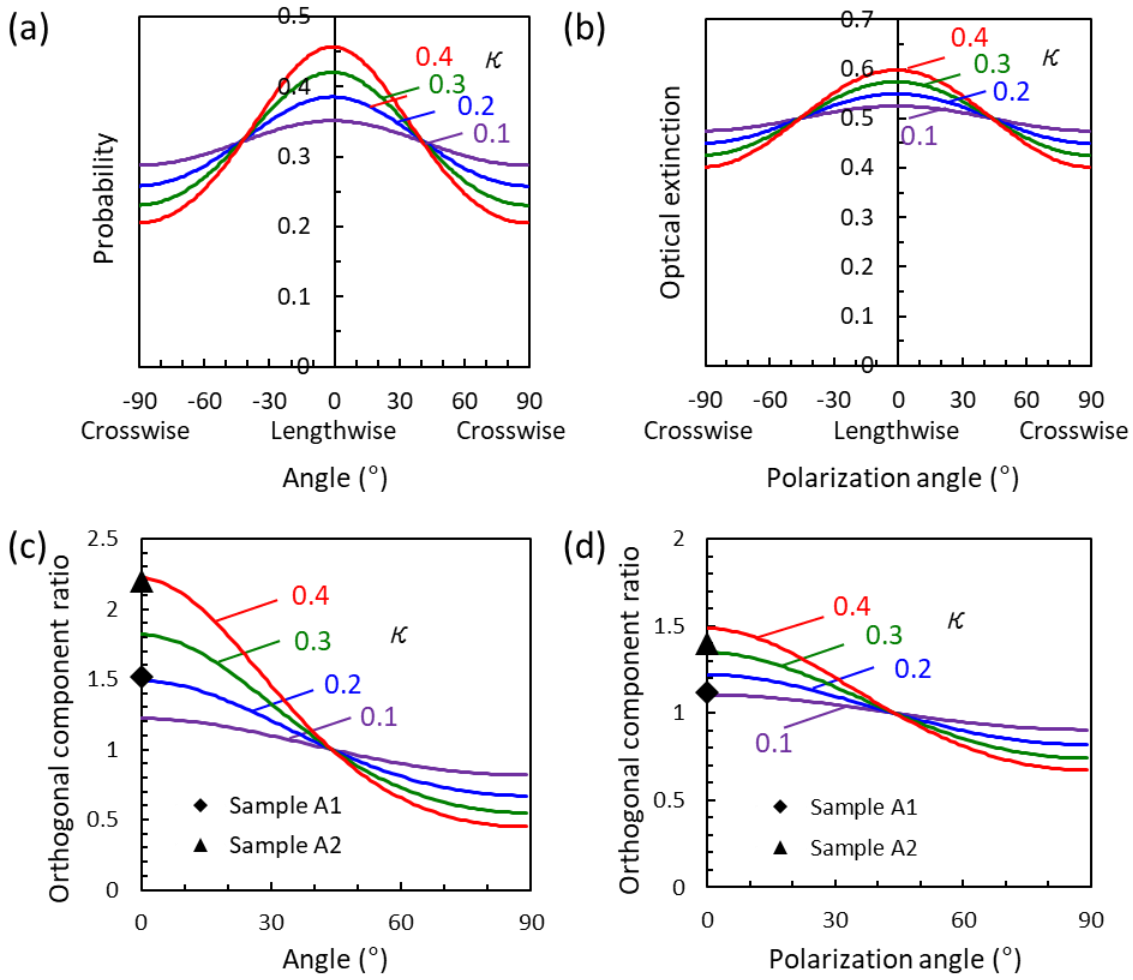

Figure 3.7 Calculated angular dependence of (a) AgNW orientation (a) and (b) ensemble AgNW extinction. Normalized ratios of orthogonal components for structural (l(θ)/l(θ+90º)) and optical (Ext(θ)/Ext(θ+90º)) anisotropies are shown in (c) and (d), respectively. Four von Mises PDFs are plotted in each panel, with μ = 0° and different values of κ: 0.1 (purple), 0.2 (blue), 0.3 (green) and 0.4 (red).

3.4 Electrical anisotropy of AgNWs

An important property of TCTFs is the dependence of the sheet resistance (Rs) on the measurement angle. It defines electrical anisotropy, therefore it needs to be fully characterized prior to any device application. In this section, I discuss sheet resistance

measurements of Samples A1 and A2, performed with the methodology described in Section 2.5.

Figure 3.8 (a) shows the measurement angle (θ) dependence of the sheet resistance for both samples, which is larger for Sample A2 than for Sample A1. This is similar to the results for optical extinction (Section 3.3). Minimum Rs values are found in the lengthwise TCTF direction (θ = 0°) and maximum values in the crosswise direction (θ = 90°) for both samples. Rs variations are symmetrical with respect to the lengthwise TCTF direction.

Using the same methodology as for optical extinction, I expressed the angular dependence of the sheet resistance as:

$$Rs(\theta) = Rs(0°)\cos^2\theta + Rs(90°)\sin^2\theta, \quad (3.6)$$

where θ is the measurement direction relative to the lengthwise TCTF direction, and Rs(0°) and Rs(90°) are the orthogonal components along the lengthwise and crosswise direction, respectively. Equation (3.6) is used to fit the experimental data (Figure 3.8 (a)) and is consistent with the measured Rs values.

The orthogonal component ratio, Rs(θ+90º)/Rs(θ), is shown in Figure 3.8 (b). Electrical anisotropy is then defined as the maximum-to-minimum ratio of orthogonal Rs components and expressed as Rs(90º)/Rs(0º). For Samples A1 and A2, I measured electrical anisotropy values of 1.17 and 1.47, respectively. Similarly, to optical anisotropy (previous section), Samples A2 shows a larger degree of electrical anisotropy than Sample A1. It is difficult to derive a simple equation to express electrical anisotropy from the AgNW angular distribution, because the sheet resistance of an ensemble of AgNWs is a complex quantity depending not only on the resistance of individual AgNWs, but also on the resistances of network junctions between neighboring AgNWs [2]. However, my experimental results showed that optical and electrical anisotropies are of comparable magnitude, and both smaller than structural anisotropy, although the phenomena that they represent are distinct.

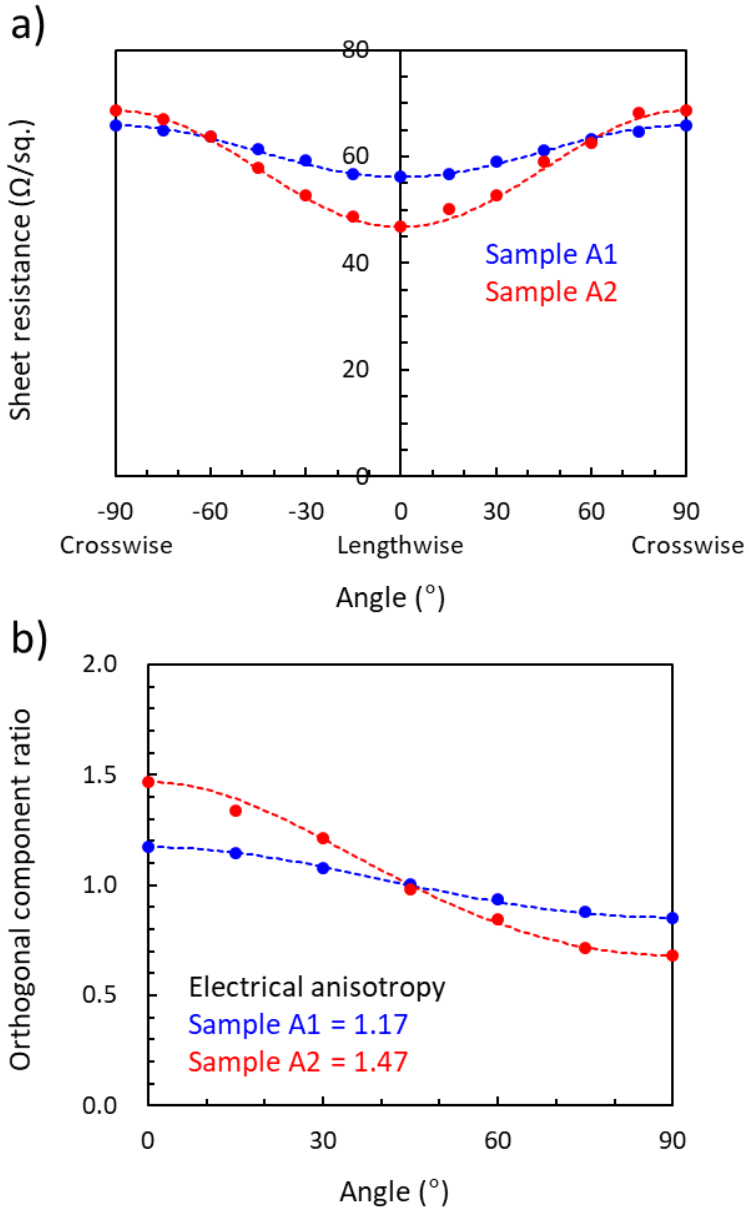

Figure 3.8 Dependence of (a) the sheet resistance (Rs) and (b) the ratio of orthogonal components, Rs(θ+90º)/Rs(θ) on the measurement angle, for Samples A1 (blue) and A2 (red). Measurements are taken every 15º. Electrical anisotropy (Rs(90º)/Rs(0º)) is shown by the black symbols in Panel (b) and values are given for both samples. The fitting function (dashed) is defined in Equation (3.6).

3.5 Influence of the AgNW loading amount

Because the optical and electrical properties of TCTFs logically depend on the quantity of AgNWs, I also investigated the influence of the AgNW loading amount on the extinction and sheet resistance of the TCTFs. For this purpose, Samples B–F were prepared with increasing loading amounts of the same AgNWs (Table 2.1). Figure 3.9 shows the variations of longitudinal mode optical extinction with the polarization angle. As the loading amount of AgNWs increases, extinction also increases, because AgNWs occupy a larger surface area within the polymer matrix. However, optical anisotropy is still observed for all samples.

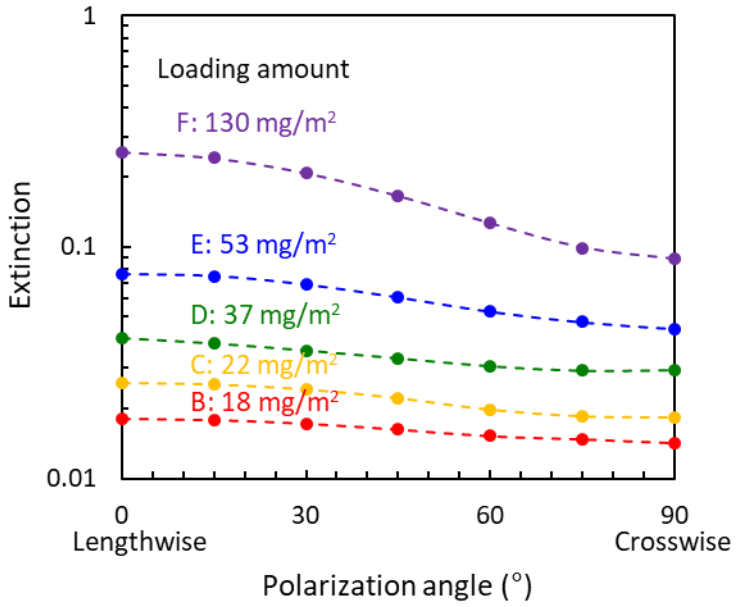

Figure 3.9 Dependence of the longitudinal mode extinction on the polarization angle for Samples B–F. The AgNW loading amount is indicated for each sample.

Figure 3.10 shows the measurement angle dependence of the sheet resistance Rs for Samples B–F. Rs decreases with increasing AgNW loading amounts because the potential number of conductive pathways increases. Interestingly, like optical anisotropy, electrical anisotropy is preserved when the quantity of AgNWs increases. This might be due to the fact that electrons diffuse preferentially along nanowires with fewer junctions, despite a

larger number of available conductive pathways. In other words, electrons diffuse preferentially along the length of an AgNW rather than moving to another. Accordingly, the sheet resistance of the AgNW network in a TCTF is dominated by junction resistance. This may be due to the dispersion agent or to the AgNW surface treatment agent.

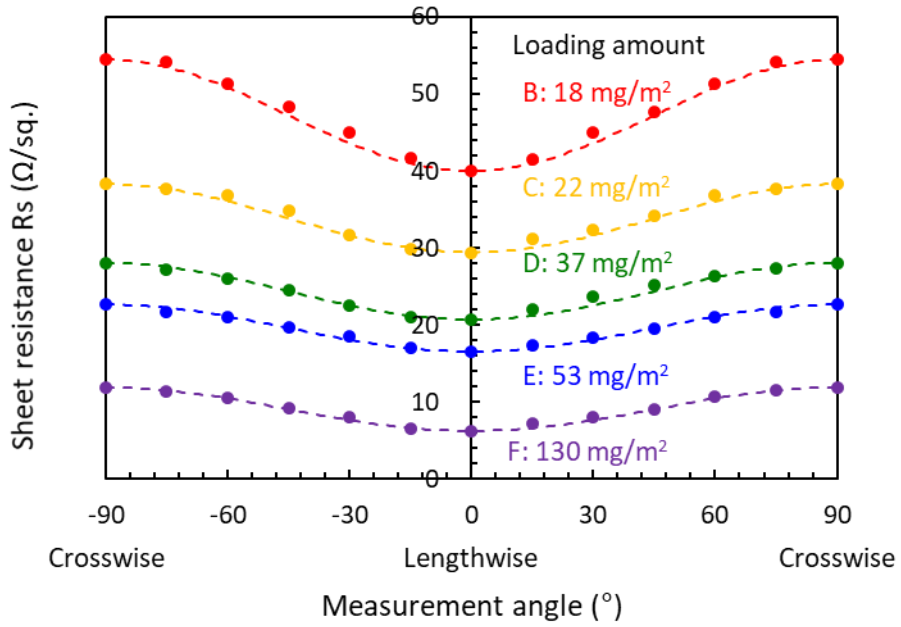

Figure 3.10 Same as Figure 3.8 (a) but for Samples B–F, measured every 15° from the lengthwise to the crosswise direction on either side (7 values per sample between 0° and ±90°, 13 in total). Color-coding is the same as in Figure 3.9. Loading amounts are also shown.

Figure 3.11 shows the relationship between the optical and electrical anisotropy for Samples B–F. When the AgNW loading amount is 37 mg/m^2 or less (Samples B–D), optical and electrical anisotropy are nearly equal (~1.5). Conversely, both anisotropies are significantly larger for loading amounts of 53 mg/m^2 or more (Samples E and F). A possible explanation is that, in densely packed networks, the orientation of AgNW is easily constrained by their neighbors during the coating process. On the contrary, in low-density networks, AgNWs are less constrained, allowing for a more random orientation during the coating process

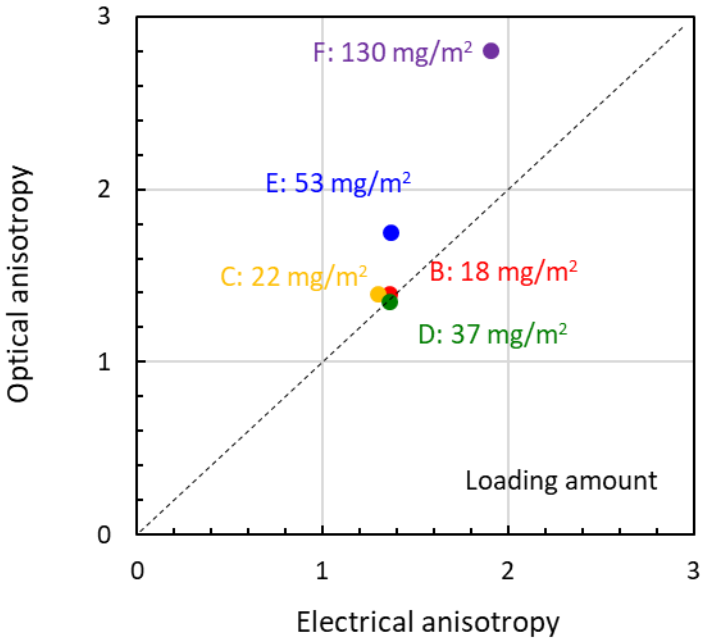

Figure 3.11 Relationship between optical and electrical anisotropy for Samples B–F, with the same color-coding as in Figure 3.9. Loading amounts are also shown.

3.6 Relationship between polarized transmittance and sheet resistance

Different methods can be used to characterize optoelectronic performance. The ratio of electrical to optical conductivity is often used as a figure of merit [21-23], an index that characterizes the performance of transparent electrode materials. For thin films, such as ITO films, this ratio is expressed as $\sigma_{DC,B}/\sigma_{OP}$ (where $\sigma_{DC,B}$ is the bulk direct current (DC) conductivity and σ_{OP} the optical conductivity) and is generally calculated at λ= 550 nm. Consequently, the transmittance T at a given wavelength can be expressed as a function of the conductivity ratio and of the sheet resistance Rs above the electrical percolation threshold [23]:

$$T(\%) = \left(1 + \frac{Z_0}{2R_S}\frac{\sigma_{OP}}{\sigma_{DC,B}}\right)^{-2} \times 100, \qquad (3.7)$$

where Z_0 is the impedance of free space (377 Ω). Large values of $\sigma_{DC,B}/\sigma_{OP}$ indicate high

transmittance and low sheet resistance.

Several studies have used this formula to describe optoelectronic performance of randomly oriented AgNW networks. Therefore, I decided to simultaneously analyze the polarized transmittance and sheet resistance for samples B–F as a function of the polarization angle (for transmittance) and of the measurement angle (for sheet resistance), with a 15° increment between 0° and 90° for both angles. Figure 3.12 shows the resulting polarized T and Rs pairs and the fitting curve (dashed line) defined by Equation (3.7). The fitting curve is a reasonable match for the measurement points pattern. Therefore, I deduced that, if the polarized transmittance along a given TCTF direction is known, the corresponding sheet resistance can be estimated without processing electrodes. By this method, electrical anisotropy can also be evaluated by optical analysis. This is a key finding of my analysis that will be beneficial for TCTF manufacturing process.

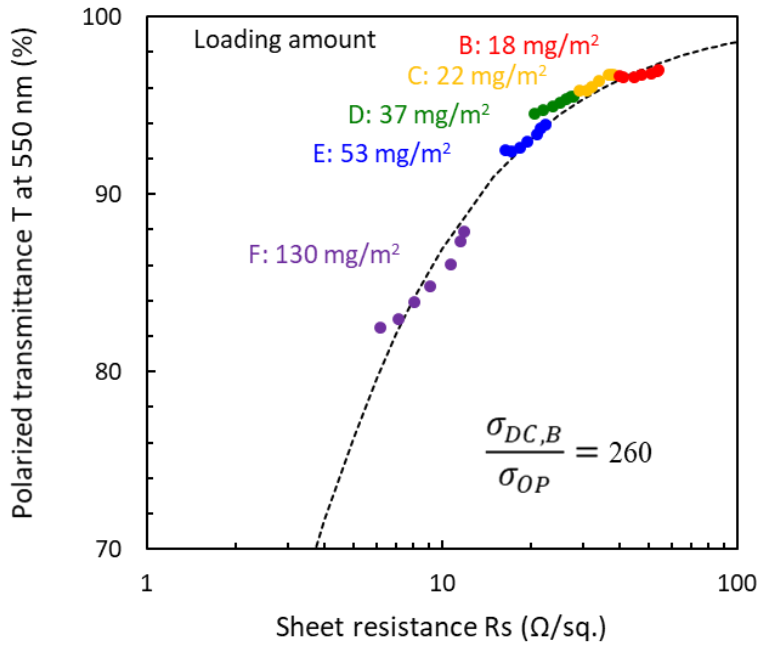

Figure 3.12 Polarized transmittance T at λ = 550 nm as a function of the sheet resistance Rs for Samples B–F. T is measured for different polarization angles and Rs for the same values of the measurement angle, both measured every 15° from the lengthwise to crosswise direction (7 values per sample between 0° and 90°). Color-coding is the same as in Figure 3.9. The fitting function (dashed line) is defined by Equation 3.7. The bulk-DC to optical conductivity ratio ($\sigma_{DC,\,B}/\sigma_{OP}$) is also given.

3.7 Conclusion for this chapter

In this chapter, I characterized and quantified the structural, optical and electrical anisotropy in the TCTFs. Optical and electrical anisotropies both depend on the angular distribution of AgNWs, which show preferential orientation (alignment of their long axis) in the lengthwise direction of the TCTF samples. Optical and electrical anisotropy values are both consistently smaller than structural anisotropy. Using von Mises PDFs to model the AgNW angular distribution, I showed that the ensemble extinction is related to structural anisotropy (expressed by the angular distribution) and to the angular dependence of single-AgNW extinction. Additionally, I established a relationship between electrical (measurement angle-dependent sheet resistance) and optical anisotropy (polarization angle-dependent polarized transmittance), which resembles the relationship between unpolarized transmittance and mean sheet resistance of isotropic AgNW networks. This is a significant finding that will allow me to estimate quantitatively the TCTF structural and electrical anisotropy by optical analysis.

3.8 References for Chapter 3

[1] Sadie I. White, Brian A. DiDonna, Minfang Mu, T. C. Lubensky, and Karen I. Winey, "Simulations and Electrical Conductivity of Percolated Networks of Finite Rods with Various Degrees of Axial Alignment," Phys. Rev. B 79, 024301 (2009).

[2] Milind Jagota, Nelson Tansu, "Conductivity of Nanowire Arrays under Random and Ordered Orientation Configurations," Sci. Rep. 5, 10219 (2015).

[3] Byoungchoo Park, In-Gon Bae, Yoon Ho Huh, "Aligned Silver Nanowire-Based Transparent Electrodes for Engineering Polarisation-Selective Optoelectronics," Sci. Rep. 6, 19485 (2016).

[4] Thomas Ackermann, Raphael Neuhaus, Siegmar Roth, "The Effect of Rod Orientation on Electrical Anisotropy in Silver Nanowire Networks for Ultra-transparent Electrodes," Sci. Rep. 6, 34289 (2016).

[5] H. Hu, M. Pauly, O. Felixa, G. Decher, "Spray-assisted Alignment of Layer-by-Layer Assembled Silver Nanowires: A General Approach for the Preparation of Highly Anisotropic Nano-Composite Films," Nanoscale 9, 1307-1314 (2017).

[6] Patrick T. Probst, Sribharani Sekar, Tobias A. F. König, Petr Formanek, Gero Decher, Andreas Fery, Matthias Pauly, "Highly Oriented Nanowire Thin Films with

Anisotropic Optical Properties Driven by the Simultaneous Influence of Surface Templating and Shear Forces," ACS Appl. Mater. Interfaces 10(3), 3046-3057 (2018).

[7] Jianjin Dong, Irene A Goldthorpe, "Exploiting both Optical and Electrical Anisotropy in Nanowire Electrodes for Higher Transparency," Nanotechnology 29(4), 045705 (2018).

[8] Seungse Cho, Saewon Kang, Ashish Pandya, Ravi Shanker, Ziyauddin Khan, Youngsu Lee, Jonghwa Park, Stephen L. Craig, Hyunhyub Ko, WLarge-Area Cross-Aligned Silver Nanowire Electrodes for Flexible, Transparent, and Force-Sensitive Mechanochromic Touch Screens," ACS Nano 11(4), 4346-4357 (2017).

[9] Yan-Ren Chen, Chien-Chong Hong, Tong-Miin Liou, Kuo Chu Hwang, Tzung-Fang Guo, "Roller-Induced Bundling of Long Silver Nanowire Networks for Strong Interfacial Adhesion, Highly Flexible, Transparent Conductive Electrodes," Sci. Rep. 7, 16662 (2017).

[10] Saewon Kang, Taehyo Kim, Seungse Cho, Youngoh Lee, Ayoung Choe, Bright Walker, Seo-Jin Ko, Jin Young Kim, Hyunhyub Ko, "Capillary Printing of Highly Aligned Silver Nanowire Transparent Electrodes for High-Performance Optoelectronic Devices," Nano Lett. 15(12), 7933-7942 (2015).

[11] Fan Wu, Zidong Li, Feng Ye, Xiaoli Zhao, Tong Zhang, Xiaoniu Yang, "Aligned Silver Nanowires as Transparent Conductive Electrodes for Flexible Optoelectronic Devices," J. Mater. Chem. C. 4(47), 11074-111080 (2016).

[12] Hebing Hu, Shichao Wang, Shancheng Wang, Guowei Liu, Tun Cao, Yi Long, "Aligned Silver Nanowires Enabled Highly Stretchable and Transparent Electrodes with Unusual Conductive Property," Adv. Func. Mater. 29, 1902922 (2019).

[13] Jinyang Feng, Xiao Ma, Haibo Mao, Baoshun Liu, "Ag/Epoxy Nanocomposite Film with Aligned Ag Nanowires and their Polarization Property," J. Mater. Res. 26(21), 2691-2700 (2011).

[14] Jaebeom Lee, Fangfang Sun, Jaewook Lee, "Fabrication of Large Area Flexible and Highly Transparent Film by a Simple Ag Nanowire Alignment," J. Exp. Nanosci. 8(2), 130-137 (2013).

[15] Xia Tong, Hongyan Liang, Yanlong Liu, Long Tan, Dongling Ma, Yue Zhao, "Anisotropic Optical Properties of Oriented Silver Nanorice and Nanocarrots in Stretched Polymer Films," Nanoscale 7(19), 8858-8863 (2015).

[16] Toshiharu Enomae, Yoon-Hee Han, Akira Isogai, "Nondestructive Determination of Fiber Orientation Distribution of Paper Surface by Image Analysis," Nord. Pulp. Pap. Res. J. 21, 253-259 (2006).

[17] R. Rezakhaniha, A. Agianniotis, J. T. C. Schrauwen, A. Griffa, D. Sage, C. V. C. Bouten, F. N. van de Vosse, M. Unser & N. Stergiopulos, "Experimental Investigation of Collagen Waviness and Orientation in the Arterial Adventitia Using Confocal Laser Scanning Microscopy," Biomech. Model. Mechanobiol. 11, 461-473 (2012).

[18] Quocanh N. Luu, Joshua M. Doorn, Mary T. Berry, Chaoyang Jiang, Cuikun Lin, P. Stanley May, “Preparation and Optical Properties of Silver Nanowires and Silver-nanowire Thin Films,” J. Colloid Interface Sci. 356(1), 151-158 (2011).

[19] Byoungchoo Park, In-Gon Bae, Yoon Ho Huh, “Aligned Silver Nanowire-Based Transparent Electrodes for Engineering Polarisation-selective Optoelectronics,” Sci. Rep. 6, 19485 (2016).

[20] Patrick T. Probst, Sribharani Sekar, Tobias A. F. König, Petr Formanek, Gero Decher, Andreas Fery, Matthias Pauly, “Highly Oriented Nanowire Thin Films with Anisotropic Optical Properties Driven by the Simultaneous Influence of Surface Templating and Shear Forces,” ACS Appl. Mater. Interfaces. 10(3), 3046-3057 (2018).

[21] Sukanta De, Thomas M. Higgins, Philip E. Lyons, Evelyn M. Doherty, Peter N. Nirmalraj, Werner J. Blau, John J. Boland, Jonathan N. Coleman, “Silver Nanowire Networks as Flexible, Transparent, Conducting Films: Extremely High DC to Optical Conductivity Ratios,” ACS Nano. 3, 1767-1774 (2009).

[22] TaeYoung Kim, Yeon Won Kim, Ho Seok Lee, Hyeongkeun Kim, Woo Seok Yang, Kwang S. Suh, “Uniformly Interconnected Silver‐Nanowire Networks for Transparent Film Heaters,” Adv. Funct. Mater. 23, 1250-1255 (2013).

[23] Sophie Sorel, Daniel Bellet, Jonathan N Coleman, “Relationship between Material Properties and Transparent Heater Performance for Both Bulk-Like and Percolative Nanostructured Networks,” ACS Nano. 8, 4805-4814 (2014).

Chapter 4

Optical anisotropy studies with Mueller matrix ellipsometry

4.1 Introduction

In Chapter 3, I quantified the in-plane (2D) structural anisotropy of the TCTF samples and defined its relationship with optical anisotropy. However, 3D anisotropy is also an important parameter for practical applications of AgNW-based TCFs. To fully understand the optical properties of a medium, accurate knowledge of its optical constants n (refractive index) and k (extinction coefficient) is fundamental. While abundant research on the optical constants of silver thin films [1-3] or silver nanoparticle arrays [4-8] is available, very little has been published on AgNW networks [9,10].

Ellipsometry is a metrology technique that measures changes of light polarization upon reflection on a medium. It is used to determine optical constants with high accuracy. Through successive developments, spectroscopic ellipsometry has evolved from the characterization of simple configurations (standard ellipsometry, Section 4.2.1) to a technique now capable of accurately characterizing complex structures and anisotropic materials (generalized and Mueller matrix ellipsometry, Sections 4.2.2 and 4.2.3, respectively). Light scattering in AgNW networks causes partial depolarization of the

TCTF. Therefore, simple ellipsometry is not appropriate for this investigation. For this reason, I used Mueller matrix spectroscopic ellipsometry to measure the optical constants of the TCTFs, because this technique can be applied to both isotropic and anisotropic samples with and without depolarization (for example, see [11] for its application to uniaxially self-assembled carbon nanotubes). In this chapter, I characterize the TCTF orthogonal optical constants with Mueller matrix ellipsometry and relate the 3D orientation of AgNWs in the polymer matrix to optical anisotropy within the TCTF.

4.2 Fundamentals of ellipsometry

4.2.1 Standard ellipsometry

Figure 4.1 shows the basic ellipsometry measurement principle (reproduced from [12]). Standard ellipsometry measures the ratio of the amplitude reflection coefficients, r_p/r_s, determined as:

$$\rho = \frac{r_p}{r_s} = \tan(\psi)e^{i\Delta} \quad , \tag{4.1}$$

where p and s represent orthogonal polarization directions parallel and perpendicular to the plane of incidence, respectively (hereafter "p-polarized" and "s-polarized"), and ψ (incoming-to-reflected amplitude ratio) and Δ (phase shift between the p and s reflected polarizations) are measurable ellipsometric variables. Standard ellipsometry assumes that there is no cross-polarization between p-polarized light and s-polarized light. In this case, the sample (reflecting medium) is described by a simple 2 x 2 diagonal Jones matrix:

$$\begin{pmatrix} E_p \\ E_s \end{pmatrix}_{out} = \begin{pmatrix} r_p & 0 \\ 0 & r_s \end{pmatrix} \begin{pmatrix} E_p \\ E_s \end{pmatrix}_{in} \tag{4.2}$$

Therefore, standard ellipsometry is only applicable to isotropic or uniaxially anisotropic samples in specific orientation conditions.

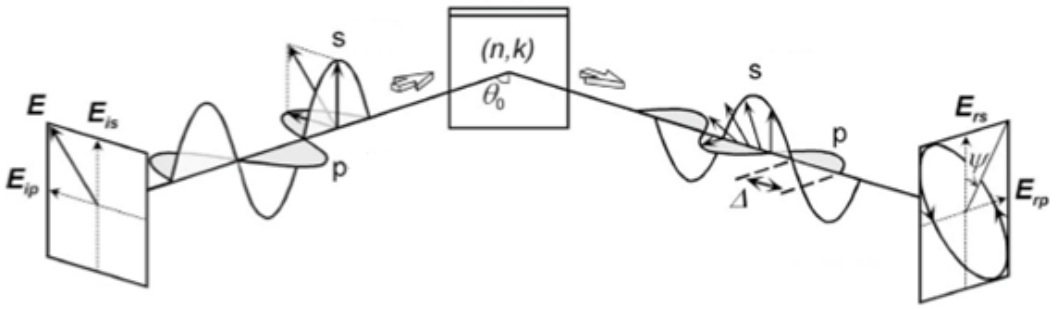

Figure 4.1 Principle of standard ellipsometry measurements (reproduced from [12]). E is the incident electric field with orthogonal components, E_{ip} and E_{is}, parallel and perpendicular to the plane of incidence, respectively. θ_0 is the angle of incidence on a medium characterized by its optical constants n (refractive index) and k (extinction coefficient). The amplitude ratio of the reflected electric field components, E_{rp} and E_{rs}, can be expressed as a function of the measurable ellipsometric quantities ψ and Δ.

4.2.2 Generalized ellipsometry

Generalized ellipsometry (GE) measurements require the complete Jones matrix of a sample, including the off-diagonal elements:

$$\begin{pmatrix} E_p \\ E_s \end{pmatrix}_{out} = \begin{pmatrix} r_{pp} & r_{sp} \\ r_{ps} & r_{ss} \end{pmatrix} \begin{pmatrix} E_p \\ E_s \end{pmatrix}_{in} \tag{4.3}$$

GE measurements themselves consist in calculating three ratios:

$$\rho = \frac{r_{pp}}{r_{ss}} = \tan(\psi)\, e^{i\Delta}, \tag{4.4}$$

$$\rho_{ps} = \frac{r_{ps}}{r_{pp}} = \tan(\psi_{ps})\, e^{i\Delta_{ps}}, \tag{4.5}$$

$$\rho_{ps} = \frac{r_{sp}}{r_{ss}} = \tan(\psi_{sp})\, e^{i\Delta_{sp}}, \tag{4.6}$$

where six variables need to be measured: ψ, Δ, ψ_{ps}, Δ_{ps}, ψ_{sp} and Δ_{sp}. GE measurements are useful for fully anisotropic samples, but they are not compatible with samples exhibiting depolarization, because GE formalism remains based on a Jones matrix.

4.2.3 Mueller matrix ellipsometry

Mueller matrices are 4 x 4 matrices that describe a linear relationship between the polarization states of the incident and reflected light beams. Their general expression is:

$$\begin{bmatrix} S_0 \\ S_1 \\ S_2 \\ S_3 \end{bmatrix}_{out} = \begin{bmatrix} M_{11} & M_{12} & M_{13} & M_{14} \\ M_{21} & M_{22} & M_{23} & M_{24} \\ M_{31} & M_{32} & M_{33} & M_{34} \\ M_{41} & M_{42} & M_{43} & M_{44} \end{bmatrix} \begin{bmatrix} S_0 \\ S_1 \\ S_2 \\ S_3 \end{bmatrix}_{in}, \tag{4.7}$$

where S_0, S_1, S_2 and S_3 are the Stokes parameters of the incident and reflected light.

The Mueller matrix formalism is based on measurable intensities and can be used to describe partially polarized or fully unpolarized light. In Mueller matrix ellipsometry, three parameters for isotropic samples (N, S, C) and seven for anisotropic samples (N, S, C, S_{ps}, C_{ps}, S_{sp}, C_{sp}) are measured [13]. The isotropic Mueller matrix is defined as:

$$M_{isotropic} = \begin{bmatrix} 1 & -N & 0 & 0 \\ -N & 1 & 0 & 0 \\ 0 & 0 & C & S \\ 0 & 0 & -S & C \end{bmatrix}. \tag{4.8}$$

N, S and C are given by:

$$N = \cos(2\psi), \tag{4.9}$$

$$S = \sin(2\psi)\sin(\Delta), \tag{4.10}$$

$$C = \sin(2\psi)\cos(\Delta), \tag{4.11}$$

where ψ and Δ are the ellipsometric angles defined in Section 4.2.1. In the anisotropic case, the Mueller matrix becomes [13]:

$$M_{anisotropic} = \begin{bmatrix} 1 & -N - \alpha_{ps} & C_{ps} + \zeta_1 & S_{sp} + \zeta_2 \\ -N - \alpha_{sp} & 1 - \alpha_{sp} - \alpha_{ps} & -C_{sp} + \zeta_1 & -S_{sp} + \zeta_2 \\ C_{ps} + \xi_1 & -C_{ps} + \xi_1 & C + \beta_1 & S + \beta_2 \\ -S_{ps} + \xi_2 & S_{ps} + \xi_2 & -S + \beta_2 & C - \beta_1 \end{bmatrix}. \tag{4.12}$$

(a)

$$M=\begin{pmatrix} 1 & M_{12} & 0 & 0 \\ M_{12} & 1 & 0 & 0 \\ 0 & 0 & M_{33} & M_{34} \\ 0 & 0 & -M_{34} & M_{33} \end{pmatrix}$$

(b)

$$M=\begin{pmatrix} 1 & M_{12} & M_{13} & M_{14} \\ M_{12} & M_{22} & M_{23} & M_{24} \\ -M_{13} & -M_{23} & M_{33} & M_{34} \\ M_{14} & M_{24} & -M_{34} & M_{44} \end{pmatrix}$$

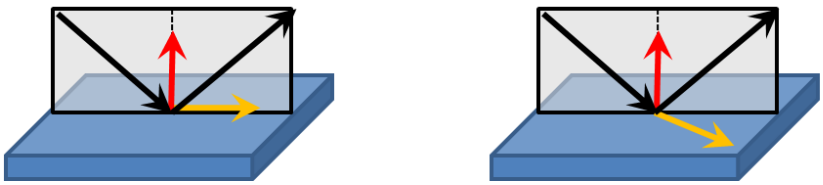

Figure 4.2 Reflection symmetries for Mueller matrix ellipsometry (adapted from [14]) at azimuth angles of (a) 0° and 90° (lengthwise and crosswise directions of the sample, respectively) and (b) 45°. Black arrows show the incident and reflected light directions in the incidence plane ("transparent" surface); the red arrow is the normal to the medium (represented in blue). Azimuth of the principal axis is shown by the yellow arrow.

Figure 4.2 summarizes the reflection Mueller matrix symmetries (adapted from [14]). These are oriented relatively to a sample of the medium being characterized, with the origin (0º) of the azimuth in the lengthwise direction of the sample. For parallel and perpendicular orientations (azimuths of 0º or 90º, respectively, Figure 4.2 (a)), the block diagonal elements M_{13}, M_{14}, M_{23}, M_{24} and M_{31}, M_{32}, M_{41}, M_{42} are zero. This means that, in this case, the medium sample is either isotropic or biaxial anisotropic with its principal axis along the lengthwise or crosswise direction, respectively. Alternately, in the case of a 45° orientation (Figure 4.2 (b)), all matrix elements are non-zero and some are related by $M_{21}=M_{21}$, $M_{31} = -M_{13}$, $M_{41} = M_{14}$, $M_{32} = -M_{23}$, $M_{42} = M_{24}$ and $M_{34}= -M_{43}$. This is the case of a biaxial anisotropic sample in which the azimuth of the principal axis is neither 0° nor 90°.

Mueller matrix measurements are especially useful when the sample is anisotropic and partially depolarized. In terms of experimental equipment, a dual-rotating-compensator ellipsometer was used to determine all elements of the Mueller matrix. The experimental set-up is described in Chapter 2 (Section 2.4.2).

4.3 Optical model description

To calculate the optical constants of the TCTF samples, I defined an optical model for the complete TCTF (Figure 4.3 (a) shows the TEM cross-section image of a real sample). An optical model is generally constructed as a stack of layers, each characterized by its thickness and optical constants and assumed to be homogeneous, with parallel interfaces. Layers are sequentially added on top of the substrate material. For this study, I devised a three-layer model consisting of a substrate layer, a polymer-only layer, and a conductive layer (Figure 4.3 (b)). Since AgNWs are embedded near the polymer surface, I define the thin conductive layer as a blend of AgNWs and polymer stacked on the thick polymer-only layer.

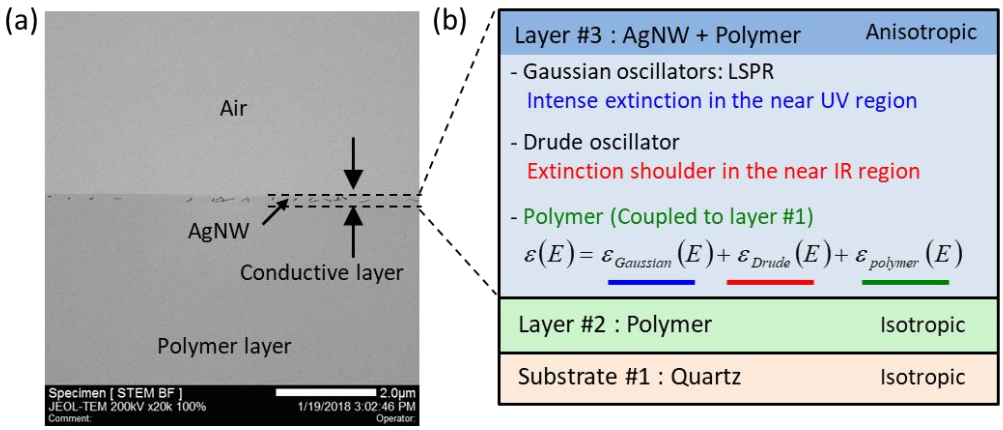

Figure 4.3 (a) TEM cross-section image of the TCTF highlighting the thin layer containing the AgNW network; (b) details of the optical model used in this ellipsometry analysis. The conductive layer model combines a set of Gaussian oscillators representing the polymer, two Gaussian oscillators for the LSPR of the transverse mode and a Drude oscillator for the longitudinal mode.

Before the analysis of the conductive layer itself, I determined the optical constants of the substrate and polymer layers separately and used them as fixed input parameters in the modeling. First, the optical constants of the substrate alone were determined. Then, those of the polymer layer were deduced from a substrate/polymer sample without AgNWs. Finally, the optical constants of the conductive layer were calculated using the

full optical model (substrate/polymer/conductive layer).

4.3.1 Quartz substrate

As described in Chapter 2, I used a quartz substrate for ellipsometry measurements. Quartz is transparent at visible wavelengths, so I applied the Cauchy dispersion equation (with three terms, Equation (4.13)) to calculate the refractive index of the substrate:

$$n(\lambda) = A + \frac{B}{\lambda^2} + \frac{C}{\lambda^4}, \tag{4.13}$$

where A, B, and C are fitting parameters. Standard ellipsometry was applied to measurements at incident angles between 50 and 75° every 5° (6 values in total).

4.3.2 Polymer layer

The dielectric function of the polymer is described using a set of Gaussian oscillators (with j elements) defined as:

$$\varepsilon_{Gaussian} = \mathrm{Amp}_j \left\{ \left[\Gamma\left(\frac{E-En_j}{\sigma_j}\right) + \Gamma\left(\frac{E+En_j}{\sigma_j}\right) \right] + i\left(exp\left[-\left(\frac{E-En_j}{\sigma_j}\right)^2 \right] + exp\left[-\left(\frac{E+En_j}{\sigma_j}\right)^2 \right] \right) \right\} \tag{4.14}$$

where j is the oscillator number, Amp_j is the amplitude of oscillator j, En_j the center energy, and σ_j the standard deviation. Assuming Equation (4.14) can be decomposed as $\varepsilon_{Gaussian} = \varepsilon_1 + i\varepsilon_2$, the Gaussian oscillator produces a Kramers-Kronig consistent line shape for ε_1 (Γ is a convergent series) and a Gaussian line shape for ε_2.

Like for the substrate, standard ellipsometry was used, at the same incident angles (50–75° at intervals of 5°). To improve the accuracy of the calculated extinction coefficient, I added the normal-incidence (θ_0 = 0°) transmission spectrum to each ellipsometry spectrum and fitted the six spectra simultaneously.

4.3.3 Conductive layer

The model for the conductive layer is more complex because it needs to combine the

polymer and the AgNWs. For this purpose, the dielectric function of the conductive layer is treated as an "effective medium approximation" (noted "EMA" in Table 4.1). The polymer component is described by a set of Gaussian oscillators (similarly to the thick polymer layer, Section 4.3.2). Transverse mode (near-UV) extinction is represented by two Gaussian oscillators, one for dipole resonance and one for the quadrupole (see Section 3.3 and Figure 3.5). Finally, Drude oscillators are used for the longitudinal mode extinction. They describe the effect of free carriers on the dielectric function and are defined as:

$$\varepsilon_{Drude} = \frac{-\hbar^2}{\varepsilon_0 \rho(\tau \mathrm{E}^2 + i\hbar \mathrm{E})}, \tag{4.15}$$

where ρ is the resistivity and τ the mean scattering time. ε_0 is the vacuum dielectric constant, ħ the reduced Planck constant and E represents energy. Resistivity is described as:

$$\rho = \frac{1}{\mathrm{q}\mu \mathrm{E}}, \tag{4.16}$$

where q is the electric charge and μ the carrier drift velocity.

The parameters of each oscillator were fitted separately in three orthogonal directions. Because the conductive layer shows some degree of anisotropy and depolarization, Mueller matrix ellipsometry was used for this analysis. Measurements were acquired at incidence angles of 50, 60 and 70º and for three azimuth settings: 0°, 45° and 90° (see Section 4.2.3). To improve the accuracy of the calculations, I combined the Mueller matrix spectra with four normal-incidence transmission spectra with distinct linear polarizations (T_{ss}, T_{sp}, T_{ps}, T_{pp}) and analyzed the samples simultaneously.

4.4 Determination of the optical constants

As explained above, I first measured the characteristics of the substrate and of the thick polymer layer separately, then used the results as input for the experimental characterization of the conductive layer. Figures 4.4 and 4.5 show the measurements and

model fitting for the quartz substrate.

Experimental and fitted values of ψ and Δ for the substrate are shown in Figure 4.4; the Cauchy model fitted the ψ (Figure 4.4 (a)) and Δ (Figure 4.4 (b)) spectra correctly at all wavelengths and incidence angles. In particular, for transparent materials, Δ should be 0° at angles higher than Brewster's (~56°) and 180° at lower angles, closer to normal incidence. Indeed, I found Δ = 180º for θ = 50º and 55º and Δ = 0° for other θ values (Figure 4.4 (b)). Figure 4.5 shows the spectral dependence of n and k for the substrate. As expected, normal dispersion (n decreasing with increasing wavelength) occurs throughout the spectrum but k is zero at all wavelengths.

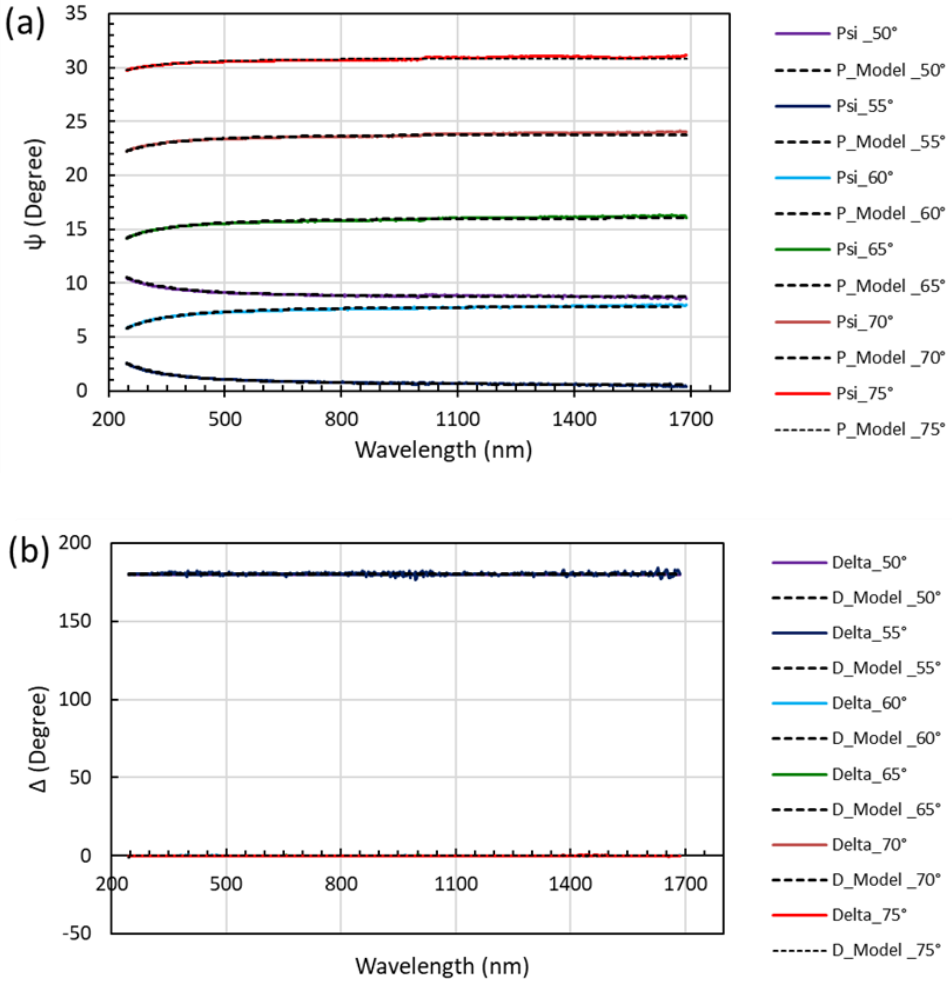

Figure 4.4 Spectral dependence of the ellipsometric parameters (a) ψ and (b) Δ for the quartz substrate. The calculated (solid) and fitted (dashed) values are shown for the incidence angles indicated in the legend on the right. The Δ value is 180° for θ = 50° and 55° (lower than Brewster's angle). For all other incidences, Δ = 0°.

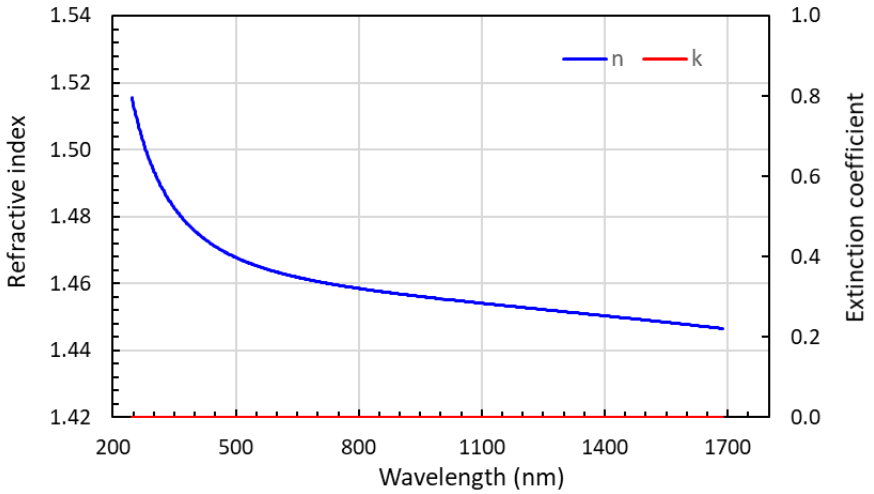

Figure 4.5 Spectral dependence of the optical constants (refractive index n and extinction coefficient k) for the quartz substrate, measured by standard ellipsometry.

Results for the polymer layer are shown in Figures 4.6–4.8. The spectra of ψ (Figure 4.6 (a)) and Δ (Figure 4.6 (b)) are very well fitted by the model. Interference fringes caused by the thickness of the polymer layer (5 μm) can be seen in all spectra. Like for the substrate, the normal-incidence transmission spectrum was added to the reflection spectra to increase calculation accuracy. Measured transmittance (and corresponding fit) is shown in Figure 4.7. Figure 4.8 shows the spectral dependence of n and k for the polymer. Using a set of four Gaussian oscillators (Equation 4.14) to express ε_2 (inset of Figure 4.8), the isotropic model yielded a sufficiently good fit for ψ and Δ (Figure 4.6) and for the transmittance (Figure 4.7) at all wavelengths and incidence angles. This confirms that the thick polymer layer is essentially isotropic and that optical anisotropy in the TCTF is caused by the conductive layer. The "shoulder" seen at near-UV and visible wavelengths in the ε_2 spectrum (Figure 4.8) is due to several UV-absorbing chromophores incorporated in the polymer.

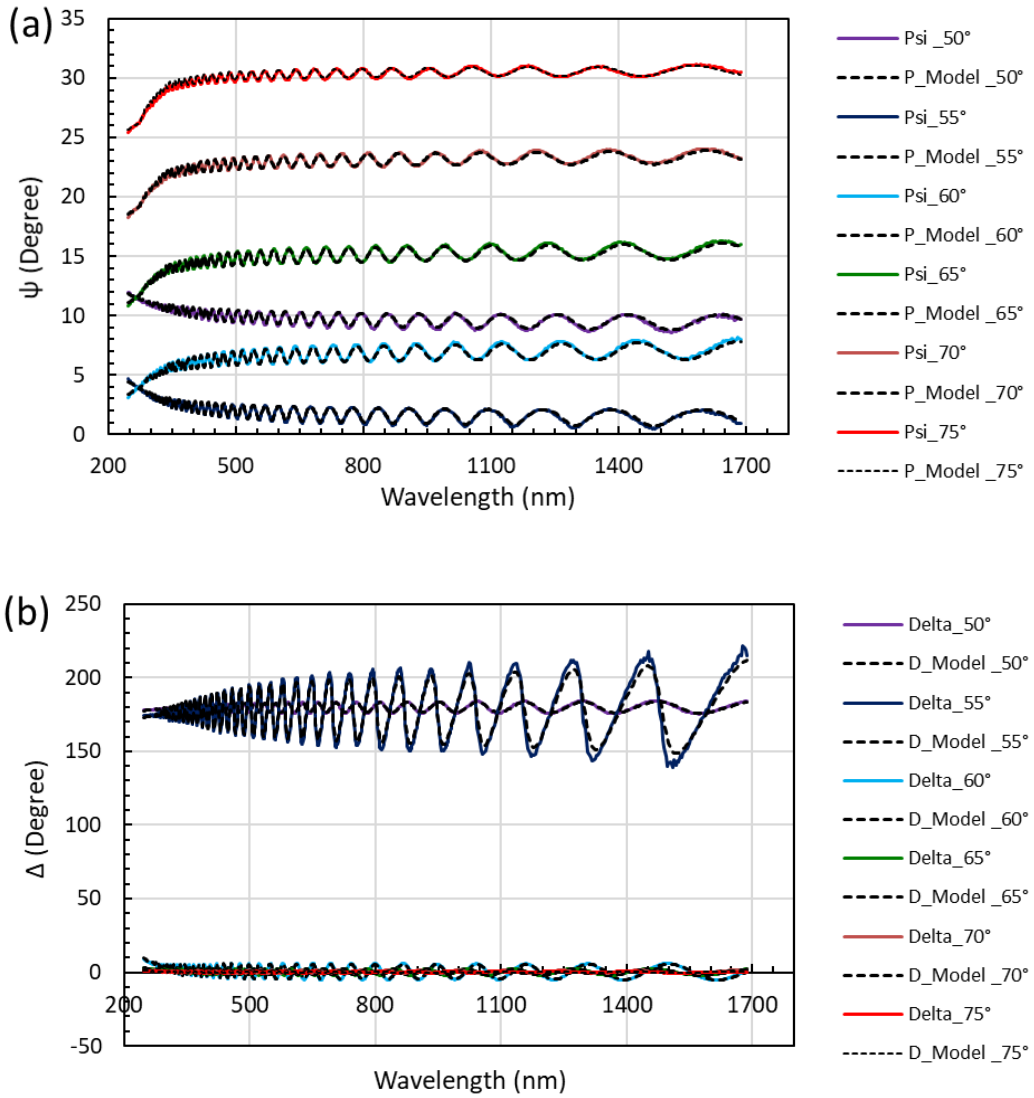

Figure 4.6 Same as Figure 4.4, but for the polymer layer. Interference fringes caused by the thickness of the polymer are visible on all spectra.

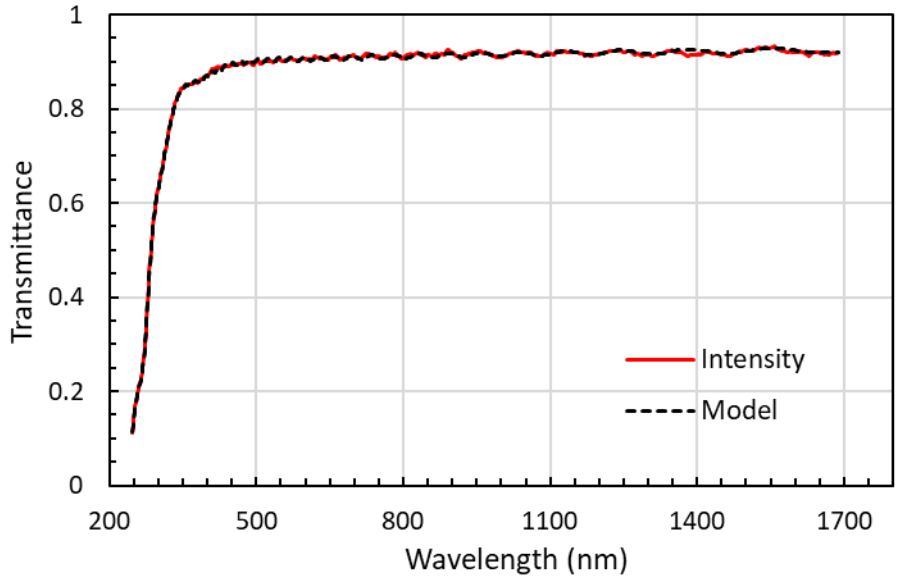

Figure 4.7 Normal-incidence transmission spectra of the polymer. Measured values are shown by the red line; the dashed line represents the fit.

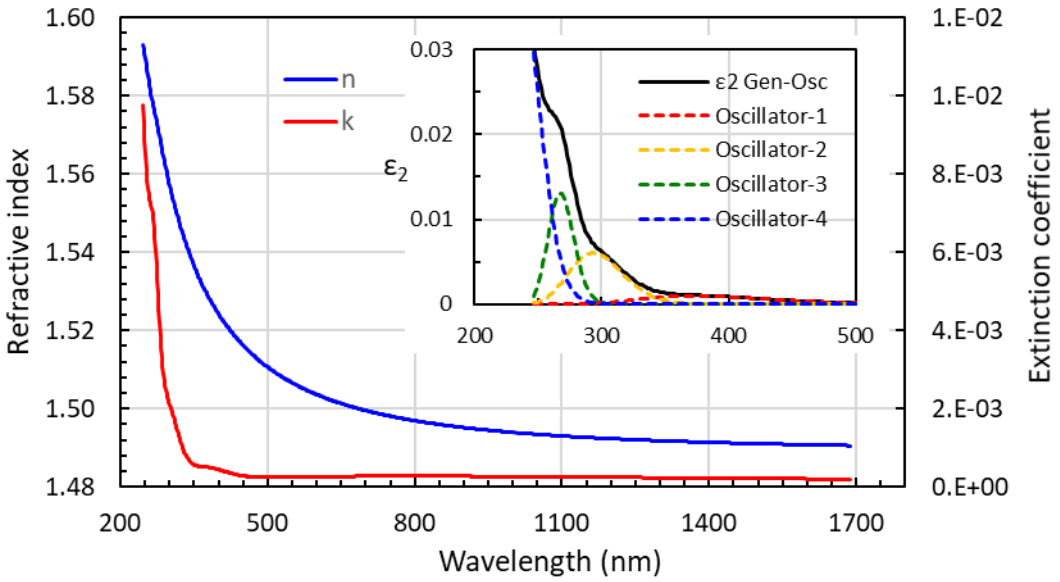

Figure 4.8 Same as Figure 4.5 but for the polymer. Inset shows the set of Gaussian oscillators (each defined as in Equation 4.14) used to represent the imaginary part (ε_2) of the dielectric function.

Using the substrate and polymer measurements as input in the optical model, I applied Mueller matrix ellipsometry to Sample A2 to characterize the conductive layer. Mueller matrix elements were first measured, then fitted with the optical model, for three incidence angles (50°, 60° and 70°) and for azimuths of 0°, 45° and 90° (Figure 4.9 (a)–(c)).

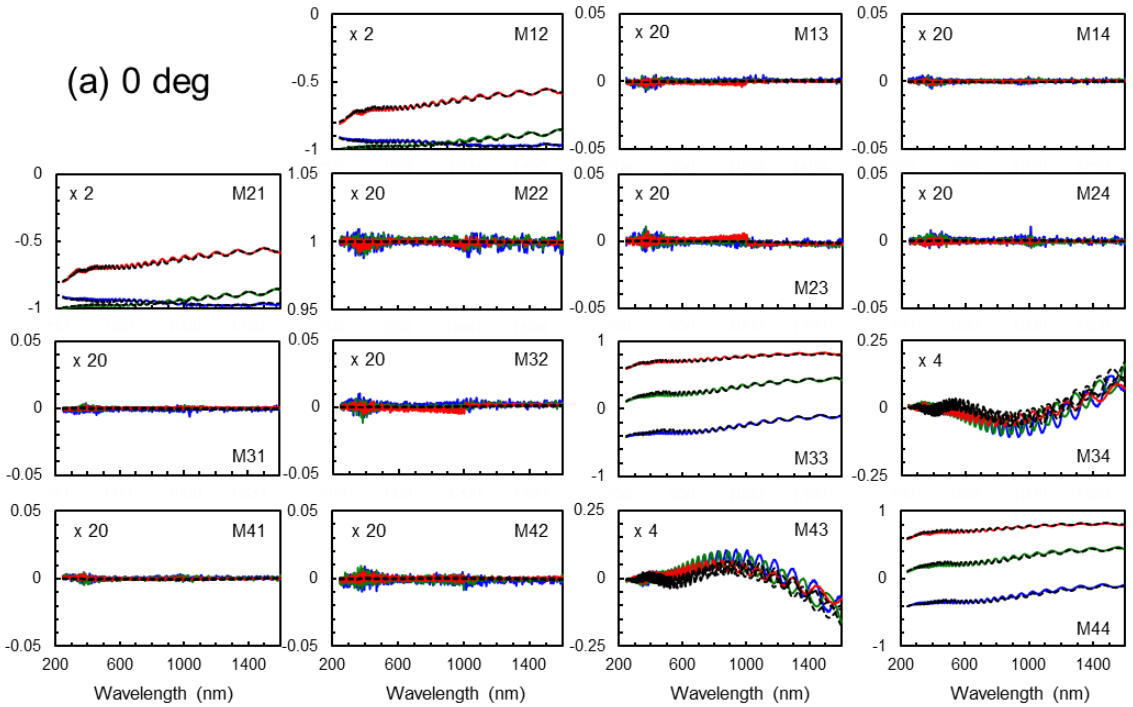

Figure 4.9 Measured spectra (near-UV to NIR) corresponding to the Mueller matrix elements of Sample A2 for different measurement angles (azimuth, measured from the lengthwise direction of the TCTF sample). Here (a) azimuth = 0°. Spectra are shown for incidence angles of 50° (blue), 60° (green), and 70° (red). Dashed lines (barely visible) give the fit for each spectrum. Vertical scale is increased for better visibility; multiplying factors are indicated in the top left corner for each matrix element.

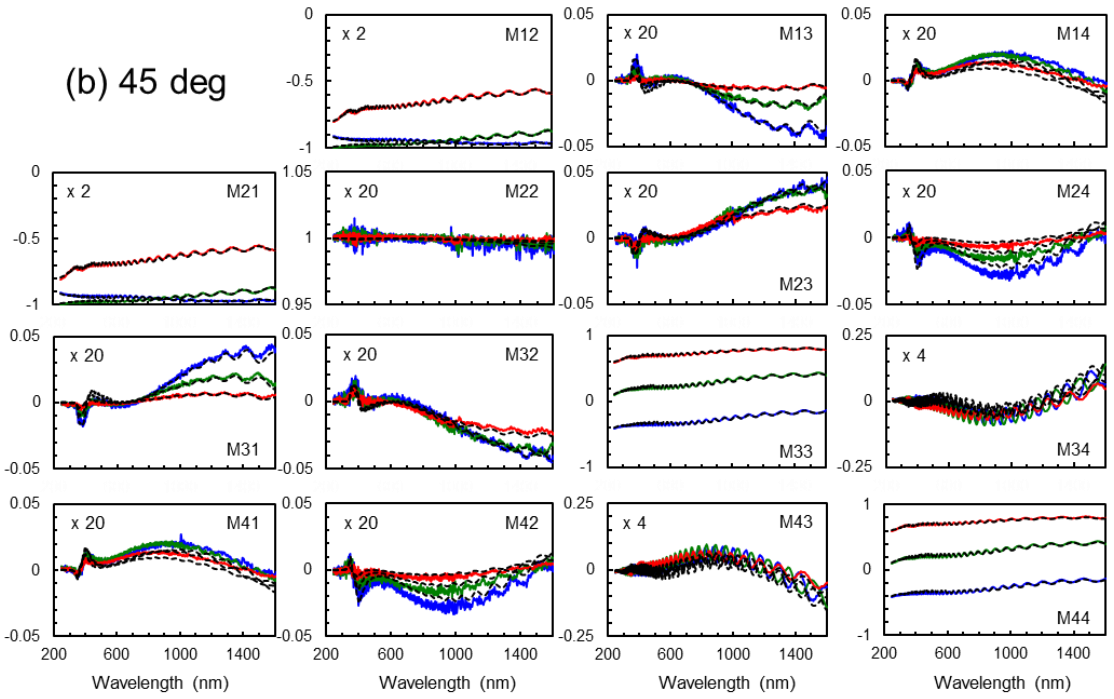

Figure 4.9, continued. (b) azimuth = 45°.

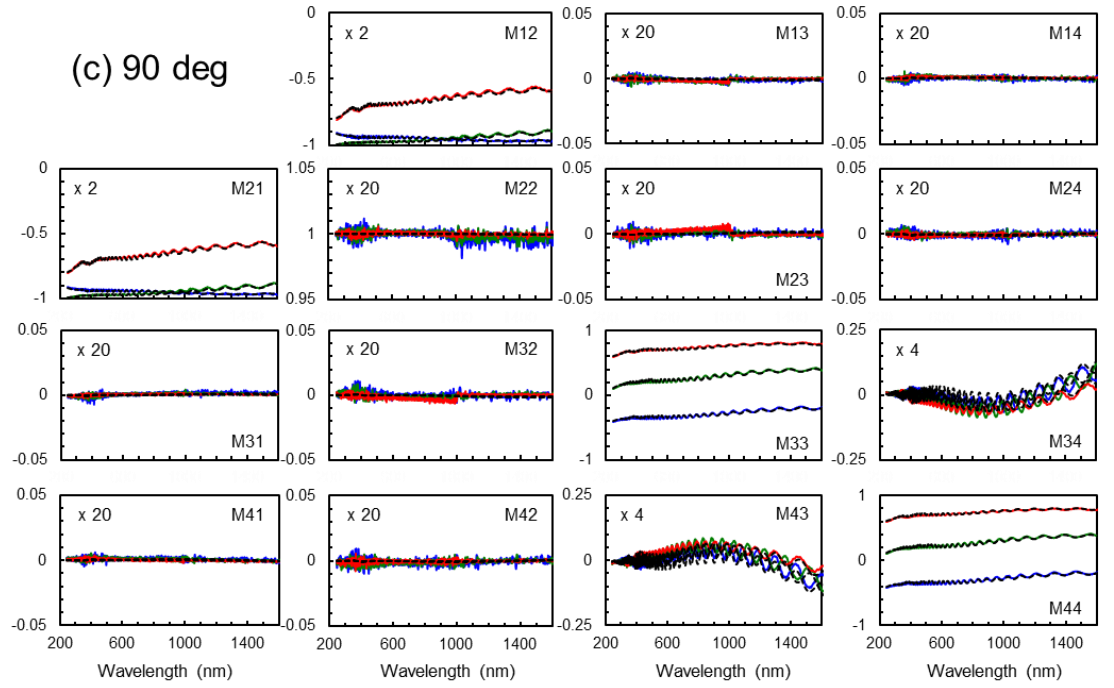

Figure 4.9, continued. (c) azimuth = 90°.

For azimuths of 0º and 90º (Figure 4.9 (a) and (c), respectively), the block diagonal elements (M_{13}, M_{14}, M_{23}, M_{24}) and (M_{31}, M_{32}, M_{41}, M_{42}) are nearly zero. For a 45° orientation (Figure 4.9 (b)), all matrix elements are non-zero and the spectra show that $M_{31} = -M_{13}$, $M_{41} = M_{14}$, $M_{32} = -M_{23}$ and $M_{42} = M_{24}$, which corresponds to biaxial anisotropy with a principal axis azimuth neither equal to 0° nor to 90°. The optical model yielded good fits for all spectra. According to the symmetry properties described in Section 4.2.3, I thus deduced that Sample A2 is, indeed, biaxial anisotropic with a principal axis oriented along its lengthwise direction.

Fitting parameters are gathered in Table 4.1 for all elements of the optical model. The effective thickness of the conductive layer estimated in this analysis is 257 nm, which is about eight times larger than the AgNW diameter for Sample A2 (33 nm, Table 2.1). This indicates that AgNWs are slightly tilted in the vertical direction.

Figure 4.10 shows the spectral dependence of optical constants determined for the conductive layer in orthogonal directions: lengthwise (x) and crosswise (y) directions within the sample and normal (z) to the sample surface. The observed spectral dependence of the dispersion curve is globally similar for the conductive layer and the polymer layer. This is reasonable because the conductive layer consists mostly of polymer with a low volume fraction of AgNWs. However, the refractive index variations are more complex than for the thick polymer layer because of the AgNW transverse and longitudinal extinction modes. Below 300 nm and above 400 nm, the expected monotonic spectral dependence associated with normal dispersion can be seen: n decreases with increasing wavelength. However, in the spectral range 300–400 nm around the transverse mode, anomalous dispersion occurs: n increases with wavelength. The extinction coefficient in the longitudinal mode (NIR region) is larger in the lengthwise direction than in the crosswise direction of the TCTF and nearly zero in the normal direction ($k_x > k_y$, $k_z = 0$). Conversely, the extinction coefficient in the transverse mode (near-UV) is largest along the normal, then in the crosswise direction, and smallest in the lengthwise TCTF direction ($k_z > k_y > k_x$).

Table 4.1 Fitting parameters for Sample A2 with the optical model of Section 4.4. Layer results are arranged as in Figure 4.3. Substrate and polymer layers analysis: standard ellipsometry; conductive layer analysis: Mueller matrix ellipsometry.

Conductive layer	Thickness: 257 nm						
	X-axis	X1: EMA(Material 1_Polymer/Material 2_AgNW_transverse)					
		Material 1	Polymer				
		Material 2	AgNW_transverse		UV Pole En: 15		
			AgNW-x1	Type: Gaussian	Amp: 6.8485	Br: 0.3399	En(eV): 3.223
			AgNW-x2	Type: Gaussian	Amp: 2.7804	Br: 0.1760	En(eV): 3.469
		EMA (Linear):0.7%_Material 2					
		X2: AgNW_longitudinal			UV Pole En: 11		
				Type: Drude	Resistivity(Ωcm): 0.0029	Scat. Time(fs): 8.055	
	Y-axis	Y1: EMA(Material 1_Polymer/Material 2_AgNW_transverse)					
		Material 1	Polymer				
		Material 2	AgNW_transverse		UV Pole En: 15		
			AgNW-Y1	Type: Gaussian	Amp: 10.8529	Br: 0.3399	En(eV): 3.223
			AgNW-Y2	Type: Gaussian	Amp: 4.6700	Br: 0.1760	En(eV): 3.469
		EMA (Linear):0.7%_Material 2					
		Y2: AgNW_longitudinal			UV Pole En: 11		
				Type: Drude	Resistivity(Ωcm): 0.0041	Scat. Time(fs): 8.039	
	Z-axis	Z1: EMA(Material 1_Polymer/Material 2_AgNW_transverse)					
		Material 1	Polymer				
		Material 2	AgNW_transverse		UV Pole En: 15		
			AgNW-Z1	Type: Gaussian	Amp: 15.7393	Br: 0.3399	En(eV): 3.223
			AgNW-Z2	Type: Gaussian	Amp: 4.4655	Br: 0.1760	En(eV): 3.469
		EMA (Linear):0.7%_Material 2					
		Z2: AgNW_longitudinal			UV Pole En: 11		
				Type: Drude	Resistivity(Ωcm): 1000	Scat. Time(fs): 1000	
Polymer layer	Thickness: 4940 nm						
			UV Pole Amp:	146.1763	UV Pole En: 11		
			Polymer				
			UV1	Type: Gaussian	Amp: 0.0010	Br: 1.0205	En(eV): 3.31
			UV2	Type: Gaussian	Amp: 0.0060	Br: 0.7099	En(eV): 4.223
			UV3	Type: Gaussian	Amp: 0.0131	Br: 0.4120	En(eV): 4.633
			UV4	Type: Gaussian	Amp: 0.0346	Br: 0.6934	En(eV): 5.2
Quartz	Thickness: 1 mm						
			Polymer				
				Type: Cauchy	A: 1.45	B: 0.00416	C: 0

To confirm my findings on the 3D orientation of AgNWs, I also derived useful extinction ratios: the lengthwise-to-crosswise ratio k_x/k_y and a "normal-to-planar" ratio: $k_z/\text{average}(k_x, k_y) = 2\ k_z/(k_x+k_y)$. Results are shown in Figure 4.11. Above 600 nm (longitudinal mode), k_x/k_y is almost constant ($k_x/k_y = 1.47$). This confirms preferential orientation of the AgNW long axis in the lengthwise direction. Furthermore, the normal-to-planar ratio value of 1.8 suggests that AgNWs are slightly tilted in the vertical direction, else it should be 2.0.

Finally, I studied the relationship between orthogonal components of n and k. Near the transverse mode (near-UV and short visible wavelengths, 380–460 nm), I found the same order for the refractive index, $n_z > n_y > n_x$, and the extinction coefficient, $k_z > k_y > k_x$. On the contrary, above 460 nm, the order is unchanged for refractive index components but reversed for the extinction coefficient: $k_x > k_y > k_z$. This behavior is due to the Kramers-Kronig relationship between k and n. These differences of refractive index components in orthogonal directions induce in-plane and out-of-plane retardation, which will be discussed in detail in Chapter 5.

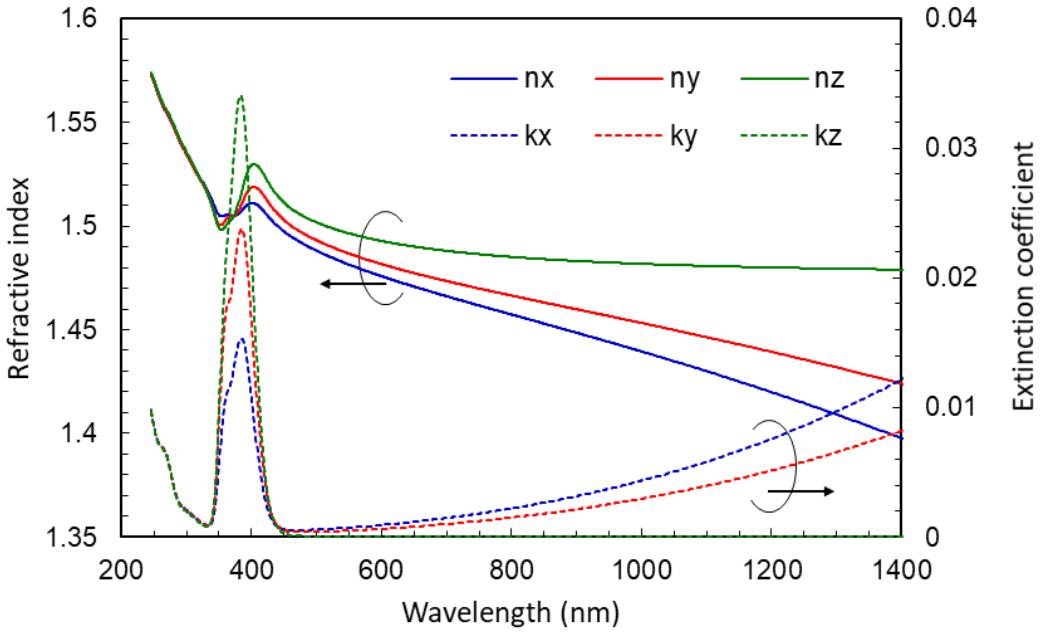

Figure 4.10 Same as Figure 4.5, but for the orthogonal optical constants of the conductive layer for Sample A2. The orthogonal directions x, y and z are the lengthwise and crosswise TCTF directions and the normal to the sample surface, respectively.

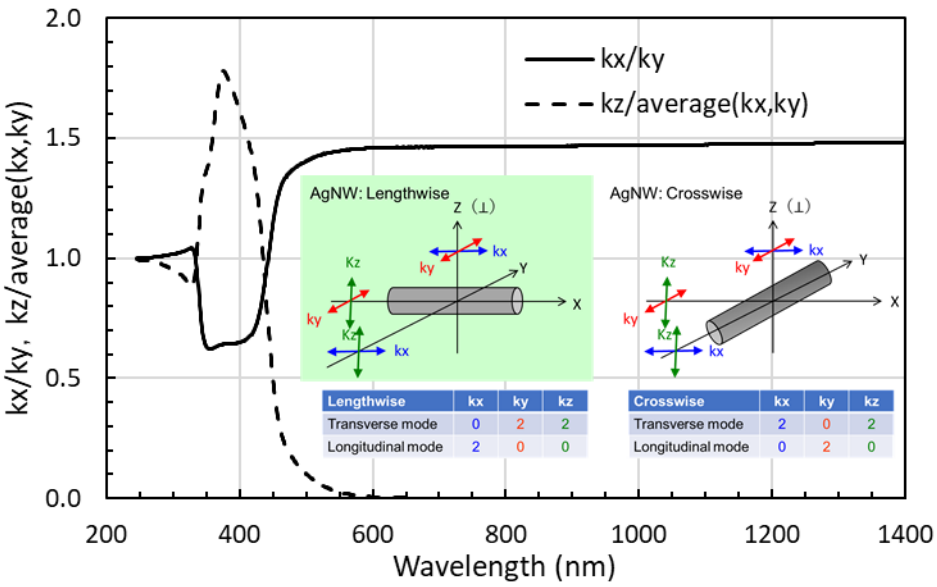

Figure 4.11 Spectral dependence of selected extinction ratios, k_x/k_y (solid line) and $2k_z/(k_x+k_y)$ (dashed line). Inset: relative amplitudes of all three orthogonal components in specific spatial configurations: AgNW oriented along the lengthwise or crosswise direction of the TCTF.

4.5 Conclusion for this chapter

In this chapter, I developed a dedicated optical model to analyze biaxial anisotropic AgNW networks by spectroscopic ellipsometry. After applying standard ellipsometry to the substrate and to the polymer layer, I determined the orthogonal optical constants of Sample A2 by Mueller matrix ellipsometry. I deduced that the spectral dependence of the orthogonal optical constants could be explained by the 3D morphology of the TCTF, in which AgNWs show in-plane anisotropy (with their long axis preferentially oriented in the lengthwise direction of the sample) and are slightly tilted in the vertical direction. Additionally, the dispersion curve of the refractive index for the conductive layer revealed in-plane and out-of-plane retardation.

4.6 References for Chapter 4

[1] Xilian Sun, Ruijin Hong, Haihong Hou, Zhengxiu Fan, Jianda Shao, “Thickness Dependence of Structure and Optical Properties of Silver Films Deposited by Magnetron Sputtering,” Thin Solid Films 515 (17), 6962-6966 (2007).

[2] A. I. Maaroof, G. B. Smith, “Effective Optical Constants of Nanostructured Thin Silver Films and Impact of an Insulator Coating,” Thin Solid Films 485(1-2), 198-206 (2005).

[3] Junbo Gong, Rucheng Dai, Zhongping Wang, Zengming Zhang, “Thickness Dispersion of Surface Plasmon of Ag Nano-Thin Films: Determination by Ellipsometry Iterated with Transmittance Method,” Sci. Rep. 5, 9279 (2015).

[4] Marsillac, S., Little, S.A., Collins, R.W., “A Broadband Analysis of the Optical Properties of Silver Nanoparticle Films by in Situ Real Time Spectroscopic Ellipsometry,” Thin Solid Films 519 (9), 2936-2940 (2011).

[5] Voue, M., Dahmouchene, N., De Coninck, J., “Annealing of Polymer Films with Embedded Silver Nanoparticles: Effect on Optical Properties,” Thin Solid Films 519 (9), 2963-2967 (2011).

[6] Thomas W. H. Oates, “Aligned Metallic Nanoparticles on Rippled Surfaces: Optical Characterization Using Generalized Ellipsometry,” Appl. Surf. Sci. 258 (23), 9278-9282 (2012).

[7] Mukesh Ranjan, Thomas W.H. Oates, Stefan Facsko, Wolfhard Möller, “Optical Properties of Silver Nanowire Arrays with 35 nm Periodicity,” Opt. Lett. 35(15), 2576-2578 (2010).

[8] Thomas W. H. Oates, Mukesh Ranjan, Stefan Facsko, Hans Arwin, “Highly Anisotropic Effective Dielectric Functions of Silver Nanoparticle Arrays,” Opt. Express 19 (3), 2014-2028 (2011).

[9] G. Khanarian, J. Joo, X.-Q. Liu, P. Eastman, D. Werner, K. O'Connell, P. Trefonas, “The Optical and Electrical Properties of Silver Nanowire Mesh Films,” J. Appl. Phys. 114, 024302 (2013).

[10] Xiaoming Yu, Xuan Yu, Jianjun Zhang, Yunqian Long, Dekun Zhang, “Optical Constants of Long Silver Nanowire Thin Films on Glass Calculated from the Transmission Spectra,” Mater. Lett. 194, 152-155 (2017).

[11] Stefan Schöche, Po-Hsun Ho, John A. Roberts, Shangjie J. Yu, Jonathan A. Fan, Abram L. Falk, “Mid-IR and UV-Vis-NIR Mueller Matrix Ellipsometry Characterization of Tunable Hyperbolic Metamaterials Based on Self-assembled Carbon Nanotubes,” J. Vac. Sci. Technol. B 38, 014015 (2020).

[12] Hiroyuki Fujiwara, "Spectroscopic Ellipsometry: Principles and Applications", John Wiley & Sons, Ltd., ISBN:9780470016084.

[13] Harland G. Tompkins, Eugene A. Irene, "Handbook of Ellipsometry", William Andrew Inc., ISBN 978-0-8155-1499-2.

[14] Oriol Arteaga, Ellipsometric Data Analysis: 2. Anisotropic materials, The 8th International conference on spectroscopic ellipsometry.

Chapter 5

Polarization properties of AgNWs

5.1 Introduction

Characterizing the polarization properties of TCFs, especially for use as a transparent conductive electrode (TCE) in touch screens, is of fundamental importance for industrial applications. For example, as LCDs became thinner, display structure shifted from the standard “out-cell” to an “in-cell” structure, where the TCE is placed between crossed linear polarizers [1]. In OLED displays, the TCE is placed under a circular polarizer to ensure anti-reflection on the metal electrode [2]. The polarization characteristics of a TCE cause undesirable effects such as “light leakage” of LCD dark screens or increased reflectance of OLED displays.

Pioneering studies have been published on polarization properties of spherical metal particles and metal nanorods [3-7], but none dedicated to AgNWs. Previous works on AgNW optical properties mainly discussed transmittance and haze [8-10] but did not include comprehensive explanation of their polarization properties, notably diattenuation, retardation and depolarization [11]. Diattenuation refers to differential attenuation (extinction) of orthogonal linear (horizontal/vertical or +45°/−45°) or circular (left/right) polarizations. Retardation is defined as a phase shift between orthogonal polarizations. Diattenuation and retardation are attributed to partial anisotropy of the AgNW network in

the TCTF. Depolarization is the loss of polarization due to randomization of polarization, as light scattering by the AgNWs induces partial depolarization of the TCTF. Evaluating these properties is critical to promote the industrial use of TCTFs in optoelectronic devices.

In this chapter, I characterize the TCTF polarization properties. I measure the Mueller matrices of several samples with a spectroscopic polarimeter and investigate the effects of the AgNW loading amount and diameter. I use the "polar decomposition method" to evaluate diattenuation and retardation in the TCTF [12]. I also devise an original "photometric method" to determine depolarization of the TCTF. Finally, I explore ways to reduce LCD light leakage in the "in-cell" configuration (sample between crossed linear polarizers). Taking into account the loading amount and diameter of AgNWs, I propose practical ways of reducing light leakage and evaluate their effectiveness.

5.2 Diattenuation, retardation and depolarization

Diattenuation and retardation are determined by polar decomposition of polarized Mueller matrix measurements (described in Chapter 2, Section 2.4.3). As will be shown in Section 5.3, depolarization of the TCTF samples used in this study is very small, hence the spectra derived from polar decomposition are extremely noisy. This motivated me to develop an original photometric method to quantify TCTF depolarization. The purpose of this section is to describe this method.

I postulate that the polarization Mueller matrix of a TCTF sample can be separated into three components, each representing a distinct effect of the sample on the incident light: linear diattenuation M_Δ, linear retardation M_R and depolarization M_D. The principal axis of each component is aligned with the lengthwise direction of the sample. The corresponding Mueller matrix decomposition is:

$$M(tmax, tmin, \delta, d_1, d_2, d_3) = M_\Delta(tmax, tmin) \cdot M_R(\delta) \cdot M_D(d_1, d_2, d_3), \quad (5.1)$$

where the components M_Δ, M_R and M_D are defined as:

$$M_{\Delta}(t_{max}, t_{min}) = \begin{pmatrix} \frac{tmax+tmin}{2} & \frac{tmax-tmin}{2} & 0 & 0 \\ \frac{tmax-tmin}{2} & \frac{tmax+tmin}{2} & 0 & 0 \\ 0 & 0 & \sqrt{tmax \cdot tmin} & 0 \\ 0 & 0 & 0 & \sqrt{tmax \cdot tmin} \end{pmatrix}, \quad (5.2)$$

$$M_R = \begin{pmatrix} 1 & 0 & 0 & 0 \\ 0 & 1 & 0 & 0 \\ 0 & 0 & \cos\delta & \sin\delta \\ 0 & 0 & -\sin\delta & \cos\delta \end{pmatrix}, \quad (5.3)$$

$$M_D = \begin{pmatrix} 1 & 0 & 0 & 0 \\ 0 & 1-d_1 & 0 & 0 \\ 0 & 0 & 1-d_2 & 0 \\ 0 & 0 & 0 & 1-d_3 \end{pmatrix}. \quad (5.4)$$

In these equations, tmax and tmin represent the maximum and minimum transmittance, δ the retardance and d_1–d_3 the degrees of depolarization for linear (d_1 for horizontal/vertical and d_2 for +45°/−45°) and circular (d_3) polarizations, respectively. The resulting depolarization factors are $(1-d_1)$, $(1-d_2)$ and $(1-d_3)$.

The global polarization Mueller matrix becomes:

$$M(tmax, tmin, \delta, d_1, d_2, d_3) =$$

$$\begin{pmatrix} \frac{tmax+tmin}{2} & \frac{tmax-tmin}{2} & 0 & 0 \\ \frac{(tmax-tmin)(1-d_1)}{2} & \frac{(tmax+tmin)(1-d_1)}{2} & 0 & 0 \\ 0 & 0 & \sqrt{tmax \cdot tmin}\cos\delta\,(1-d_2) & \sqrt{tmax \cdot tmin}\sin\delta\,(1-d_2) \\ 0 & 0 & -\sqrt{tmax \cdot tmin}\sin\delta\,(1-d_3) & -\sqrt{tmax \cdot tmin}\cos\delta\,(1-d_3) \end{pmatrix}. \quad (5.5)$$

For this analysis, I assume that each TCTF sample is placed between ideal linear polarizers. Two measurement configurations, corresponding to the horizontal/vertical linear case, are used: parallel, where both polarizers are oriented along the x axis of the reference frame, and crossed, where the first polarizer (on the incident side) is aligned with the x-axis and the second (transmission side) is perpendicular, along the y axis. The Stokes vectors of transmitted light in the parallel and crossed cases (S_0 and S_{90}, respectively) can then be described as:

$$S_0 = \begin{pmatrix} S_0^0 \\ S_0^1 \\ S_0^2 \\ S_0^3 \end{pmatrix} = P(q,r) \cdot M(tmax, tmin, \delta, d_1, d_2, d_3) \cdot P(q,r) \cdot \begin{pmatrix} 1 \\ 0 \\ 0 \\ 0 \end{pmatrix}, \text{ and} \quad (5.6)$$

$$S_{90} = \begin{pmatrix} S_{90}^0 \\ S_{90}^1 \\ S_{90}^2 \\ S_{90}^3 \end{pmatrix} = R(90°) \cdot P(q,r) \cdot R(-90°) \cdot M(tmax, tmin, \delta, d_1, d_2, d_3) \cdot P(q,r) \cdot \begin{pmatrix} 1 \\ 0 \\ 0 \\ 0 \end{pmatrix}. \quad (5.7)$$

In these equations, P(q, r) is the matrix representing the linear polarizers:

$$P(q,r) = \begin{pmatrix} \frac{q+r}{2} & \frac{q-r}{2} & 0 & 0 \\ \frac{q-r}{2} & \frac{q+r}{2} & 0 & 0 \\ 0 & 0 & \sqrt{qr} & 0 \\ 0 & 0 & 0 & \sqrt{qr} \end{pmatrix}, \quad (5.8)$$

where q and r are the maximum and minimum transmittance, respectively. The general expression of P derives from that of an ideal linear polarizer for which q = 1 and r = 0:

$$P(1,0) = \begin{pmatrix} \frac{1}{2} & \frac{1}{2} & 0 & 0 \\ \frac{1}{2} & \frac{1}{2} & 0 & 0 \\ 0 & 0 & 0 & 0 \\ 0 & 0 & 0 & 0 \end{pmatrix}. \quad (5.9)$$

Finally, $R(\theta)$ is the Mueller matrix of a rotator, with θ the rotation angle with respect to the lengthwise direction of the sample:

$$R(\theta) = \begin{pmatrix} 1 & 0 & 0 & 0 \\ 0 & \cos 2\theta & -\sin\theta & 0 \\ 0 & \sin 2\theta & \cos 2\theta & 0 \\ 0 & 0 & 0 & 1 \end{pmatrix}. \quad (5.10)$$

As a result, the total intensity (first element of the Stokes vector) of the transmitted light for the parallel and crossed configurations, respectively, is expressed as:

$$S_0^0 = 4\ tmax - 2\ tmax \cdot d_1, \text{ and} \quad (5.11)$$

$$S_{90}^0 = 2\ tmax \cdot d_1, \quad (5.12)$$

and the degree of depolarization, d_1, can be derived from S_0^0 and S_{90}^0 as:

$$d_1 = \frac{2}{1+\frac{S_0^0}{S_{90}^0}}. \quad (5.13)$$

The instrumental setup for depolarization measurements is given in Chapter 2, Section 2.4.4. In this analysis, the lengthwise direction of the TCTF was aligned with the transmission axis of the first (horizontal) linear polarizer to eliminate retardation effects.

5.3 Polarization properties

5.3.1 Mueller matrix measurements

To evaluate TCTF polarization properties, transmission Mueller matrices were measured at normal incidence for each sample. Figure 5.1 shows the 16 Mueller matrix elements of Sample F measured at azimuths of 0°, +45° and +90°, with the origin (0°) along the lengthwise direction of the TCTF sample.

At azimuths of 0° and 90°, the off-diagonal blocks (M_{13}, M_{14}, M_{23}, M_{24}) and (M_{31}, M_{32}, M_{41}, M_{42}) show near-zero values at all wavelengths. This confirms that the principal axes of the TCTF are aligned with the lengthwise and crosswise directions. Non-zero values measured for the symmetric pairs M_{12}/M_{21} (azimuths 0° and 90°) and M_{13}/M_{31} (azimuth 45°) indicate that Sample F shows linear diattenuation. Similarly, non-zero values for M_{34}/M_{43} (at 0° and 90°) and M_{24}/M_{42} (at 45°) are indicative of linear retardation. Finally, the near-zero values for the M_{14}/M_{41} and M_{23}/M_{32} pairs at all wavelengths indicate that circular polarization effects can be neglected. For the next sections, I used the polar decomposition of the Mueller matrix elements to quantify diattenuation and retardation of the TCTF.

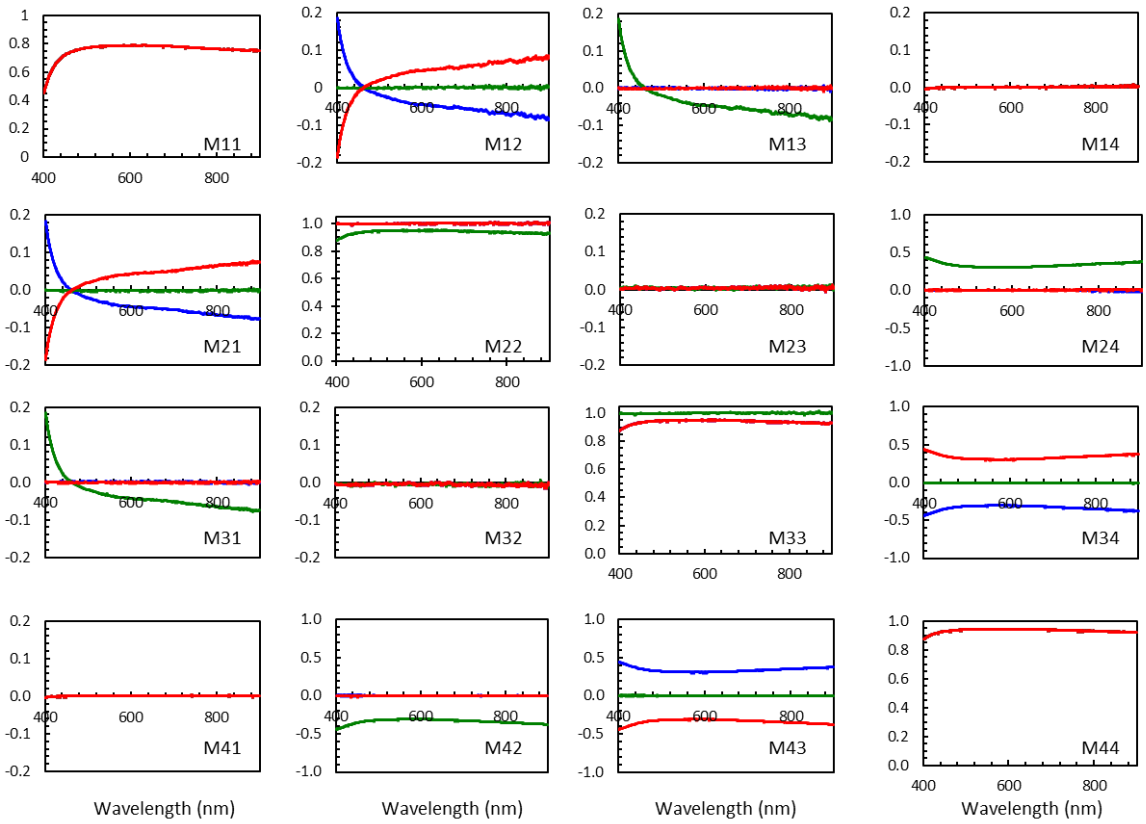

Figure 5.1 Optical spectra corresponding to the transmission Mueller matrix elements of Sample F at measurement angles (azimuth, measured from the lengthwise direction of the TCTF sample) of 0° (blue), 45° (green) and 90° (red). All spectra were acquired at normal incidence.

5.3.2 Diattenuation

To characterize the dependence of linear diattenuation on the AgNW loading amount, I plotted optical spectra of linear diattenuation for Samples B–F (Figure 5.2 (a); for simplicity, absolute values are shown). All spectra are similar in shape, with an isosbestic point at 460 nm and two distinct features: strong diattenuation below the isosbestic point and slow increase with wavelength above. As the AgNW loading amount increases (from Sample B to Sample F), diattenuation increases.

Figure 5.2 (b) shows measurements of the transmission axis azimuth for Sample F. Azimuth changes quickly from 0° (lengthwise direction) below the isosbestic point to 90°

(crosswise direction) above, within about 30 nm (450–480 nm). This confirms the results I established in previous chapters on TCTF anisotropies and axes orientation.

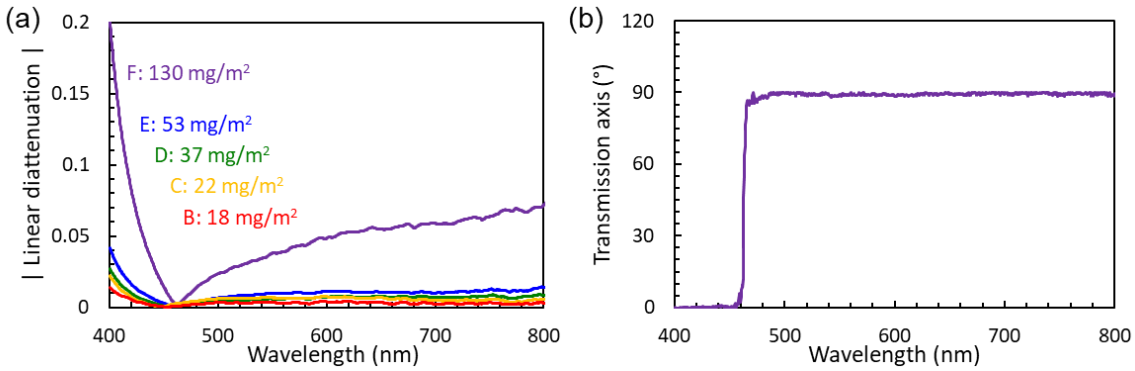

Figure 5.2 (a) Dependence of linear diattenuation on the AgNW loading amount. Optical spectra of Samples B (red), C (orange), D (green), E (blue) and F (purple) are shown. For convenience, absolute values of diattenuation are plotted. Isosbestic point is at 460 nm. (b) Azimuth of the transmission axis of Sample F, with the origin (0°) along the TCTF lengthwise direction.

5.3.3 Retardation

Linear retardance in a thin, planar medium is defined as the difference of refractive indices in orthogonal directions, multiplied by the medium thickness. Applying this to the TCTF, in-plane retardance can be expressed as:

$$\delta = (n_y - n_x) \times z_{eff}\,, \tag{5.14}$$

where z_{eff} represents the effective conductive layer thickness estimated in Chapter 4. Figure 5.3 (a) shows the effect of AgNW loading amounts on linear retardation spectra of Samples B–F, in the visible wavelength region. Like linear diattenuation, retardation increases with increasing AgNW loading amounts (from Sample B to Sample F) and the minimum value is found between 460–500 nm for all samples. In an anisotropic medium, the fast axis is the direction where refractive index is smallest. Figure 5.3 (b) shows the azimuth of the fast axis for Sample F. The fast axis clearly coincides with the TCTF lengthwise direction because the azimuth is nearly zero at all wavelengths. This result is

consistent with the relationship between the optical constants (Chapter 4, Figure 4.10) and explains the shape of the retardation spectra.

In Chapter 4, optical constants were measured by ellipsometry. From these, I derived retardation values using Equation (5.14). In Figure 5.4, I compare in-plane retardation of Sample A2 calculated by ellipsometry (Chapter 4) and by polarimetry (Figure 5.3 (a)). Although the polarimetric spectrum is somewhat flatter, both spectra have similar shape, with nearly equal values above 660 nm. This wavelength dependence reflects the impact of normal and anomalous dispersion on n_x and n_y.

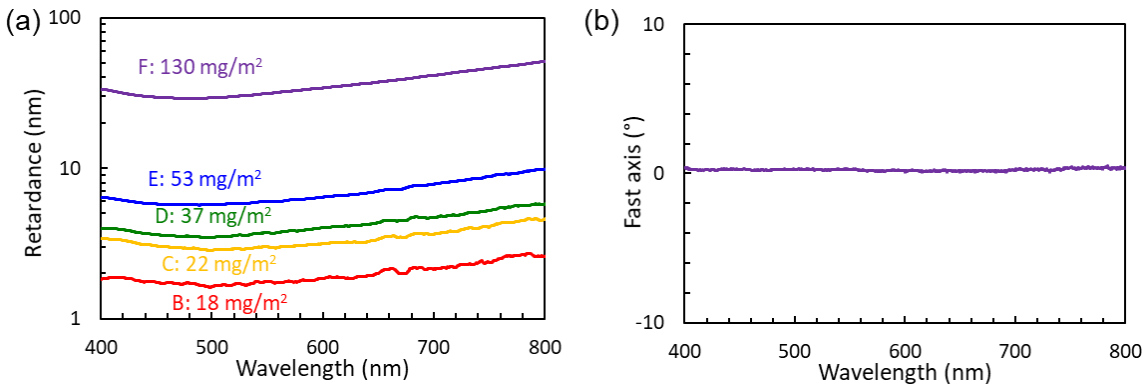

Figure 5.3 Same as Figure 5.2, but for (a) linear retardance and (b) azimuth of the fast axis.

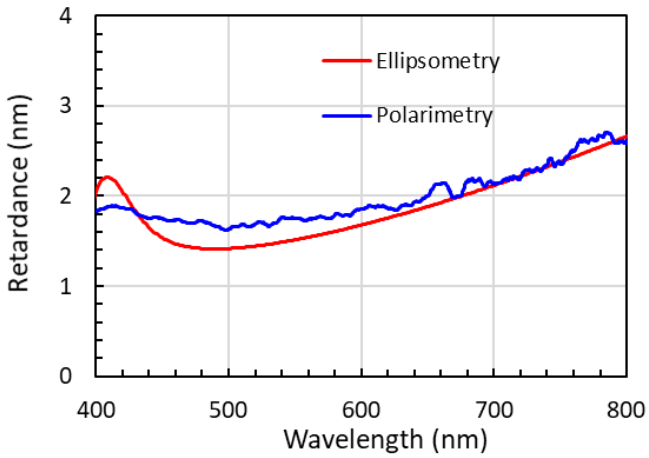

Figure 5.4 In-plane retardance spectra of Sample A2, calculated by ellipsometry (Chapter 4, red curve) and polarimetry (this chapter, blue curve).

5.3.4 Depolarization

In this section, I apply the photometric method that I developed (Section 5.2) to measure TCTF depolarization. The linear depolarization factor d_l was derived from this method using dual linear polarizers in the parallel and crossed configurations (Figure 2.7). In the first part of this study, I focused on Sample F to better illustrate the effects of AgNWs. I measured its transmittance at 450 nm and 700 nm. Configuration is explained in Section 2.4.4. Sample F was rotated in 5° steps from 0° (origin of azimuths, lengthwise direction of the sample) to 360°. The resulting polar curves (hereafter "trajectories") are shown in Figure 5.5 for the (a) parallel and (b) crossed configurations.

In the parallel configuration (Figure 5.5 (a)), trajectories at 450 nm and 700 nm show two orthogonal lines of symmetry. Transmittance at 450 nm is maximum in the parallel direction (0°–180°, lengthwise TCTF direction) and minimum in the perpendicular direction (90°–270°, crosswise). Conversely, the trajectory at 700 nm shows minimum transmittance in the parallel direction and maximum in the perpendicular direction. This confirms the extinction properties established earlier.

In the crossed configuration (Figure 5.5 (b)), transmittance trajectories at 450 nm and 700 nm are aligned. There are four polar lobes, thus four lines of symmetry. Transmittance minima are found in the parallel and perpendicular directions. This confirms that depolarization is the only effect observed along the lengthwise and crosswise directions of Sample F. Maxima occurring in intermediate directions (45°–225° and 135°–315°) likely include depolarization and additional retardation effects.

To quantify the degree of depolarization, I analyzed the transmittance of Sample F between two maxima (azimuths between −45° and +45° every 5°) in the crossed configuration. The full curve is symmetric (Figure 5.6 (a)), with maximum transmittance of about 1.35% at ±45° and minimum at 0° (~0.01%, Figure 5.6 (b)). The minimum value gives an estimate of the degree of depolarization (d_l) of Sample F.

Figure 5.7 shows transmission spectra of Sample F at azimuths of 0° and +45° in the crossed configuration. In the lengthwise direction (0°, Figure 5.7 (a)), transmittance is large at shorter wavelengths because of AgNW transverse mode extinction. Transmittance

decreases monotonically from a maximum of about 0.0085% at 420 nm to 0.004% at 780 nm. In the intermediate direction (+45°, Figure 5.7 (b)), transmittance values are larger than in the parallel direction by a factor of 100–200, but the spectrum shape is similar below ~500 nm. Transmittance shows a broad minimum (~1.2%) between 500–550 nm, then increases monotonically above ~550 nm. This increase could be due to contributions of additional retardation components.

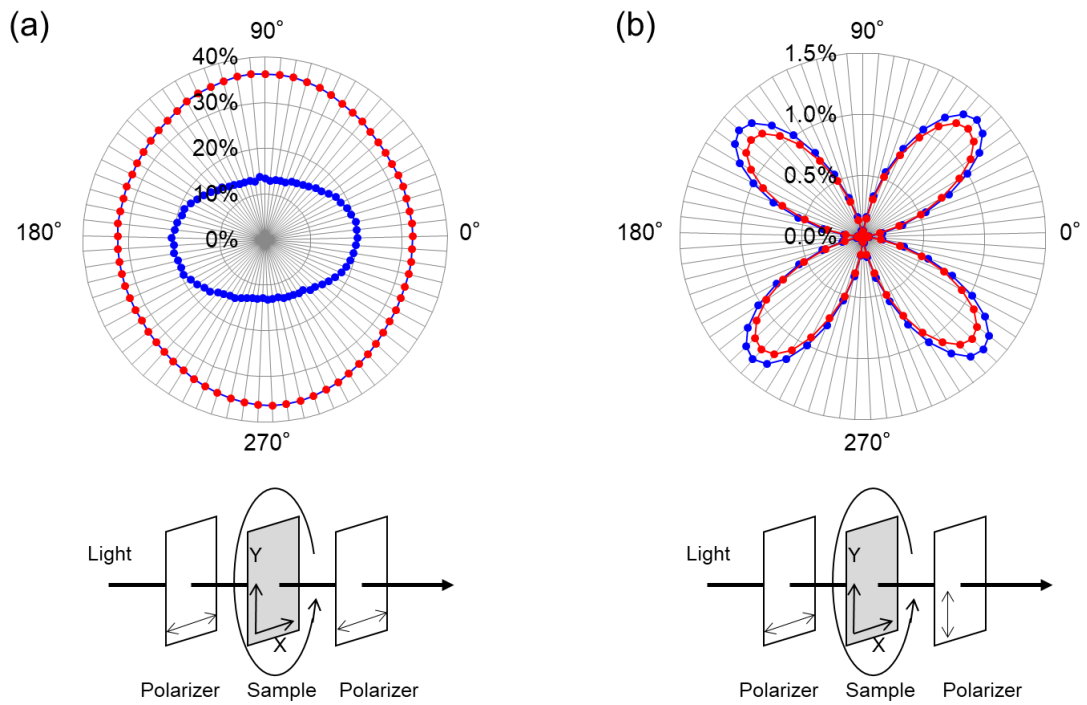

Figure 5.5 Transmittance of Sample F in the (a) parallel and (b) crossed configurations (Section 2.4.4), plotted in polar coordinates. Measurements are acquired at 450 nm (blue) and 700 nm (red) by rotating the sample in 5° steps from 0° to 360°. Origin of azimuths (0°) is the lengthwise sample direction. Schematic diagram of the measurement geometry is shown below; the parallel (x) and perpendicular (y) axes are aligned with the lengthwise and crosswise TCTF directions, respectively.

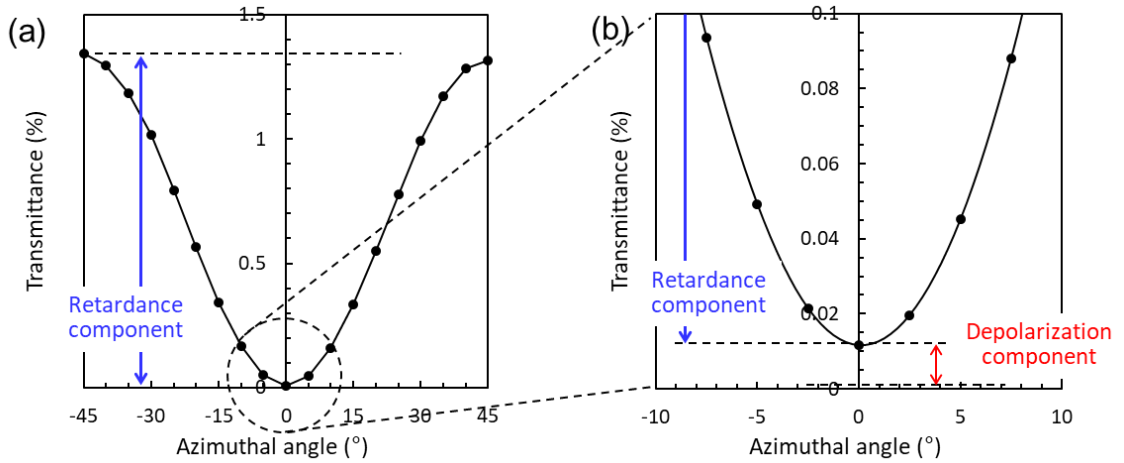

Figure 5.6 Azimuth dependence of Sample F transmittance at 450 nm in the crossed linear polarizers configuration. (a) Transmittance curve between two maxima (±45°) of the polar trajectory (blue curve, Figure 5.5 (b)). Sample F is rotated in 5° steps between −45° and +45°. Maximum transmittance is measured at ±45°. Minimum transmittance is measured along the lengthwise TCTF direction. (b) Enlarged scale, close to the transmission axis of the first polarizer (incident side, horizontal, azimuth 0°). Here, Sample F is rotated in 2.5° steps between −7.5° and +7.5°. Non-zero minimum transmittance corresponds to the depolarization component.

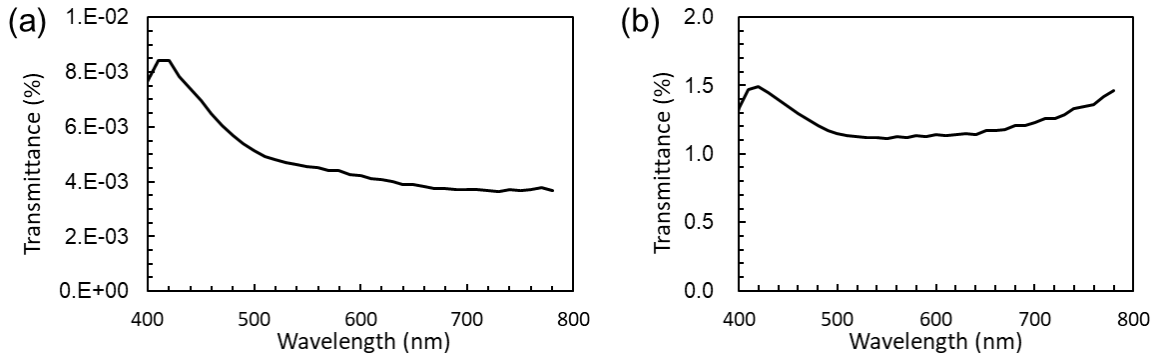

Figure 5.7 Optical transmission spectra of Sample F at azimuths of (a) 0° (corresponding to the blue curve in Figure 5.5 (b)) and (b) +45°, in the crossed configuration.

Finally, I investigated the effect of the AgNW loading amount and diameter on depolarization within the TCTFs, by comparing depolarization spectra of two sets of samples: Samples B–F, prepared with increasing loading amounts of the same AgNWs

(see Table 2.1 and Chapter 3), and Samples A2, B and G, which have similar sheet resistance but decreasing AgNW diameters (Chapter 2).

Figure 5.8 (a) shows the dependence of depolarization spectra on the AgNW loading amount (Samples B–F). As the loading amount decreases from Sample F to Sample B, depolarization decreases as well. This is expected, because low AgNW density should induce limited scattering of the incoming light, thus only a small depolarization effect.

Figure 5.8 (b) shows the dependence of depolarization spectra on the AgNW diameter (Samples A2, B and G). Samples A2, B and G have similar sheet resistance (about 50Ω/sq., see Table 2.1) and different diameters, but also slightly different loading amounts. As the AgNW diameter decreases from Sample A2 to Sample G, the degree of depolarization also decreases, despite a slight loading amount increase. Therefore, I conclude that small-diameter AgNWs could be effective in minimizing unwanted depolarization effects.

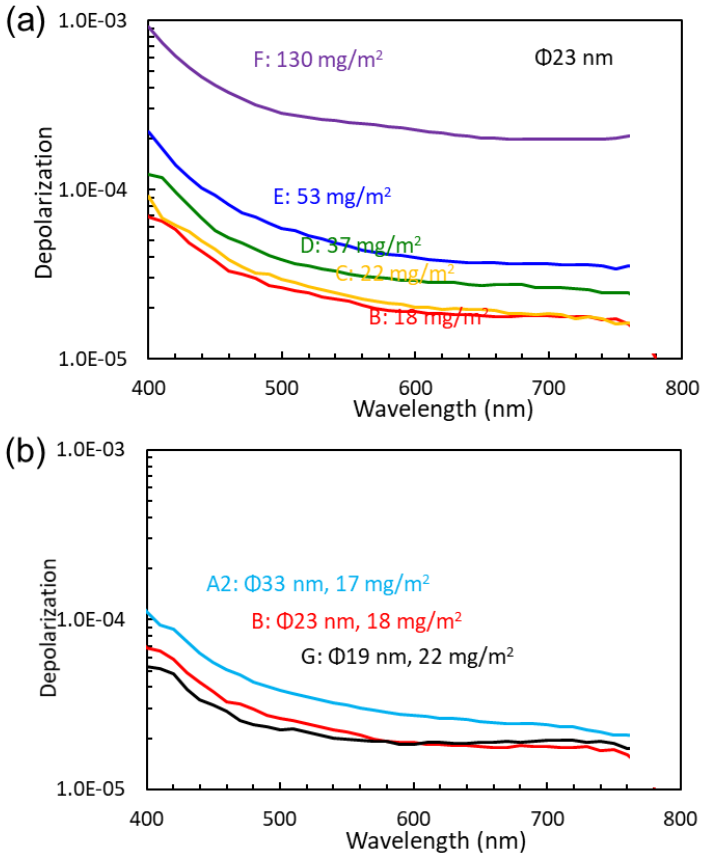

Figure 5.8 (a) Same representation as Figure 5.2 (a) but for depolarization spectra, to illustrate the effect of the loading amount on depolarization. AgNW diameter is indicated in the top right corner. (b) Depolarization spectra of Sample A2 (light blue), B (red) and G (black), which illustrate the effect of the AgNW diameter.

5.4 Light leakage of LCDs

Because TCEs are becoming increasingly thinner, LCD layout has recently shifted from a traditional out-cell structure to an in-cell architecture [1], where the TCE is placed between crossed linear polarizers. Unfortunately, in the in-cell architecture, retardation and depolarization within the TCE induce light leakage, a phenomenon in which linearly polarized light generated by the incident-side linear polarizer becomes elliptically or partially polarized by the TCE, causing unwanted light transmission through the outgoing-side orthogonal linear polarizer. Light leakage deteriorates the LCD contrast ratio. It is especially problematic when displaying dark screens. In this section, I investigate potential solutions to reduce light leakage in the TCTFs.

Figure 5.9 (a) shows the angular dependence of light leakage (seen as non-zero transmittance) on AgNW loading amounts (Samples B–F). Wavelength is set to 450 nm to better illustrate the phenomenon, because depolarization is larger at shorter wavelengths. Each sample is rotated close to the transmission axis of the first polarizer (azimuth steps of 2.5° between −7.5° and +7.5°). As the AgNW loading amount decreases (from Sample F to Sample B), light leakage also decreases at all azimuths. Furthermore, I confirm that light leakage is minimized if the TCTF principal axis (transmission axis) is aligned with the transmission axis of the incident-side polarizer, because minimum transmittance is observed along the lengthwise direction (azimuth 0°) of the samples.

Figure 5.9 (b) shows the angular dependence of light leakage on the AgNW diameter (Samples A2, B and G). As explained for Figure 5.8, depolarization decreases with decreasing diameter, thereby minimizing light leakage. Therefore, I conclude that light leakage can be reduced to 7×10^{-4} % by using AgNWs with diameters comparable or smaller than that of Sample B (23 nm, threshold shown by the dashed line in Figure 5.9 (b)) in TCTFs with sheet resistance of about 50 Ω/sq.. This is a significant improvement over conventional polarizer films used for LCDs, for which typical light leakage is 5×10^{-3} % [13].

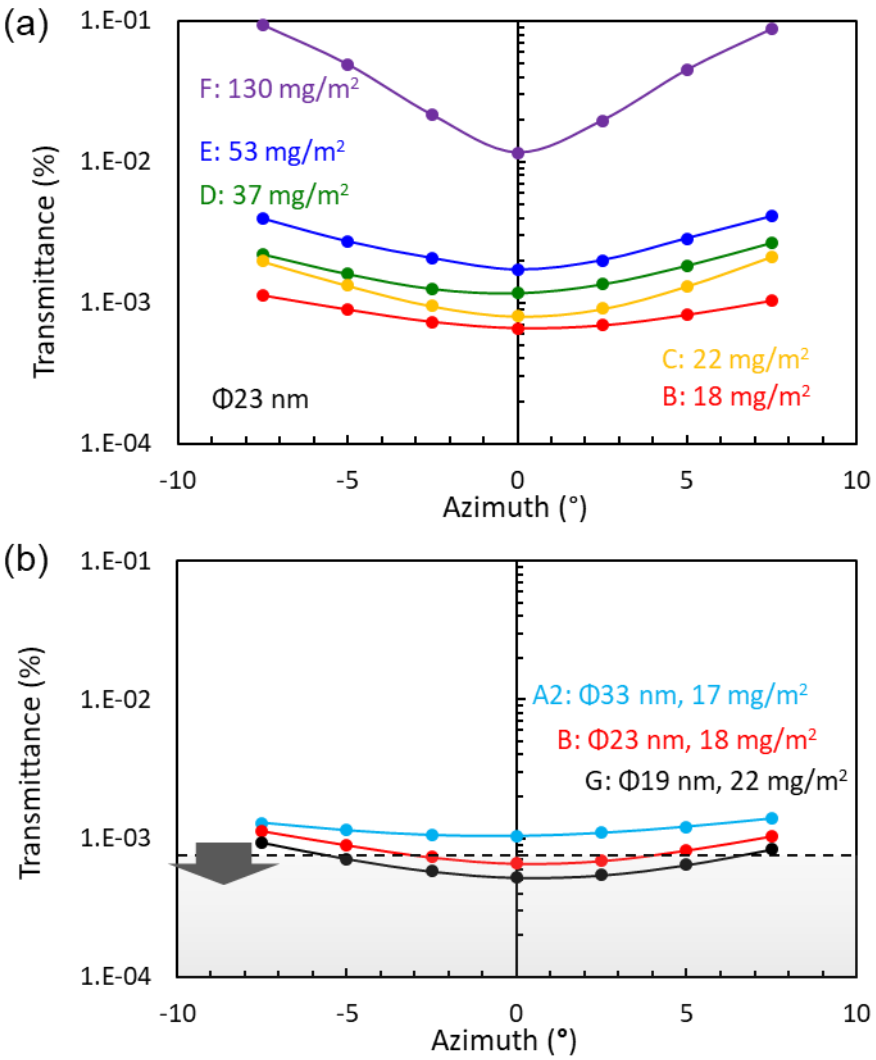

Figure 5.9 Angular dependence of light leakage on (a) AgNW loading amounts (Samples B–F, diameter indicated in the bottom left corner) and (b) AgNW diameters (Samples A2, B and G). Representation and measurement method for Panels (a) and (b) are the same as in Figure 5.6 (b) and color-coding is the same as in Figure 5.8. Shaded area in Panel (b) shows AgNW diameters optimally suited to minimize light leakage.

5.5 Conclusion for this chapter

In this chapter, I assessed the polarization properties of the TCTFs to minimize an undesirable effect known as LCD light leakage. I quantified diattenuation, retardation and depolarization of the TCTFs. Since the degree of depolarization is consistently too small

for standard polar decomposition method, I developed an original photometric method for this analysis. I found that the amplitude of diattenuation and retardation is directly proportional to the AgNW loading amounts, whereas depolarization is not only proportional to the loading amounts, but also to the AgNW diameter.

From these results and the confirmation of the TCTF axes orientation, I was able to determine two practical ways of reducing light leakage to a level acceptable for industrial applications, notably for TCEs. The first is to minimize retardation by aligning the TCTF principal axis (transmission axis) with the transmission axis of the incident-side polarizer, in the dual-linear-polarizer crossed configuration used for in-cell architectures. The second is to reduce depolarization by using smaller-diameter AgNWs. For TCTFs with a sheet resistance of about 50Ω /sq., I established that the AgNW diameter should be limited to 23 nm or less, which allowed me to calculate a light leakage of 7×10^{-4} % or less. This is an order of magnitude better than current conventional values and would allow for operational use of the TCTFs.

5.6 References for Chapter 5

[1] Geoff Walker, Mark Fihn, "LCD In-Cell Touch," Inf. Disp. **26**(3), 8-14 (2010).

[2] Ranbir Singh, K.N. Narayanan Unni, Ankur Solanki, Deepak, "Improving the Contrast Ratio of OLED Displays: An Analysis of Various Techniques," Opt. Mater., **34**(4), 716-723 (2012).

[3] Jalpa Soni, Harsh Purwar, Nirmalya Ghosh, "Quantitative polarimetry of plasmon resonant spheroidal metal nanoparticles: A Mueller matrix decomposition study," Opt Commun. **285**(6), 1599-1607 (2012).

[4] Sayantan Ghosh, Jalpa Soni, Sudipta K. Bera, Ayan Banerjee, Nirmalya Ghosh, "Mueller Matrix Polarimetry of Plasmon Resonant Silver Nano-Rods: Biomedical Prospects," Proc. SPIE. **8699**, 869902 (2013).

[5] Shubham Chandel, Jalpa Soni, Subir kumar Ray, Anwesh Das, Anirudha Ghosh, Satyabrata Raj, Nirmalya Ghosh, "Complete Polarization Characterization of Single Plasmonic Nanoparticle Enabled by a Novel Dark-field Mueller Matrix Spectroscopy System," Sci. Rep. **6**, 26466 (2016).

[6] Nikolai G. Khlebtsov, Lyubov A. Trachuk, Andrei G. Melnikov, "Plasmon Resonances of Silver and Gold Nanorods," Proceedings of the SPIE. **5475**, 1-11 (2004).

[7] Nikolay G. Khlebtsov, "Anisotropic Properties of Plasmonic Nanoparticles:

Depolarized Light Scattering, Dichroism, and Birefringence," J. Nanophotonics **4**(1), 041587 (2010).

[8] Garo Khanarian, Jaebum Joo, X.-Q. Liu, Peter Eastman, Daniel Werner, Kathleen M. O'connell, Peter Trefonas, "The Optical and Electrical Properties of Silver Nanowire Mesh Films," J. Appl. Phys. **114**(2), 024302 (2013).

[9] Colin Preston, Yunlu Xu, Xiaogang Han, Jeremy N. Munday, Liangbing Hu, "Optical Haze of Transparent and Conductive Silver Nanowire Films," Nano Res. **6**(7), 461-468 (2013).

[10] Teppei Araki, Jinting Jiu, Masaya Nogi, Hirotaka Koga, Shijo Nagao, Tohru Sugahara, Katsuaki Suganuma, "Low Haze Transparent Electrodes and Highly Conducting Air Dried Films with Ultra-Long Silver Nanowires Synthesized by One-Step Polyol Method," Nano Res. **7**(2), 236–245 (2014).

[11] Maria Losurdo, Kurt Hingerl, "Ellipsometry at the Nanoscale", Springer, ISBN 978-3-642-33955-4

[12] Shih-Yau Lu, Russell A. Chipman, "Interpretation of Mueller Matrices Based on Polar Decomposition," J. Opt. Soc. Am. A. 13(5), 1106-1113 (1996).

[13] Yuka Utsumi, Ikuo Hiyama, Yasushi Tomioka, Katsumi Kondo,Shigeru Matsuyama, "Analysis of light leakage caused by color filter between crossed polarizers," Jpn. J. Appl. Phys. 46(3A) 1047-1050 (2007).

Chapter 6

Absorption and scattering by AgNWs

6.1 Introduction

Aside from light leakage (Chapter 5), the phenomenon known as “pattern visibility” is another important issue affecting TCEs in touch-screen devices. The human eye can perceive optical differences between regions with and without AgNWs. This characterizes pattern visibility. In ITO-based TCEs, pattern visibility is generally solved by inserting a matched refractive index layer between the high refractive index ITO and the substrate to minimize specular reflectance differences between regions with and without ITO [1,2].

In AgNW-based TCFs, pattern visibility is caused by AgNW density inhomogeneities in the polymer [3,4]. AgNWs cause light scattering of the incident light, thus the diffuse component dominates the transmission and reflection spectrum. Pattern visibility in AgNW-based TCFs takes two forms: forward scattering (or forward haze), which obscures the image projected from the display, and backward scattering (or backward haze), generally more pronounced, in which diffuse reflection on the AgNWs creates a pale blue hue over the black background (when display is turned off). Forward haze (diffuse transmission/total transmission) has been studied extensively [5–10] and was found to be proportional to the AgNW diameter. Therefore, decreasing the AgNW diameter is an effective way of reducing forward haze [5,6,9,10]. Furthermore, length and

loading amount of AgNWs were shown to affect backward haze (diffuse reflection/total reflection) [11,12].

Absorption and scattering have been extensively studied for metal nanowires but almost exclusively through model simulations of infinite length single cylinders [13,14]. Few real-case analyses for densely packed AgNW networks are available. In the previous chapters, I showed that polarized extinction (which includes absorption and scattering) within the TCTFs depends on AgNW orientation. In this chapter, I firstly derive intrinsic TCTF optical properties—absorption and scattering—from transmission and reflection spectra measured using an integrating sphere. Then, I establish a method to quantify pattern visibility from diffuse reflection spectra, by calculating color differences ΔE_{00} (CIEDE2000 [15,16]) in the color space formalism (CIELab a*, b*, L* [17]). Until now, ufortunately, pattern visibility has only been evaluated visually but has not been quantified. By quantifying the dependence of the color difference on AgNW diameter and loading amounts, I explore ways to reduce pattern visibility.

6.2 Optical measurements

6.2.1 Absorption and scattering measurements

To evaluate absorption and scattering within the TCTF samples, total and diffuse transmission and reflection spectra were acquired from the near-UV to the NIR using an integrating sphere mounted on a spectrophotometer. Technical specifications and experimental configurations are given in Chapter 2, Section 2.4.5.

6.2.2 Color difference calculations

To quantitatively evaluate pattern visibility, I applied the CIEDE2000 formula [15,16] to the diffuse reflection spectra to calculate the color difference ΔE_{00} (relative to standard illuminant D65) between regions with and without AgNWs. ΔE_{00} expresses colors using three CIE components named a*, b* and L*. a* and b * are color indices; a* varies from

green (−) to red (+) and b * from blue (−) to yellow (+). L* represents the luminance from black (0) to white (100) [17]. ΔE_{00} is considerably more sophisticated than its predecessor ΔE^*_{ab} (CIELab formula), to improve performance for blue and gray colors [16]. Detailed formula for color difference calculation is given in Appendix 2.

6.3 Transmission and reflection spectra

With the experimental setup described in Section 2.4.5, I measured polarized total and diffuse transmission and reflection spectra, both for the polymer coating alone and for Sample E (Table 2.1), to derive absorption, scattering and extinction for the TCTFs. Two orthogonal polarizations were investigated.

Figure 6.1 (a)–(b) shows the diffuse transmission and reflection spectra of the polymer coating (without AgNWs). Both are nearly zero at all wavelengths, with no difference between the orthogonal polarizations. Figure 6.1 (c)–(d) shows similar spectra for specular transmission and reflection. Above 400 nm, specular transmittance is nearly constant (~0.92), whereas the reflectance spectrum shows a slight negative slope. Interference fringes (oscillations) due to the thickness of the polymer can also be seen. Below 400 nm, both specular spectra show a sharp drop caused by the UV-absorbing chromophores incorporated in the polymer (already mentioned in Chapter 4). Furthermore, there is no visible dependence of either transmittance or reflectance on the incident polarization: blue and red spectra in Figure 6.1 are nearly superimposed. Thus, absorption and reflection of the polymer coating alone do not show any diffuse components and do not depend on the incident polarization.

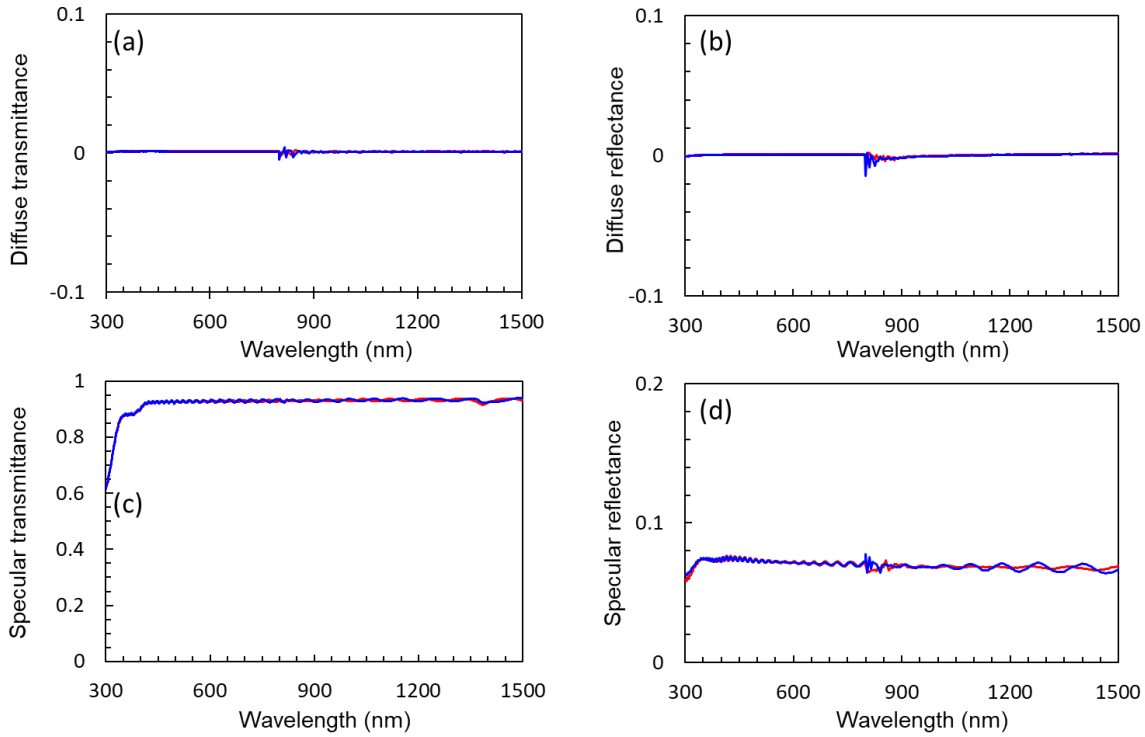

Figure 6.1 Diffuse (top row) and specular (bottom row) transmission (a, c) and reflection (b, d) spectra of the polymer coating, for incident light polarization oriented along the lengthwise (blue) and crosswise (red) TCTF directions. Oscillations on the specular spectra are interference fringes caused by the polymer layer thickness. Noisy features near 800 nm are due to the changeover from the PMT detector used in the near-UV and visible region to the PbS detector used in the NIR region (as described in Chapter 2).

Figure 6.2 shows similar spectra for Sample E. Sample E was selected because it has a large loading amount of AgNWs, hence their scattering properties are more pronounced. Unlike the polymer, TCTF anisotropy induces spectral features depending on the incident polarization angle. The diffuse transmission (Figure 6.2 (a)) and reflection (Figure 6.2 (b)) spectra both show a marked peak around 383 nm, with a shoulder at 360 nm. This was already shown on the TCTF extinction spectra of Figure 3.5 and corresponds to the AgNW transverse mode. The slight upward slope at visible and NIR wavelengths is caused by the longitudinal mode. Diffuse transmittance and reflectance are larger around the transverse mode for the perpendicular polarization (red curve above blue near 400 nm) and larger in the longitudinal mode for parallel incident polarization (blue curve above red above ~500 nm). Finally, specular transmission (Figure 6.2 (c)) and reflection

(Figure 6.2 (d)) spectra show opposite behavior: a local minimum of specular transmission is found in the near-UV, smaller for the perpendicular polarization (red curve below blue near 400 nm), while a downward slope is observed above 500 nm, with smaller values in the longitudinal mode for parallel polarization (blue curve below red above ~500 nm). Specular reflection shows similar features but with smaller amplitude. Oscillations caused by interferences in the thick polymer layer are also visible.

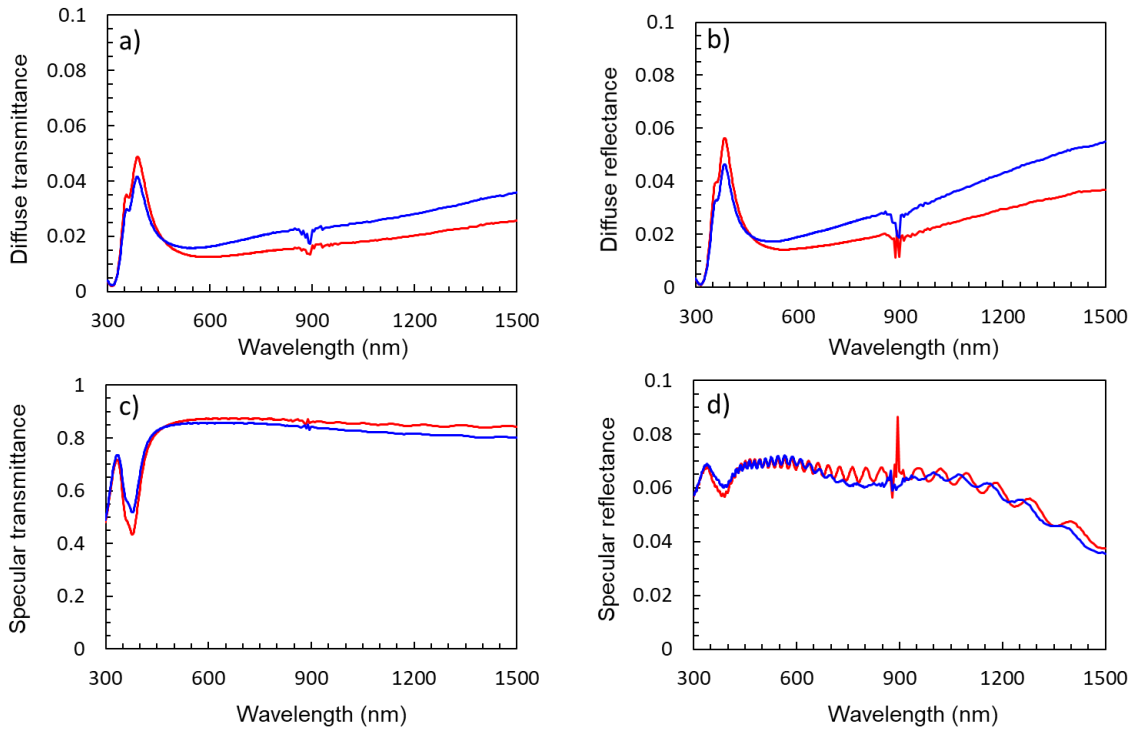

Figure 6.2 Same as Figure 6.1, but for Sample E.

6.4 Absorption and scattering spectra

6.4.1 TCTF samples

Using the transmittance and reflectance spectra, I calculate absorption, scattering and extinction from Equations (2.7)–(2.9). Absorption and scattering of Sample E are shown in Figure 6.3. Absorption (Figure 6.3 (a)) and scattering (Figure 6.3 (b)) spectra show a peak around the transverse mode (near-UV) and a small positive slope in the longitudinal

mode (Vis to NIR). Near the transverse mode, absorption and scattering are larger when incident polarization is oriented along the crosswise TCTF direction (red curve above blue below ~500 nm) and smaller in the longitudinal mode when polarization is parallel to the lengthwise direction (blue curve above red above ~500 nm).

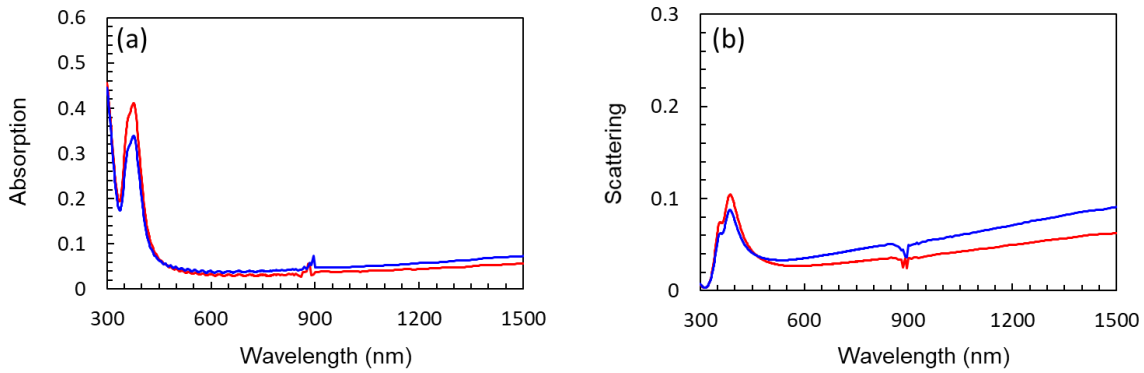

Figure 6.3 Same as Figure 6.2 (a)–(b) for (a) absorption and (b) scattering of Sample E.

Finally, I investigated the dependence of TCTF absorption, scattering and extinction on AgNW loading amount and diameter, respectively, by comparing Samples B–E, which contain the same AgNWs in increasing loading amounts, and Samples A2, B and G, which have similar sheet resistance but decreasing AgNW diameters (Table 2.1). I restricted the spectral range to near-UV and visible wavelengths (300–800 nm) to emphasize near-UV absorption and scattering in the visible region.

Figure 6.4 shows the effect of AgNW loading amounts for unpolarized incident light. As the loading amount decreases (from Sample E to Sample B), absorption (Figure 6.4 (a)), scattering (Figure 6.4 (b)) and extinction (Figure 6.4 (c)) consistently decrease at all wavelengths. I also calculated the ratio between the absorption and extinction spectra (Figure 6.4 (d)). In the near-UV, it is large (0.7 or larger below 400 nm) and nearly equal for all samples. At visible wavelengths, it decreases quickly and stabilizes within 0.4–0.6 for all samples above about 500 nm. This means that TCTFs behave mostly as absorbers in the near-UV region, whereas absorption and scattering contribute equally to extinction in the visible region. Furthermore, the fact that the ratio does not depend on the loading

amount (despite noticeably larger interference fringes for smaller loading amounts, Figure 6.4 (d)) confirms that AgNWs are arranged approximately as a 2D network. Otherwise, multiple scattering within the volume of the samples would cause scattering values to increase proportionally to the AgNW loading amount.

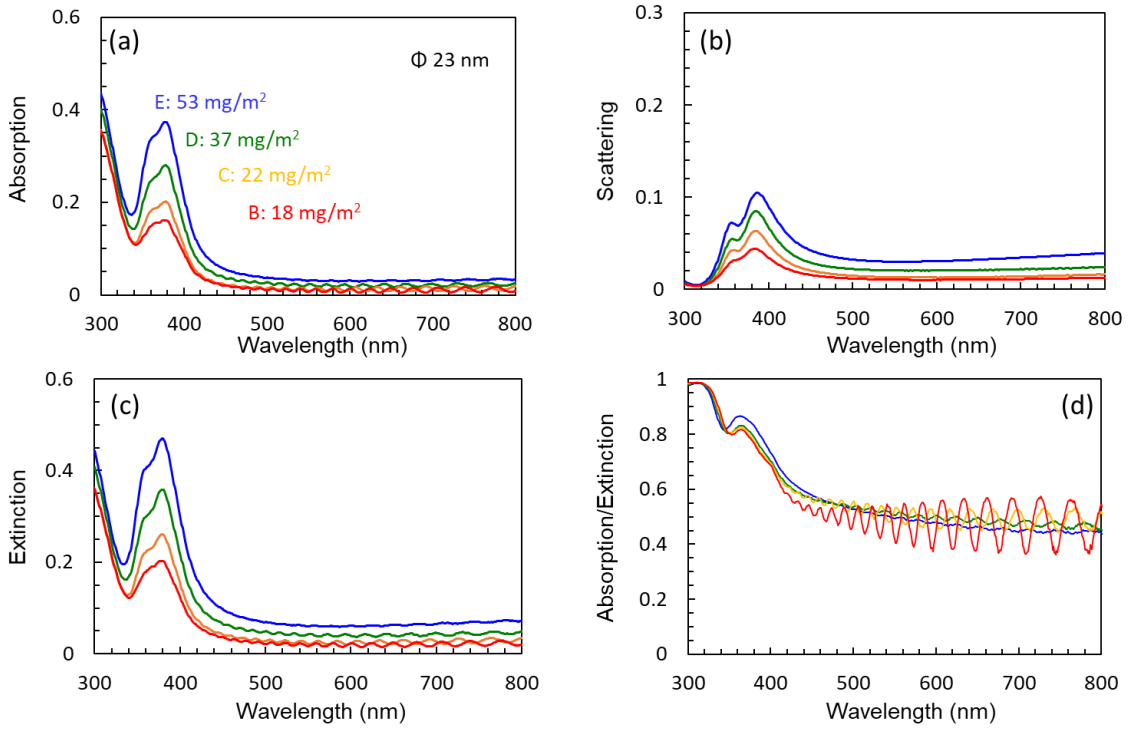

Figure 6.4 Dependence of (a) absorption, (b) scattering and (c) extinction of Samples B–E on AgNW loading amounts, in the near-UV and visible spectral regions, for unpolarized incident light. The ratio of absorption to extinction spectra is shown in Panel (d).

Figure 6.5 shows the dependence of absorption and scattering on the AgNW diameter for unpolarized incident light. Resistivity of AgNWs is inversely proportional to their diameter because of surface scattering by conduction electrons [18]. Therefore, achieving similar sheet resistance with smaller-diameter AgNWs requires larger amounts. As the diameter decreases (from Sample A2 to Sample G), absorption around the transverse mode increases (Figure 6.5 (a)). On the contrary, smaller diameters yield lower scattering independently of the loading amount (Figure 6.5 (b)). Furthermore, the transverse mode scattering peak shifts to shorter wavelengths when the AgNW diameter decreases.

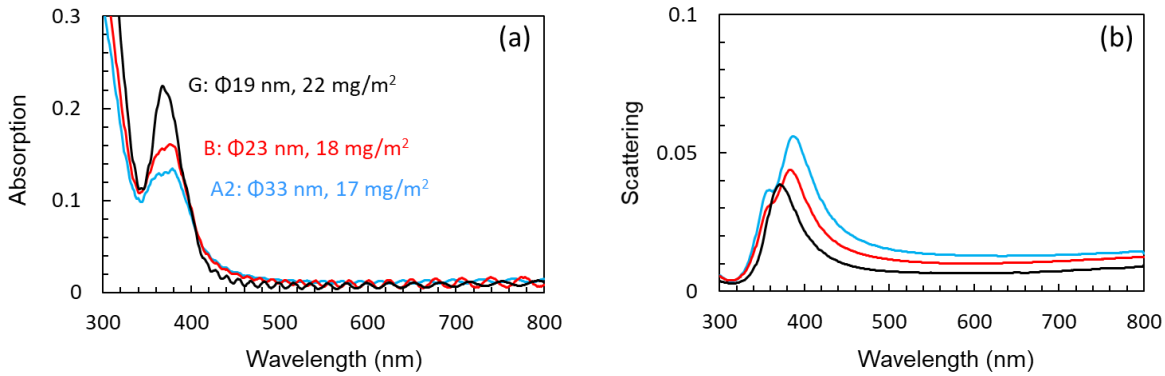

Figure 6.5 Same as Figure 6.4 (a)–(b) but for Samples A2, B and G, with the same color-coding as in Figure 5.9 (b).

6.4.2 Mie simulations – singular infinite AgNW

To confirm the experimental results, I performed model simulations of a single, infinite length AgNW with a simulator based on Mie theory [19]. This simulator applies Mie scattering theory to calculate total absorption and scattering efficiencies (Figure 6.6 (a)–(b)). Total absorption efficiency is the ratio of the absorption cross-section to the geometric cross-section. Total scattering efficiency is calculated the same way but for scattering. To determine these cross-sections for different AgNW diameters, I introduced the "effective cross-section ratio", defined as the geometric cross-section ratio multiplied by the loading amount and divided by the volume. In this expression, each quantity (geometric cross-section, loading amount and volume) is normalized to Sample A2. Effective absorption and scattering cross-sections are then calculated by multiplying the corresponding efficiency by the effective cross-section ratio.

Figure 6.6 (c)–(d) shows the results for an ensemble of AgNWs of Samples A2, B and G. As the AgNW diameter decreases (from Sample A2 to Sample G), the transverse mode effective absorption cross-section increases while the effective scattering cross-section decreases at all wavelengths. This is very similar to the measured results (Figure 6.5). The wavelength shift of the scattering peak is also well reproduced. In summary, these simulations confirmed the 2D nature of the AgNW network.

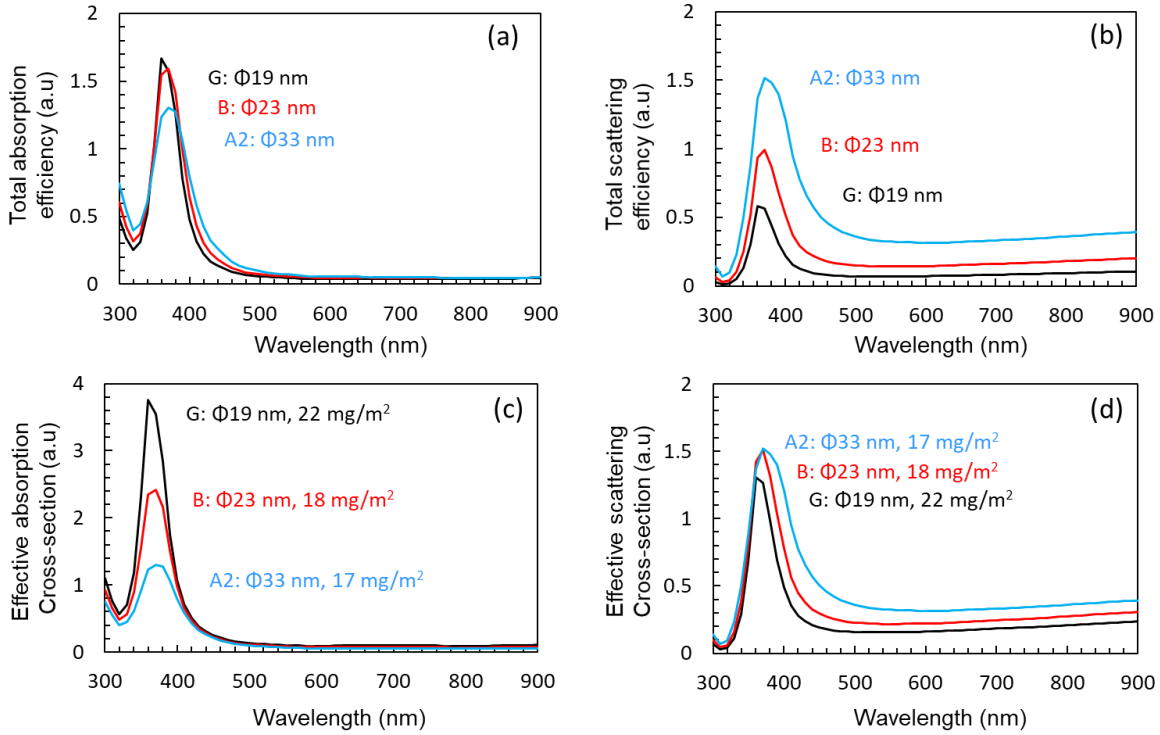

Figure 6.6 Model simulations of efficiencies (top row) by a single, infinite length AgNW and effective cross-sections (bottom row) for an ensemble of AgNWs for absorption (a, c) and scattering (b, d). Nanowire diameters are set to those of Samples A2, B and G (Table 2.1). Color-coding is the same as in Figure 6.5. Efficiencies and cross-sections are expressed in arbitrary units.

6.5 Color difference

Until now, pattern visibility in AgNW-based TCFs has not been objectively quantified, but only evaluated visually. Therefore, existing results depend directly on the observer. To overcome the potential subjective bias, I decided to establish an experimental method to quantify pattern visibility. For this purpose, I applied the color difference formula ΔE_{00} [15,16] to diffuse reflection spectra of the TCTFs, to compare regions with and without AgNWs. Equations defining ΔE_{00} are detailed in Appendix 2.

Figure 6.7 shows the effect of AgNW loading amounts (Samples B–E, Figure 6.7 (a)) and diameter (Samples A2, B, G, Figure 6.7 (b)), respectively, on TCTF diffuse reflection

spectra. Diffuse reflectance is large and decreases with increasing wavelengths below about 500 nm, shows a broad minimum between 500–600 nm, then gradually increases at longer wavelengths. Diffuse reflectance decreases with both the loading amount and diameter of AgNWs. However, the way colors are perceived by the human eye cannot be easily determined from the spectra. Therefore, I used the diffuse reflection spectra to calculate color-space parameters and color difference for the TCTFs.

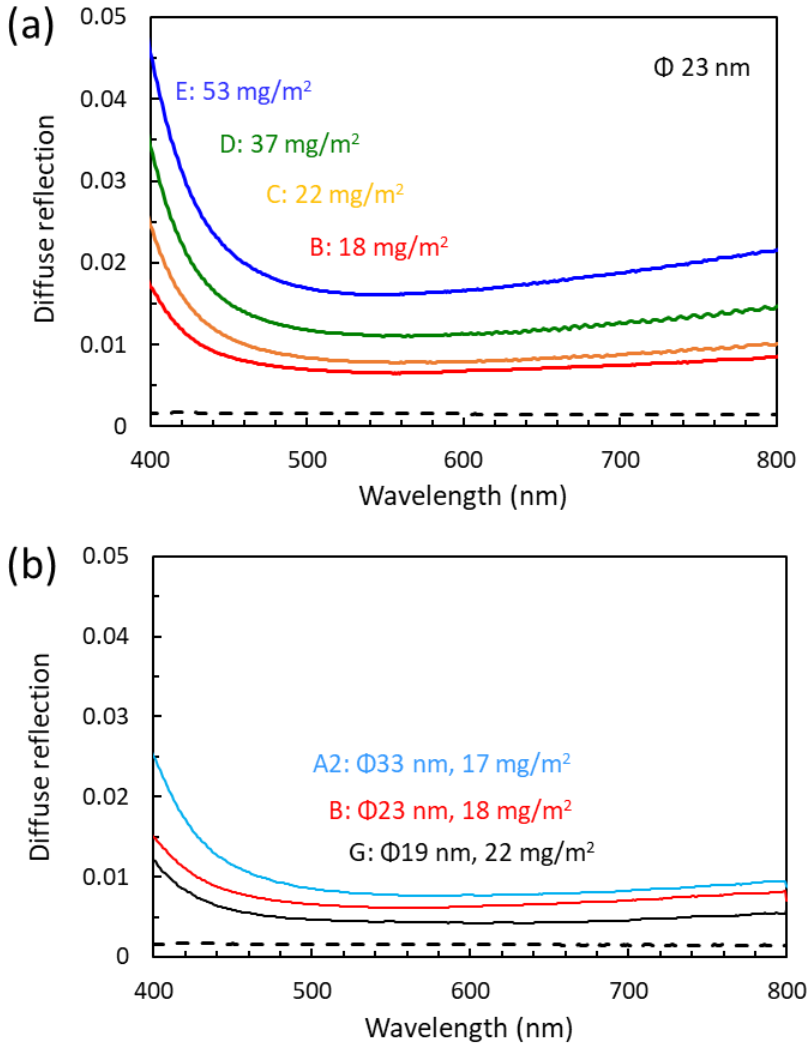

Figure 6.7 Same representation as in Figure 5.9, but for diffuse reflection spectra as a function of (a) the AgNW loading amount (Samples B–E) and (b) the AgNW diameter (Samples A2, B and G). The polymer spectrum (dashed black) is also shown.

Figure 6.8 shows the sample localization in the CIELab color space. The color parameters (a*, b* and L*) and color difference ΔE_{00} are plotted as a function of the AgNW loading amount. Samples are each represented by a dot, color-coded as in Figure 6.7. This allowed me to quickly visualize the effect of the AgNW loading amount (and of the diameter) on the color parameters.

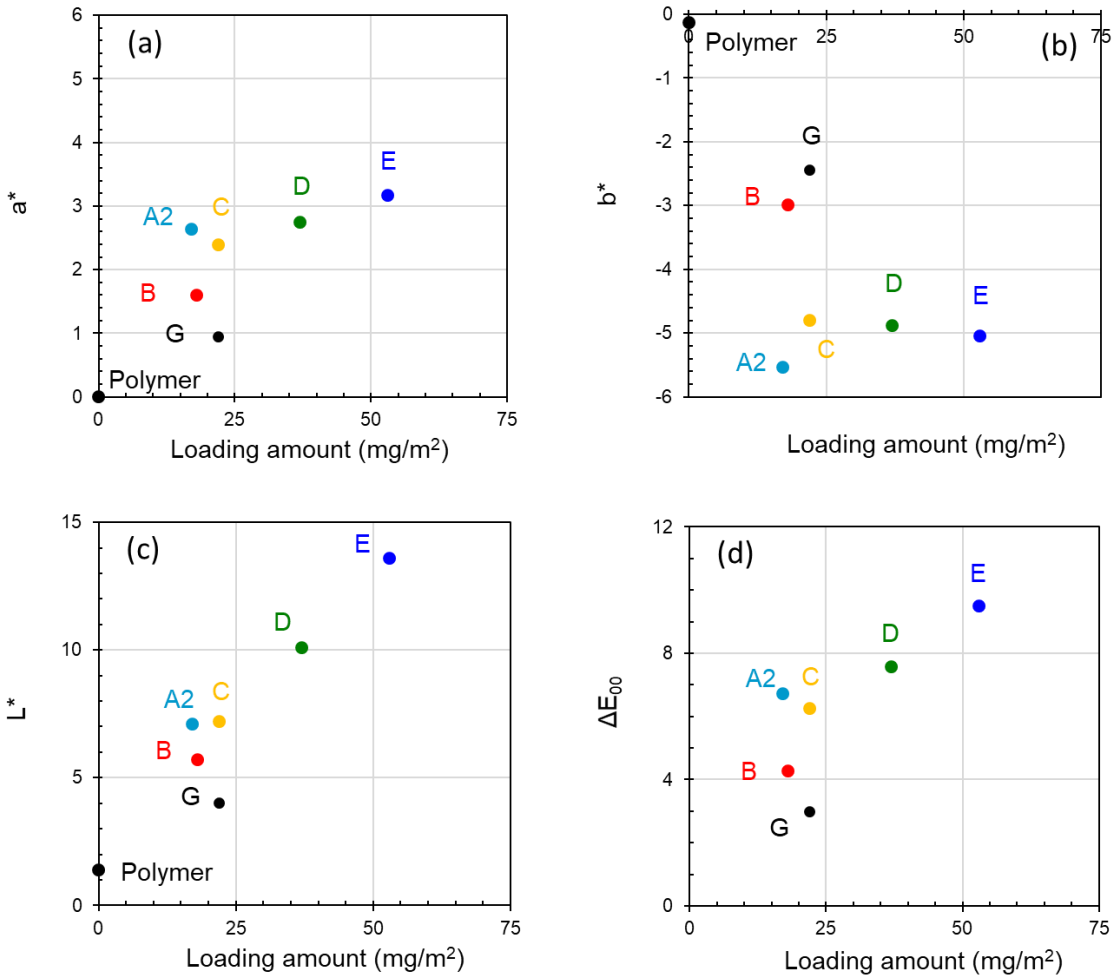

Figure 6.8 Localization of the TCTF samples in the CIELab color space. Color parameters (a) a*, (b) b*, (c) L* and (d) color difference ΔE_{00} are plotted as a function of the AgNW loading amount. Values for the polymer are also indicated. Color-coding for the samples is the same as in Figure 6.7.

Parameters a* and b* are shown in Figure 6.8 (a) and (b), respectively. They behave consistently for all samples: a* is small and positive (red hues) with values within 0.9–3.2, whereas b* is negative (blue hues) with larger values, between −5.6 and −2.4. This means that the human eye consistently perceives our TCTFs with a pale, light blue hue. As the AgNW loading amount (from Sample E to Sample B) and diameter (from Sample A2 to Sample G) decrease, a* and b* both tend toward zero (neutral hue).

The luminance parameter L* (Figure 6.8 (c)) decreases monotonically when the AgNW loading amount decreases (from Sample E to Sample B). L* also decreases (from 7.1 to 4.0) with the AgNW diameter (from Sample A2 to Sample G). This result is expected, because smaller AgNW diameters induce lower scattering.

Finally, the color difference ΔE_{00} is shown in Figure 6.8 (d). The behavior of ΔE_{00} is similar to that of a* and L*. Since limiting pattern visibility implies minimizing ΔE_{00}, I concluded that Sample G, with the smallest value of ΔE_{00}, is best suited for this purpose. Results of the calculations for L*, a*, b* and ΔE_{00} are summarized in Table 6.1.

Table 6.1 CIELab color space parameters L*, a*, and b* and color difference ΔE_{00}, for the polymer coating and for Samples A2, B–E and G.

Sample designation	Average diameter (nm)	AgNW loading (mg/m^2)	a*	b*	L*	ΔE_{00}
Polymer	—	—	0.00	−0.13	1.4	—
A2	33	17	2.63	−5.53	7.1	6.72
B	23	18	1.60	−2.99	5.7	4.28
C		22	2.39	−4.80	7.2	6.24
D		37	2.74	−4.88	10.1	7.58
E		53	3.17	−5.05	13.6	9.50
G	19	22	0.94	−2.45	4.0	2.97

6.6 Conclusion for this chapter

In this chapter, I devised a method to quantify pattern visibility, a difference of optical properties that occurs when patterning electrodes with AgNW-based TCFs and investigated ways to reduce this phenomenon. For this purpose, I analyzed TCTF diffuse reflection spectra, converted them into color space with the CIE formalism and derived the color difference ΔE_{00} (CIEDE2000) between regions with and without AgNWs. I showed that the composite film with the smallest AgNW diameter has the smallest color difference, which directly leads to minimizing pattern visibility. Additionally, among TCTFs with similar sheet resistance, those with smaller AgNW diameter show stronger absorption in the near-UV and limited scattering at all wavelengths. This could also allow me to reduce pattern visibility.

6.7 References for Chapter 6

[1] Chang Seok Oh, Sang Mun Lee, Eun Hye Kim, Eun-Woo Lee, Lee Soon Park, “Electro-Optical Properties of Index Matched ITO-PET Film for Touch Panel Application,” Mol. Cryst. Liq. Cryst. 568(1), 32-37 (2012).

[2] Chan-Hwa Hong, Jae-Heon Shin, Byeong-Kwon Ju, Kyung-Hyun Kim, Nae-Man Park, Bo-Sul Kim, Woo-Seok Cheong, “Index-Matched Indium Tin Oxide Electrodes for Capacitive Touch Screen Panel Applications,” J. Nanosci. Nanotechnol. 13(11), 7756-7759 (2013).

[3] Eun-Hyoung Cho, Jinyoung Hwang, Jaekwan Kim, Jooho Lee, Chan Kwak, Chang Seung Lee, “Low-Visibility Patterning of Transparent Conductive Silver-Nanowire Films,” Opt. Express 23(20), 26095-26103 (2015).

[4] Kwonwoo Shin, Ji Sun Park, Jong Hun Han, Yunsu Choi, Dae Sung Chung, Se Hyun Kim, “Patterned Transparent Electrode with a Continuous Distribution of Silver Nanowires Produced by an Etching-Free Patterning Method,” Sci. Rep. 7, 40087 (2017).

[5] Colin Preston, Yunlu Xu, Xiaogang Han, Jeremy N. Munday, Liangbing Hu, “Optical Haze of Transparent and Conductive Silver Nanowire Films,” Nano Res. 6(7), 461-468 (2013).

[6] Garo Khanarian, Jaebum Joo, X.-Q. Liu, Peter Eastman, Daniel Werner, Kathleen M. O'connell, Peter Trefonas, “The Optical and Electrical Properties of Silver Nanowire Mesh Films,” J. Appl. Phys. 114, 024302 (2013).

[7] A. B. M Hasan Talukder, Md. Omar Faruk, Shahida Rafique, “Analysis of Silver and Gold Nanowires to Determine the Effect of Diameter Change on Cross-Sections and Local Electric Field Intensity,” International Journal of Electronics & Informatics 3(1), 1-10 (2014).

[8] Xiaoming Yu, Xuan Yu, Jianjun Zhang, Dekun Zhang, Jian Ni, Hongkun Cai, Dexian Zhang, Ying Zhao, “Investigation of Light Transmission and Scattering Properties in Silver Nanowire Mesh Transparent Electrodes,” Mater. Lett. 145, 219-223 (2015).

[9] Mini Mol Menamparambath, Kihyuk Yang, Hyeong Hoon Kim, Oh Seung Bae, Mun Seok Jeong, Jae-Young Choi, Seunghyun Baik, “Reduced Haze of Transparent Conductive Films by Smaller Diameter Silver Nanowires,” Nanotechnology, 27(46), 465706 (2016).

[10] M. Marus, A. Hubarevich, W. J. Fan, H. Wang, A. Smirnov, K. Wang, H. Huang, X. W. Sun, “Optical Haze of Randomly Arranged Silver Nanowire Transparent Conductive Films with Wide Range of Nanowire Diameters,” AIP Adv. 8(3), 035201 (2018).

[11] Xiaoming Yu, Xuan Yu, Jianjun Zhang, Liqiao Chen, Yunqian Long, Dekun Zhang, “Optical Properties of Conductive Silver-Nanowire Films with Different Nanowire Lengths,” Nano Res. 10(11), 3706-3714 (2017).

[12] Xiaoming Yu, Xuan Yu, Liqiao Chen, Jianjun Zhang, Yunqian Long, Leng Zhe, Jinfei Hu, Huiqiu Zhang, Yaning Wang, “Investigation the Scattering Properties of Silver Nanowires with Different Densities,” Opt. Mater. 84, 490-497 (2018).

[13] H. C. van de Hulst, “Light Scattering by Small Particles,” Dover Publications Ed., ISBN 0-486-64228-3.

[14] Craig F. Bohren, Donald R. Huffman, “Absorption and Scattering of Light by Small Particles,” John Wiley & Sons, Inc. Ed., ISBN 0-471-05772-X.

[15] M. R. Luo, G. Cui, B. Rigg, “The Development of the CIE 2000 Colour-Difference Formula: CIEDE2000,” Color Res Appl. 26(5), 340-350 (2001).

[16] Gaurav Sharma, Wencheng Wu, Edul N. Dalal, “The CIEDE2000 Color-Difference Formula: Implementation Notes, Supplementary Test Data, and Mathematical Observations,” Color Res Appl. 30(1), 21-30 (2005).

[17] https://www.iso.org/standard/74166.html

[18] Aveek Bid, Achyut Bora, A. K. Raychaudhuri, “Temperature Dependence of the Resistance of Metallic Nanowires of Diameter $\geqslant$15 nm: Applicability of Bloch-Grüneisen Theorem,” Phys. Rev. B 74, 035426 (2006).

[19] Sarath Ramadurgam, Katherine Elizabeth Hansen, Tzu-ging Lin, Amartya Dutta, Sulaiman Abdul-Hadi, Chen Yang, “Optical Properties of Single Coaxial Nanowires,” https://nanohub.org/tools/nwabsorption, doi:10.4231/D3ZP3W30Z (2018).

Chapter 7

Conclusion

In this thesis, I have comprehensively explored anisotropy effects in AgNW networks. I used various optical measurement methods such as polarization spectroscopy, ellipsometry and polarimetry to characterize the relationship between structural, electrical and optical anisotropy. I also examined ways to reduce two practical problems encountered when using TCTFs for touch screen applications: LCD light leakage and electrode pattern visibility.

7.1 Summary of the thesis

In Chapter 3, I investigated structural anisotropy within AgNW networks and showed that the long axis of the AgNWs is preferentially oriented in the lengthwise direction of the TCTF. The resulting electrical and optical anisotropies are both correlated to the AgNW angular distribution. Their magnitudes are both smaller than that of structural anisotropy. The relationship between structural and optical anisotropy depends on the AgNW angular distribution and on the angular dependence of single-AgNW extinction. Furthermore, the direction-dependent equation linking sheet resistance and polarized transmittance is similar to the relationship between unpolarized transmittance and mean sheet resistance for isotropic AgNW networks. This allowed me to derive quantitative estimates of

structural and electrical anisotropy by optical analysis.

In Chapter 4, the orthogonal optical constants of the AgNW network were determined by Mueller matrix spectroscopic ellipsometry. These measurements showed the 3D morphology of the composite film, confirming that AgNWs are not only preferentially oriented in the lengthwise TCTF direction but also slightly tilted vertically. Furthermore, refractive index dispersion showed evidence of in-plane and out-of-plane retardation.

In Chapter 5, I explored the light leakage phenomenon. I showed that light leakage, retardation and depolarization are directly proportional to the AgNW loading and that depolarization decreases with decreasing AgNW diameter. I formulated two practical methods to reduce light leakage: minimizing retardation by aligning the TCTF's principal axis with the polarizer's transmission axis; using small-diameter AgNWs to reduce depolarization.

Chapter 6 was dedicated to the quantitative evaluation of pattern visibility. I analyzed diffuse reflection spectra of the TCTFs to derive the color space. Then, I calculated the color difference ΔE between regions with and without AgNWs. I showed that ΔE was smallest for TCTFs with the smallest AgNW diameter, thus that choosing small-diameter AgNWs directly leads to minimizing pattern visibility. Finally, among TCTFs with similar sheet resistance, those with smaller AgNW diameters showed stronger absorption in the near-UV region and less scattering at all wavelengths, despite large AgNW loading amounts.

7.2 Future work

In this study, I established an optical method to characterize the AgNW angular distribution. This will be useful for mass production of AgNW-based TCFs. I also devised a strategy to reduce light leakage and pattern visibility, both undesirable for device applications. However, some remaining issues must be addressed. For example, the reasons for the AgNW orientation should be determined. When this is done, isotropic TCFs with the same level of performance as ITO films can be obtained. The methodology that I devised represents a fundamental technological improvement for this purpose.

To generalize the use of AgNW-based TCFs in the next generation of flexible devices, solving the optical issues described in this study is not sufficient. Device configuration must also be optimized for flexibility and for chemical and electrical reliability. However, I believe that reducing light leakage and pattern visibility will significantly promote AgNW-based TCFs for device applications.

List of publications

A. Refereed Journal Articles

1. Takeo Tomiyama, Hiroshi Yamazaki, Optical Anisotropy Studies of Silver Nanowire/Polymer Composite Films with Mueller Matrix Ellipsometry, Appl. Surf. Sci., **421** (2017) 831-836

2. Takeo Tomiyama, Yasuhiro Seri, Hiroshi Yamazaki, Relationship between Wire Orientation and Optical and Electrical Anisotropy in Silver Nanowire/Polymer Composite Films, Appl. Surf. Sci., **469** (2019) 340-347

3. Takeo Tomiyama, Kensuke Yoshihara, Hiroshi Yamazaki, Polarization Properties of Silver Nanowire/Polymer Composite Films: Diattenuation, Retardance and Depolarization, Opt. Mater. Express, **9**(6) (2019) 2582-2594

4. Takeo Tomiyama, Ikuo Mukai, Hiroshi Yamazaki, Yoshihiko Takeda, Optical Properties of Silver Nanowire/Polymer Composite Films: Absorption, Scattering and Color Difference, Opt. Mater. Express, **10**(12) (2020) 3202-3214

B. Presentations at International Conferences

1. 7th International Conference on Spectroscopic Ellipsometry (2016, Berlin)

2. 6th International Conference and Exhibition on Materials Science and Chemistry (2018, Rome)

Appendix 1

Orientation of AgNWs in the composite films

The validity of the OrientationJ calculations for AgNW angular distribution was verified as follows: in a first step (Figure A1 − 1), I hypothesized that the AgNW angular distribution is best described by a von Mises PDF, as explained in Chapter 3. Next, random images of nanowire networks with known angular distribution were generated with the Mathematica software using von Mises PDFs (Figure A1−2). The effective angular distribution was then measured with OrientationJ on a sample of 100 images (Figure A1−3). Finally, the averaged angular distribution was fitted with a von Mises PDF and the fitting parameters were determined (Figure A1−4). I was able to confirm that the fitted value of the concentration coefficient κ was close to the initial value used to generate the images, thereby verifying the initial assumption.

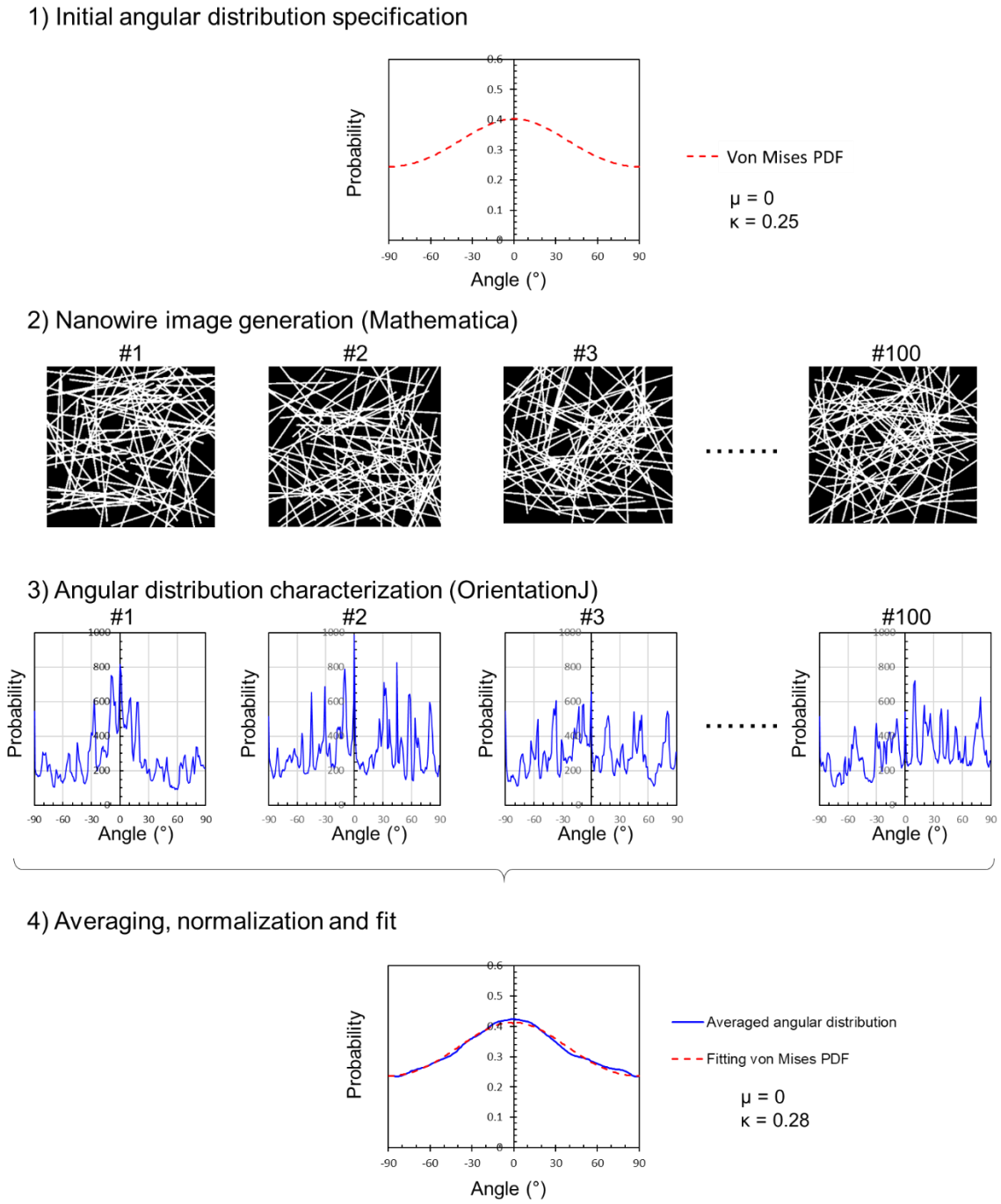

Figure A1. Methodology used to determine the AgNW angular distribution in the TCTFs.

Appendix 2

CIEDE2000 color difference formula

The equations defining the CIELAB color indices and used to derive the CIEDE2000 color difference (detailed below) are defined in:

Gaurav Sharma, Wencheng Wu, Edul N. Dalal, "The CIEDE2000 Color-Difference Formula: Implementation Notes, Supplementary Test Data, and Mathematical Observations," Color Res Appl. 30(1), 21-30 (2005).

1. Calculate the CIELAB L*, a*, b*:

$$L^* = 116 \cdot f(Y/Yn) - 16$$
$$a^* = 500 \cdot [f(X/Xn) - f(Y/Yn)]$$
$$b^* = 200 \cdot [f(Y/Yn) - f(Z/Zn)]$$

where X, Y, Z describe the color stimulus considered, X_n, Y_n, Z_n describe a specified white achromatic reference illuminant, and f is defined as

$$f(I) = \begin{cases} I^{1/3} & \text{for } I > 0.008856 \\ f(I) = 7.7871 + 16/116 & \text{otherwise} \end{cases}$$

2. Infer C_i', h_i':

$$C_{i,ab}^* = \sqrt{(a_i^*)^2 + (b_i^*)^2} \qquad i = 1, 2$$

$$\bar{C}_{ab}^* = \frac{C_{1,ab}^* + C_{2,ab}^*}{2}$$

$$G = 0.5 \cdot \left(1 - \sqrt{\frac{\bar{C}_{ab}^{*\,7}}{\bar{C}_{ab}^{*\,7} + 25^7}}\right)$$

$$a_i' = (1 + G) \cdot a_i^* \qquad i = 1, 2$$
$$C_i' = \sqrt{(a_i')^2 + (b_i^*)^2} \qquad i = 1, 2$$

$$h'_i = \begin{cases} 0 & b^*_i = a'_i = 0 \quad i = 1,2 \\ \tan^{-1}(b^*_i / a'_i) & \text{otherwise} \quad i = 1,2 \end{cases}$$

3. Calculate $\Delta L'$, $\Delta C'$, $\Delta H'$:

$$\Delta L' = L^*_2 - L^*_1$$
$$\Delta C' = C'_2 - C'_1$$

$$\Delta h' = \begin{cases} 0 & C'_1 C'_2 = 0 \\ h'_2 - h'_1 & C'_1 C'_2 \neq 0; |h'_2 - h'_1| \leq 180° \\ (h'_2 - h'_1) - 360° & C'_1 C'_2 \neq 0; (h'_2 - h'_1) > 180° \\ (h'_2 - h'_1) + 360° & C'_1 C'_2 \neq 0; (h'_2 - h'_1) < -180° \end{cases}$$

$$\Delta H' = 2 \cdot \sqrt{C'_1 C'_2} \cdot \sin\left(\frac{\Delta h'}{2}\right)$$

4. Calculate CIEDE2000 Color-Difference ΔE_{00}:

$$\bar{L}' = (L^*_1 + L^*_2)/2$$
$$\bar{C}' = (C'_1 + C'_2)/2$$

$$\bar{h}' = \begin{cases} \frac{h'_1 + h'_2}{2} & |h'_1 - h'_2| \leq 180°;\ C'_1 C'_2 \neq 0 \\ \frac{h'_1 + h'_2 + 360°}{2} & |h'_1 - h'_2| > 180°;\ (h'_1 + h'_2) < 360°;\ C'_1 C'_2 \neq 0 \\ \frac{h'_1 + h'_2 - 360°}{2} & |h'_1 - h'_2| > 180°;\ (h'_1 + h'_2) \geq 360°;\ C'_1 C'_2 \neq 0 \\ (h'_1 + h'_2) & C'_1 C'_2 = 0 \end{cases}$$

$$T = 1 - 0.17 \cdot \cos(\bar{h}' - 30°) + 0.24 \cdot \cos(2\bar{h}') + 0.32 \cdot \cos(3\bar{h}' + 6°) - 0.20 \cdot \cos(4\bar{h}' - 63°)$$

$$\Delta\theta = 30 \cdot \exp\left\{-\left[\frac{\bar{h}' - 275°}{25}\right]^2\right\}$$

$$R_c = 2 \cdot \sqrt{\frac{\bar{C}'^7}{\bar{C}'^7 + 25^7}}$$

$$S_L = 1 + \frac{0.015 \cdot (\bar{L}' - 50)^2}{\sqrt{20 + (\bar{L}' - 50)^2}}$$

$$S_C = 1 + 0.045 \cdot \bar{C}'$$

$$S_H = 1 + 0.015 \cdot \bar{C}' \cdot T$$

$$R_T = -\sin(2\Delta\theta) \cdot R_C$$

$$\Delta E_{00} = \sqrt{\left(\frac{\Delta L'}{S_L}\right)^2 + \left(\frac{\Delta C'}{S_C}\right)^2 + \left(\frac{\Delta H'}{S_H}\right)^2 + R_T \left(\frac{\Delta C'}{S_C}\right)\left(\frac{\Delta H'}{S_H}\right)}$$

Acknowledgements

First of all, I would like to express my deep gratitude to my supervisor, Prof. Yoshihiko Takeda, Tsukuba University, for his guidance, excellent advice, and support throughout my Ph.D. study. I also would like to thank Prof. Jie Tang, Prof. Naoki Fukata, Prof. Satoshi Ishii, and Prof. Muneaki Hase for reviewing my thesis.

The contents of the present work were performed at Showa Denko Materials Co. Ltd. (formerly Hitachi Chemical Co. Ltd.) and National Institute for Materials Science (joint graduate school program of Tsukuba University). I would like to express my grateful thanks to my colleagues (R&D member of TCTF), especially Mr. Hiroshi Yamazaki, Mr. Ikuo Mukai, Mr. Seri Yasuhiro, and Kensuke Yoshihara. Furthermore, I would like to thank all the people working in the same lab for sharing their support, especially Mr. Junichi Imaizumi, Mr. Yasuhiko Awano, Mr. Tadashi Okuda, Mr. Goki Toshima, Ms. Mariko Konishi, and Mr. Tomoki Takayama.

I would like to thank to Yasuharu Oba and Takanobu Sato (J. A. Woollam Japan) for their insightful suggestions in ellipsometry analysis.

Special thanks go to my friends Dr. Eric Dupuy and Mr. Jotham Sadan to carefully proofread and improve my manuscript.

Finally, I thank my wife, Miwa, for her continuous support and patience.

This thesis would not have been completed without the cooperation and support of everyone involved.

February 28, 2021

Takeo Tomiyama